12-2008

Nano-Raman Spectroscopy and Surface Nanostructuring Using Near-Field Optics

Kaijun Yi
University of Nebraska - Lincoln, kjyi1@bigred.unl.edu

NANO-RAMAN SPECTROSCOPY AND SURFACE NANOSTRUCTURING USING NEAR-FIELD OPTICS

by

Kaijun Yi

A Dissertation

Presented to the Faculty of

The Graduate College At the University of Nebraska

In Partial Fulfillment of Requirements

For the Degree of Doctor of Philosophy

Major: Engineering

Under the Supervision of Professor Yongfeng Lu

Lincoln, Nebraska

December, 2008

NANO-RAMAN SPECTROSCOPY AND SURFACE NANOSTRUCTURING USING NEAR-FIELD OPTICS

Kaijun Yi, Ph. D.
University of Nebraska, 2008

Adviser: Yongfeng Lu

To satisfy the development of nanoscience and nanotechnology, techniques to characterize and fabricate nanostructures and nanodevices are in great demand. Laser, as a unique monochromatic and coherent light source, meets the needs because it exhibits the potential to reveal some vital information of the materials. However, the applications of laser technology to nanoscience and nanotechnology are facing a severe challenge: the spatial resolution cannot be further enhanced to achieve nanometer scales due to the optical diffraction limit associated with conventional optics. In response to this challenge, near-field optics has been emerging as a new scientific area to deal with optical phenomena at that scales. The objective of this dissertation is to explore the possibility and extend the capability of laser technology into the fabrication and characterization of nanostructures and nanodevices using near-field optics. With the aim of establishing a frame to this objective, our goals of this study are to develop novel optical characterization techniques and platforms with nanoscale resolutions, and to fabricate nanostructures using laser technology.

First, theoretical studies on the optical near fields induced by microparticles, metallic tips and metallic nanostructures were accomplished by using the Finite-Difference-Time-Domain method. Secondly, based on a micro-Raman spectrometer, a nano-Raman spectrometer was developed by using a scanning tunneling microscope in

combination with side-illumination optics. The spatial resolution of 20 nm of this instrument was demonstrated by mapping single-walled carbon nanotubes. Thirdly, assisted by using metallic nanostructures, the Raman enhancement was further improved by one order. Fourthly, using self-assembled silica microparticles, the Raman enhancement was observed. This technique has a spatial resolution of 100 nm. Fifthly, using the developed techniques, the properties of the single-walled carbon nanotubes were systematically studied through spectral characterization and Raman imaging. Finally, highly conductive Si nanostructures with a feature size of 30 nm were fabricated using a laser-assisted scanning tunneling microscope. The developed techniques have the capabilities of fabricating nanostructures and characterizing their topographic, electronic, mechanic, thermal and optical properties systematically.

ACKNOWLEDGEMENT

During the past three and a half years in Lincoln, NE, I have gained a lot through the academic studies and the research projects, and have been living a fulfilled and colorful life at the Department of Electrical Engineering at the University of Nebraska-Lincoln (UNL). I have never thought that pursuing Ph. D. degree is such a big challenge. I have never expected to experience so many negative feelings, such as sorrow, disappointment, self-doubtfulness, anxiety, depression, and exhaustion, during the period. Thanks to those people who have provided me help and always stood on my side when I was in trouble, I have successfully gone through those difficulties, and finally have been rewarded happiness and confidence. Upon the completion of my dissertation, I would like to take this opportunity to deliver my overwhelming thanks to them.

First of all, undoubtedly, I would like to greatly appreciate my supervisor, Prof. Yongfeng Lu, who has provided me this opportunity allowing me to join this dynamic group and be able to continue my dream of self surpassing. His profound knowledge, keen vision, rigorous attitude towards science, touch-on-ground style, forgiveness, and especially hardworking have impressed me a lot, and will significantly impact my future career path. Thanks to his supervision and financial support, I can complete my degree smoothly without extra worries. During the years of his supervision, I have learned not only how to do research, solve the problems encountered in doing experiments, write papers, make presentations, but also how to deal with difficulties ahead of me and think as an individual. In addition, I have learned how to be a responsible person, how to balance work and personnel life, and how important for us to contribute to the society.

His courage, wisdom and determination will encourage me to circumvent all the challenges I might face ahead of me.

Secondly, my special thanks go to my degree committee members, Profs. Dennis R. Alexander, Natale J. Ianno, and Paul G. Snyder from the Department of Electrical Engineering at UNL, and Prof. Xinwei Wang from the Department of Mechanical Engineering at UNL, for their time and efforts on instructing me to complete the degree.

Thirdly, I would like to thank my colleagues in the group of Laser Assisted Nano Engineering (LANE) lab. Without them, I can not image how miserable my life would be during these years. Specifically, I appreciate Dr. Jing Shi with whom I had a great time on the nanotube project, Dr Hao Ling who helped me to prepare samples and who I shared a lot with about research and personnel life, Ms. Hao Wang who helped me to prepare samples and gave me a lot of valuable advices when asked, Mr. Xiaokang Shen who was my partner when exercising at the recreation center, and Mr. Xiangnan He who was my lab partner helping me to perform experiments. I would also thank other members, including current members: Dr. Yunshen Zhou, Dr. Jian Sun, Dr. Changbao Ma, Mr. Weiqing Yang, Mr. Wei Xiong, Mr. Zhiqiang Xie, Mr. Tadiyos T. Gebre, Mr. Masoud M. Samanii and Mr. Yang Gao and previous members: Dr. Yaoxuan Han, Dr. Zhenyu Yang, Dr. Ming Zhao, Mr. Kiran Mendu and Mr. Nagaraj Batta, for their help.

I had a happy leisure time and received a lot of encouragement from my friends, Dr. Haifeng Zhang, Dr. Jingxi Song, Mr. Qin Chen, Mr. Jiaqi Guo, Mr. Jingbo Hou, Mr. Longzhang Tian, Mr. Amere, Ms. Lijun Zhan and Ms. Tian Tian. It is a great honor to have being with them during the past years.

Fourthly, this dissertation is dedicated to my father who always believed that I can make a difference. The characteristics inherited from him have greatly influenced me by equipping me with necessary figure of merits. I want to show my great respect and thanks to my mother who had brought up me in that extremely difficult period. Her love, kindness, politeness and optimism have taught me how to be an honest man. This dissertation is also devoted to my grandpa with whom I have had a great childhood.

Finally, I would like to covey my great appreciation to my family members. My wife, Dr. Zhiqun Tang who lately graduated from the National University of Singapore, is a once-in-a-lifetime partner who had given me so much love and tremendous help, and sacrificed a lot to the family in taking care of me and nurturing my kids during the past 10 years. Without her, I would have never hoped to accomplish so much. My daughter, Sijun Yi who was born in Singapore in 2001, and my son, Chuanglong Yi who was born in Lincoln this May, have given me a lot of joy and helped me out of pressure and exhaustion. They have been giving me incomparable happiness.

I am crystal clear that the road ahead will never be straightforward, but with the knowledge I gained, the skills I mastered, the wisdom I learned, the relationships I made, the habit I formed, the accomplishment I achieved, the courage I had, and the events I experienced, I am more confident than ever to start a new chapter of my life firmly and bravely.

TABLE OF CONTENTS

LIST OF FIGURES

CHAPTER 1 INTRODUCTION

1.1 Background and motivation

1.2 Dissertation outline

1.1 Background and motivation

Laser, as a monochromatic and coherent light source, has been widely used in various areas such as engineering, chemistry, physics, biology, and biomedical for broad applications. Examples of those applications include material processing [1], communication [2], data storage [3], disease diagnosis and treatment [4], semiconductor lithography [5], fabrication [6] and spectroscopy [7]. Most of the applications, however, are limited to microscales, which results from the optical diffraction limit associated with conventional optics [8]. Therefore, without fundamental scientific breakthrough it would not be realistic applying these techniques to nanoscience and nanotechnology which deal with structures with features less than 100 nm [9]. The main objective of this dissertation is to explore the possibility and extend the capability of laser technology into this rapid developing field. Near-field optics is one of the most promising techniques to circumvent the optical diffraction limit [10-12]. Topics of nanoscale characterization and fabrication using lasers based on near-field optics are included in this dissertation.

While Scanning Probe Microscopy (SPM) has become a mature tool to measure topologic, mechanical, electronic, magnetic and thermal properties of materials at nanoscales [13], tools capable of characterizing chemical structures at nanoscales are necessary but rarely available. Raman spectroscopy (RS) in combination with near-field optics can address this issue by identifying chemical structures through Raman spectra which are associated with molecular vibration status [11]. On the other hand, while current efforts for nanoscale fabrication are being taken to reduce the optical wavelength or increase the Numerical Aperture (NA) of the objective or both, which renders high

cost and complicated design, fabrication using near-field optics offers cheap, fast, simple and reliable advantages over these solutions.

Near-field optics can be achieved from an aperture or an apertureless metallic tip by creating a localized optical field in nanoscale at the tip apex [15, 16]. The apertureless metallic tips made of silver (Ag), Ag-coated W (W) or gold (Au) are widely used because of several advantages: 1) they can generate a highly localized and significantly enhanced optical field, similar as in the Surface-Enhanced Raman Spectroscopy (SERS), which is the fundamental to achieve nanoscale resolutions; 2) their fabrication is straightforward and cost-effective; 3) the tip accommodates both the SPM and the RS, allowing the correlated studies of topologic, electronic, mechanical, electronic, magnetic, thermal and chemical properties of individual nanostructures.

Besides metallic tips, dielectric microparticles can also be used to produce optical near fields, which is also explored in this project. In particular, our focuses of this study are: 1) the theoretical study on the optical near fields induced by laser-tip and laser-microparticles interactions, 2) the development of a Tip-Enhanced Raman Spectrometer (TERS) and imaging system with nanoscale resolutions, 3) the systematical investigation of the impact of the nanojets generated by self-assembled silica microparticles on Raman enhancement, 4) the improvement of the detection sensitivity of the tip-enhanced Raman spectroscopy by using metallic nanostructures, 5) the examination of Single-Walled Carbon Nanotubes (SWCNTs) using the developed techniques and platforms, and (6) the surface nanostructuring on silicon (Si) substrates using a Laser-Assisted Scanning Tunneling Microscope (LASTM).

This study has both scientific and engineering significance. From perspectives of science, TERS can be used to characterize materials and devices at nanoscales, allowing us to investigate different properties of nanostructures in a correlated manner and completely understand mutual relationship. From perspectives on engineering, the understanding of different properties of the nanostructures will pave the way to design more powerful materials or devices which will be ultimately served in various areas. Meanwhile, LASTM allows us to gain systematic knowledge about formation mechanisms of nanostructures which will lead us to successfully develop desired nanostructures on which next generation devices will be based.

1.2 Dissertation outline

The most significant contributions of this dissertation are: 1) developed a TERS system which has a spatial resolution of 30 nm, and 2) fabricated highly conductive nanostructures with features of 30 nm on hydrogen-passivated Si surfaces using a LASTM. This dissertation includes nine chapters. In chapter 1, the motivation and background of this study is explained, and the dissertation outline is given. In chapter 2, the fundamentals and recent development relevant to this study are reviewed. In chapter 3, the theoretical study of optical near fields induced by microparticles, metallic tips and nanostructures is presented. In chapter 4, the details of designing the normal and tip-enhanced Raman spectrometer are discussed. In chapter 5, a technique to achieve RS at nanoscales using self-assembled silica microparticles is described. In chapter 6, a scheme to further improve the detection sensitivity of TERS using TERS assisted by metallic nanostructures is introduced. In chapter 7, an example of using the developed techniques

by characterizing SWCNTs is provided. In chapter 8, the fabrication of high-conductivity nanostructures on Si surfaces using a LASTM is presented. In chapter 9, the summary is given and some tasks beyond this study are discussed.

CHAPTER 2 BACKGROUND AND REVIEWS

2.1 Near-field optics: the path to nanometer optical resolution

2.2 Raman spectroscopy: the unique tool for chemical identification

2.3 Nanostructuring on semiconductor surfaces using a laser-assisted scanning tunneling microscope

2.1 Near-field optics: the path to nanometer optical resolution

2.1.1 The needs of nanoscience and nanotechnology

Nanoscience and nanotechnology, dealing with nanoscale structures less than 100 nm, have attracted much attention in the past decades due to their potentiality and applications in information processing, communications, biomedicine, chemistry, environmental science, tissue engineering, defense, and space exploration [1]. Nanotechnology was foresighted by Dr. Richard P. Feynman in the talk, "There is Plenty of Room at the Bottom" in 1959, for which he was inaugurated Nobel Prize in 1998.

As highly multidisciplinary subjects, nanoscience and nanotechnology has a significant impact on other fields such as applied physics, materials science, colloidal science, device physics, supramolecular chemistry, biology, medicine, and mechanical and electrical engineering. For example, the 45-nm Complementary Metal Oxide Semiconductor (CMOS) technology has given rise to the emerging of small, light, long-lasting, and multifunctional smart Personal Digital Assistant (PDA) and cell phone [2, 3]. The discovery of Giant Magnetoresistance (GMR) and Tunnel Magnetoresistance (TMR), which use two ferromagnetic layers separated by a nonmagnetic layer with a thickness of several nanometers, has led to the invention of hard disk drives with high capacity and rapid access time [4, 5]. The application of nanomaterials, e.g., Au nanoparticles, to biomedicine has enabled the inventions of diagnostic devices, contrast agents, analytical tools and drug-delivery vehicles for disease diagnosis and treatment [6, 7]. As oil is depletable, nanotechnology is becoming more and more important to deal with the energy issue by reducing power consumption, increasing the efficiency of energy production and building more environment friendly energy systems [8]. However, nanotechnology, is far

from maturity, and there is still a lot of areas to explore. For example, the need of further miniaturization of high performance and high density devices is compelling us to develop quantum devices based on moletronics using molecules or nanoelectronics using SWCNTs rather than microelectronics using Si technology because Si-based microelectronics is severely constrained by the inherent tunneling effect when the device features are comparable to or less than the electron de Broglie wavelength, i.e., 100 nm [9-12].

In nanoscience and nanotechnology, both the fabrication and characterization techniques of nanostructures need to be significantly improved. The fabrication methods can be categorized into two general types: “top-down” and “bottom-up” approach. In the "top-down" approach, nanostructures are constructed from larger entities without atomic-level control. In the "bottom-up" approach, materials and devices are built from molecular components which assemble themselves chemically by principles of molecular recognition. In both approaches, however, without precise characterization of the structures in atomic or molecule level, the controllable fabrication of such structures is nearly impossible. The impetus for nanotechnology comes from the invention of a new generation of analytical tools such as Scanning Probe Microscope (SPM) [13]. When coupled with refined processes such as Electron Beam Lithography (EBL) and Molecular Beam Epitaxy (MBE), these tools allow the deliberate manipulation of nanostructures, and lead to the observation of novel phenomena [14]. Scanning Electron Microscope (SEM) is another analytical tool that images the sample surface by scanning it with a high-energy beam of electrons in a raster scan pattern. The electrons interact with the

atoms of the sample and produce signals that contain information about the surface topography, composition and other properties such as electrical conductivity.

However, both SPM and SEM are not able to identify chemicals, which provide critical information of the nanostructures. For a cutting edge characterization tool, other than capability of chemical identification, some other requirements include: 1) it should be able to operate in a versatile environment; 2) it should be fast enough to allow for dynamic observation on a fast time-scale. Optical spectroscopic tools, e.g. RS, can fulfill those needs [15]. RS, by identifying chemical structures based on light-matter interactions, offers many unique advantages over its counterparts. For example, it is non-destructive and relatively inexpensive. In addition, it provides access to unique information under a wide range of operation conditions. Another appealing feature of this technique is that by coupling light with certain substances, surface nanostructuring, which is the basis of modern lithography, can be performed [16]. It is obvious that a versatile and multifunctional system for nanostructures fabrication and characterization using the optical technique should and would be developed.

2.1.2 Far-field optics: dilemma of the optical diffraction limit

A wealth of light-matter interactions allows for a variety of highly selective spectroscopic techniques, providing information not only on the elemental composition of a sample but also on its chemical organization and structure. The classic optics, however, has the difficulty in confining optical fields to volumes sufficiently small for the purposes of characterization and modification in nanoscales. The smallest volume of a light spot generated by conventional optics is governed by the optical diffraction limit [see Fig. 2.1(a, d)].

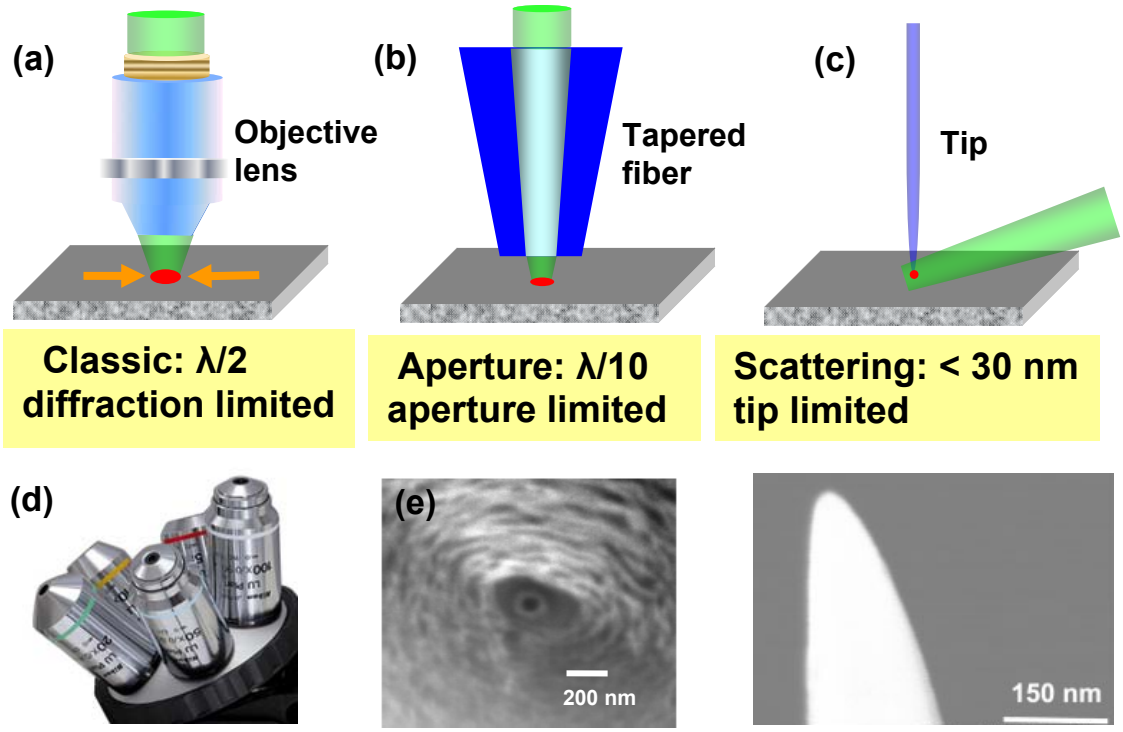

FIGURE 2.1 Comparison of approaches for (a) far-field optics using an objective lens, (b) near-field optics using a tapered fiber and (c) near-field optics using a metal tip. (d) practical objective lenses; (e) an aluminum (Al)-coated aperture probe prepared by pulling method [18]; (f) a Au tip produced by AC-wet etching method [19].

The optical diffraction limit, D, is defined as [17].

$$D = k\frac{\lambda}{NA} \quad . \tag{2.1}$$

Here, λ and NA refer to the optical wavelength and the numerical aperture of the lens, respectively. k is the factor which depends on the incident beam profile onto the lens. For uniform illumination, k = 0.61 (Rayleigh criterion); for an optimized ring shape illumination, k can be smaller, e.g., 0.36. With k = 0.36 and NA = 0.9, near-ultraviolet (UV) light (λ = 400 nm) can be focused down to $D \approx$ 140 nm, a capability that is exploited in modern photolithography. With the same illumination, D = 100 nm can be achieved with the best commercially available solid-immersion objective (NA = 1.4).

Clearly, classical optics ends with respect to resolution right at the borderline of nanometer-sized dimensions.

2.1.3 Near-field optics: overcoming the optical diffraction limit

The optical diffraction limit of the classical optics can be circumvented by near-field optics. Near-field optics is that branch of optics that considers configurations that depend on the passage of light to, from, through, or near an element with subwavelength features and the coupling of that light to a second element located a subwavelength distance from the first. This concept was first proposed by E. H. Synge in 1928, but was not realized experimentally until the 1950s when several researchers demonstrated the feasibility of sub-wavelength resolution [20]. In 1984, D. Pohl at IBM in Zurich, Switzerland, obtained for the first time a near-field optical scan traces recorded with an aperture-type probe at visible wavelengths [21].

As an evanescent wave, the optical field from near-field optics exhibits exponential decay with distance along the optical propagation direction. Due to their rapid decay, they are of importance only close to the interface. Using near-field optics, the attainable resolution is now determined by the size of the element used to confine the light but not by the wavelength of the light [22].

2.1.4 Approaches to achieving near-field optics

Tips with sharp apexes can be used to create optical near fields. Two kinds of tips exist: 1) a tip with an aperture of nanoscale diameter at the terminal such as the tip made of optical fibers [see Fig. 2.1(b, e)], and 2) an apertureless tip such as a Au or Ag tip [see Fig. 2.1(c, f)]. An aperture tip can be used to illuminate the sample through its aperture placed in

close proximity to the sample surface [18], and the light can be collected by the same aperture. The most frequently used aperture tip consists of a tip made from a transparent material, e.g., glass or quartz, coated with an opaque metal film so that a small opening is created at the apex of the tip. With this type of tip, D. Pohl *et al.* developed the first Near-field Scanning Optical Microscopy (NSOM) in 1984 when STM was invented and could provide the technology to position a tip to a sample surface within a few nanometres and scan the surface with a subnanometer resolution [21]. Another aperture tip is a micropipette with metal-coated end-face [23]. The most common design uses an optical fiber shaped at one end into a pointed, metal-coated tip with an aperture at its apex, while illuminated by a focused laser beam at the other end [24]. There are two main drawbacks associated with the aperture tip: the minimum spot size is limited by the skin depth; the tip transmits very little light through the aperture, i.e., the optical throughput is extremely low. This low throughput severely degrades the detection sensitivity. Plastic deformation [25], shadow evaporation [24] and Focused Ion Beam (FIB) [26] are usually used to fabricate aperture tips.

An apertureless tip achieves nanoscale resolution based on light scattering rather than light emission. The tip, either metallic or dielectric, can generate near fields at the proximity of the tip apex when it is placed very close, e.g., 1 nm, to the surface of a sample [27-29]. The apertureless tip has some advantages over the aperture tip: a higher near-field excitation and a higher spatial resolution. Its disadvantage is that the presence of the background signals may mask the near-field signals [30].

The mechanism behind the powerful capability of the apertureless tip is that a highly localized and significantly enhanced optical field can be generated in the

proximity of the tip apex induced by the Localized Surface Plasmons (LSPs) and by the "lightning rod" effect [19]. The light wavelength, the tip geometry and the substrate properties influence the localized optical field. By tuning those parameters to optimal conditions, the optical field might be enhanced more strongly. For example, much higher optical enhancement can be achieved through the resonant excitation when the tip resonates with the focused beam at a certain wavelength. The recent observation of such enhancement, by a Au tip, of fluorescence from a single fluorescent molecule paves the way for nanoscale fluorescence microscopy [31]. Second-harmonic generation may also be enhanced in the vicinity of a metal tip, providing a sensitive technique to investigate the field distribution over a surface [32]. The most important breakthrough of this approach, however, is that chemical specificity at nanoscales becomes reality when this approach is applied on RS [33-35].

2.1.5 Near-field scanning optical microscopy: observing at the subwavelength scale

An optical microscope with a scanning function in combination with near-field optics constitutes a Near-field Scanning Optical Microscope (NSOM). The first NSOM was developed in 1984 by Pohl *et al.* [21]. NSOM began to capture wider interest in the early 1990s. This field was stimulated in particular by a series of exploratory NSOM studies by E. Betzig *et al.* at Bell Laboratories [37-40]. Meanwhile, other forms of NSOM began to raise increasing interests, in the interaction of light with single molecules, such as resonant energy transfer [41], Raman microscopy [42], trapping of particles by optical forces [43], localization and waveguiding in so called photonic crystals [44], plasmon excitation at nanometre-sized individual and coupled particles [45] and optical antennas [46].

Besides NSOM, near-field optics has a variety of other applications, such as single-molecule microscopy and spectroscopy, plasmons properties of metallic nanostructures, optical nanolithography, optical manipulation, photonic crystals and bandgap structures, and optical antennas [17].

2.2 Raman spectroscopy: the unique tool for chemical identification

2.2.1 Theory of Raman spectroscopy

Different types of radiation occur when light interacts with matter, including diffraction, scattering, photoluminescence and fluorescence, based on which different techniques and instruments have been developed and used to analyze compositions, chemical structures and bandgaps of samples. There are two different type of radiation, i.e., Rayleigh scattering and Raman scattering. Rayleigh scattering is a two-photon process having a net effect of changing the direction of light, while keeping its frequency constant, during which there is no exchange of energy. Therefore, Rayleigh scattering is elastic. Raman scattering, on the other side, is a two-photon process having net effects of scattering photons but changing their frequency. This changing in frequency, which is characteristic of inelastic scattering, provides a basis for Raman spectroscopy [47]. Mathematical analysis is used to understand the scattering processes.

The polarizability of molecules α, which is the key factor for Raman scattering, represents the ability of an applied electric field E to induce a dipole moment μ_{in} in an atom or molecule. μ_{in} can be expressed as [48]

$$\mu_{in} = \alpha E \,. \tag{2.2}$$

Suppose the polarizability is α_0 at a molecule's equilibrium nuclear geometry. At some distance, Δr, away from this equilibrium nuclear geometry, the instantaneous polarizability α is given by

$$\alpha = \alpha_0 + \left(\frac{\partial \beta}{\partial r}\right)\Delta r . \tag{2.3}$$

Here, the derivative,

$$\left(\frac{\partial \alpha}{\partial r}\right), \tag{2.4}$$

represents the change in polarizability with change in position. If the molecule is vibrating or rotating in some sinusoidal fashion, Δr can be expressed as some sinusoidal function in terms of the vibration frequency v and the time t:

$$\Delta r = r_{\max}\cos(2\pi v t). \tag{2.5}$$

Here, r_{max} is the maximum vibrational amplitude. Likewise, the induced electric field E by the light with a particular frequency v_{in} also has sinusoidal behavior:

$$E = E_{\max}\cos(2\pi v_{in} t) \tag{2.6}$$

Here, E_{max} is the maximum amplitude of electric field. Substituting E, α, and Δr into equation (2) yields:

$$\mu_{in} = \alpha_0 E_{\max}\cos(2\pi v_{in} t) + E_{\max} r_{\max}\left(\frac{\partial \alpha}{\partial r}\right)\cos(2\pi v t)\cos(\pi v_{in} t). \tag{2.7}$$

Eq. (2.7) can be rewritten as

$$\mu_{in} = \alpha_0 E_{\max}\cos(2\pi v_{in} t) + \frac{E_{\max} r_{\max}}{2}\left(\frac{\partial \alpha}{\partial r}\right)\left(\cos(2\pi t(v_{in} + v)) + \cos(2\pi t(v_{in} - v))\right). \tag{2.8}$$

Three terms from the formula indicate three different types of radiation: Rayleigh scattering (first term, unchanged energy), Anti-Stokes Raman light (second term, higher energy) and Stokes Raman light (third term, lower energy). The last two terms show that incoming photons will shift their frequencies, up and down by amounts equal to certain motions of molecules, which ultimately explain Raman scattering and are the basis of Raman spectroscopy. If $\left(\frac{\partial \alpha}{\partial r}\right) = 0$, no Raman scattering will occur, yielding the selection rule: A molecular motion will be Raman-active only if the motion occurs with a changing polarizability.

2.2.2 Factors to determine Raman signal intensity

The Raman scattering intensity for a given wavelength and observation angle is dependent on the incident power, the scattering volume and the Raman cross section of the molecule. Specific intensity, L, defined as the number of Raman photons scattered from 1 cm^2 of the sample into one steradian of solid angle in 1 sec, can be described by [47]

$$L = P_D \beta D_s K \quad . \tag{2.9}$$

Here, β is the Raman cross section, D_s is the number density of scatterers (molecules/cm^3), P_D is the power density (photons/cm^2 second), and K is either the thickness of the sample or the penetration depth of the laser beam in the sample, whichever is less.

2.2.3 Surface-enhanced Raman spectroscopy

Surface Enhanced Raman Spectroscopy (SERS) is a surface sensitive technique that results in the enhancement of Raman scattering by the molecules adsorbed on rough metal surfaces [15]. The enhancement factor can be as much as 10^{14}-10^{15}, so this technique is sensitive enough to detect single molecules [49]. The electromagnetic mechanism explains that the Localized Surface Plasmon Resonance (LSPR) due to the collective oscillation of the electron gas stimulated by the incident photons contributes to the enhancement. The generated plasmons increase both the incident electric field and the scattered Raman field, leading to the overall enhancement scaling roughly as E^4 (E is the incident electric field) [50]. Chemical mechanism explains that the enhancement derives from a resonance Raman enhancement process due to charge transfer excitation between analyte molecules and metal nanoparticles [51].

The selections of the substrate materials and the excitation wavelengths are critical to achieve high enhancement. Researchers have proposed different types of SERS-active substrates such as colloid Ag [52], Au particles [53], Ag electrodes [54], island films of Ag and Au [55], metal fractals [56], Rhodium multipods [57], and nanostructures [58, 59]. The substrates with metallic nanostructures have obvious advantages over other alternatives due to their tunable structural geometry, stable reproducibility, high sensitivity and controllable fabrication. The tunability of a nanostructure geometry helps to tailor the chemical and physical properties of analytes attached to the substrate surfaces. Near-field effects from nanostructures like bowties and sharp metal tips have been reported to be able to enhance the electric field, which provides another advantage to the fabrication of nanostructure-based substrates [60].

Simulations have illustrated that the electric field intensity coupled by two triangle-shaped Ag nanostructures separated by 2 nm distance can be enhanced as high as 10^5 [61].

Typical applications of SERS include chemical analysis [62], chemical warfare agents detection [63], single molecule detection [41], disease diagnosis and therapy control [64], industrial process monitoring [65] and residual stress detection [66]. However, SERS still suffers from a few but severe drawbacks: 1) only those metals (Ag, Au and Cu) which support an easy excitation of the LSP modes in the visible region can provide large enhancement for the Raman process; 2) the metal surfaces must be heavily roughened; 3) the position where SERS occurs, i.e., the so called "hot spot", can not be precisely controlled; 4) the spatial resolution is still defined by the optical diffraction limit. Most of the above difficulties can be circumvented by TERS.

2.2.4 Tip-enhanced Raman spectroscopy

Tip-enhanced Raman spectroscopy is a combination of Raman spectroscopy with a sharp metallic tip which can be controlled very close to the sample surfaces. Due to the highly localized and significantly enhanced optical field generated by the tip apex at the proximity of the tip, nanoscale spatial resolutions can be achieved [67-69]. A Raman spectroscopy with nanoscale resolutions is named as a nano-Raman Spectroscopy (n-RS).

In 1985, Wessel firstly proposed the idea to scan a sample surface with a Ag nanoparticle which was controlled by piezo crystals [70]. However, the control of the distance between the particle and the substrate was extremely difficult. Then he suggested that an STM might be used to control this distance and the scanning tip served as a light enhancer, which was validated later. The first TERS system was reported by Zenobi *et al.* who combined an AFM with a RS in 2000 [71]. The configuration that the

tip and the light were on the opposite sides of the sample, i.e., the bottom illumination optics, was used for this system. However, this configuration was only valid for transparent samples. To study opaque samples, Pettinger *et al.* developed a TERS system by employing an STM in combination with side illumination optics, in which the tip and the sample were on the same side of the sample [72,73].

The origin of the enhanced electromagnetic field is a combination of two distinct physical effects: the "lightning rod" effect, which is a result of the geometric singularity associated with sharply pointed metal structures, and the LSPs, which depend strongly on the excitation wavelength and are specific to the geometrical shape of a metal surface. The excitation laser light is focused onto the very end of the sharp metal tip which is kept in close distance to the surface. LSPs are excited at the tip apex or in the cavity between the tip and the sample, and only the molecules located right underneath the tip in the enhanced field give rise to intense Raman scattering. The tip serves as amplifying antenna for the incoming and outgoing electromagnetic waves, thus supporting extremely intense Raman scattering [19].

TERS has been used for different applications, such as material analysis, cell identification and device characterization. Using a Cr-coated quartz tip, Zhu *et al.* demonstrated that stressed Si lines with a width of 10 nm can be resolved by identifying a double band [74]. Hartschuh *et al.* obtained the Raman imaging of the individual SWCNT [75].

2.2.5 Raman instrumentation

Raman spectrometer is a practical apparatus used to measure frequency changes from the scattered light with respect to the incident light. It consists of three parts: a light

source (a laser), a delivery and collection optical path, and a detector. The light source provides the necessary light with a specific wavelength and power. The delivery and collection optical path is used to deliver the light to the sample and collect the scattered signals. The scattered signals are sensed by the detector [76]. Raman spectrometer can be categorized to two types based upon sensing methods: Fast Fourier Raman spectrometer (FT-Raman spectrometer) and UV/VIS/NIR Raman spectrometer. Raman signals are detected by an FT-Raman spectrometer through modulating the different frequencies (non-dispersive), while they are detected by a UV/VIS/NIR Raman spectrometer through a multichannel detector (dispersive). The advantages of an FT-Raman spectrometer include the reduction of fluorescence, the ease of operation, and the high spectral resolution, and its disadvantages include restricted wavelength response, low sensitivity, strong absorption, local heating and significant thermal background. The advantages of a UV/VIS/NIR Raman spectrometer include unlimited wavelength capability (200 - 1700 nm), easy coupling to fiber optics, the capability of integration with microscopes, two-dimensional (2D) imaging, extremely high sensitivity, high optical throughput and high quantum efficiency. The disadvantages of dispersive Raman encompass expensive light source, frequent spectral calibration and strong fluorescence.

Most of the current commercial Raman spectrometers are configured as dispersive type in combination with a microscope. The basic components of a singly-dispersive Raman spectrometer system are shown in Fig. 2.2 (a). Main system subcomponents are the laser light source, the microscope sample chamber and the spectrograph. Light in a narrow, collimated beam from the excitation laser unit passes a line filter to remove any unwanted laser lines and sidebands, before passing via beam splitter into the microscope.

Some instruments may have more than one laser and laser selection optics. The microscope can be regarded as a normal laboratory microscope, with a set of exchangeable objectives on a rotating turret. These lenses focus the laser light into a small, nearly diffraction-limited spot, typically less than 1 μm in diameter. The sample scatters this light, which is collected by the same objective and transmitted back to the detection unit. A Rayleigh rejection notch filter, which is a narrow rejection-band filter, is used to efficiently blocks light with the wavelengths near the laser line from reaching the spectrograph section. Figures 2.2 (b-d) shows a practical Raman spectrometer, a Raman spectrum and a Raman image of azobenzene polymer, respectively.

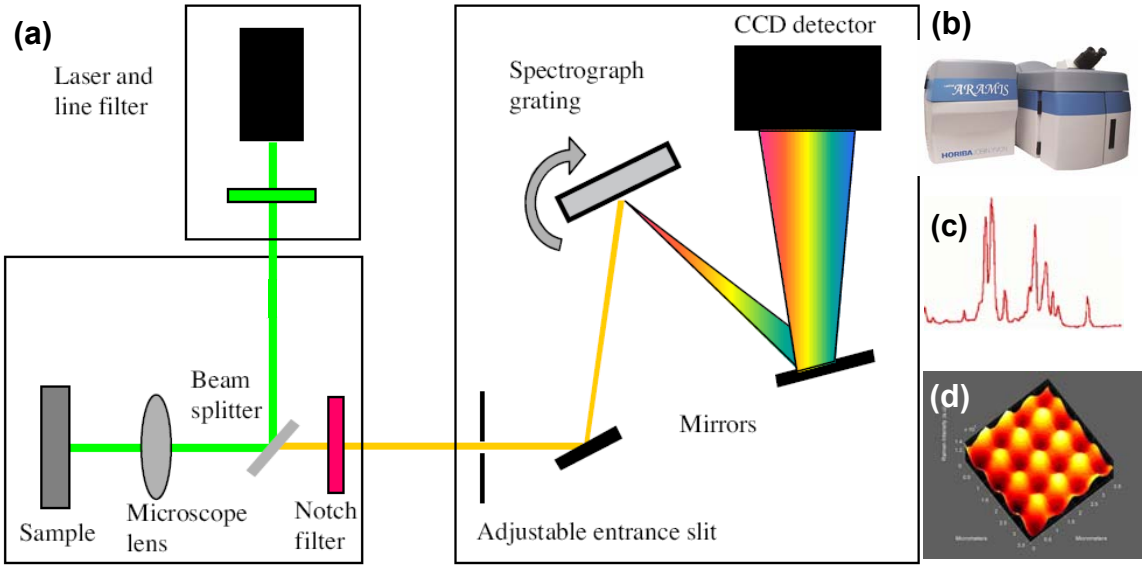

FIGURE 2.2 (a) Schematic diagram of a Raman spectrometer; (b) a practical Raman spectrometer from HORIBA Jobin Yvon; (c) Raman spectrum and (d) Raman imaging of azobenzene polymer. (b)-(d) are cited from http://www.jobinyvon.com.

2.3 Nanostructuring on semiconductor surfaces using a laser-assisted scanning tunneling microscope

2.3.1 Scanning tunneling microscope

A scanning tunneling microscope (STM) is an apparatus capable of obtaining surface images with atomic-scale resolutions, measuring tunneling spectroscopy that reveal a variety of surface electronic properties, and manipulating individual surface atoms and molecules with atomic-scale precisions. Illustrated in Fig. 2.3(a) is a schematic diagram of an STM. A sharp metal tip is brought so close to the surface of an electrically-conductive sample that the gap between the tip and the surface is less than 1 nm and a voltage of a few volts is applied between the tip-surface gap, enabling electrons to quantum-mechanically tunnel across the gap. The resulting tunnel current, typically on the order of 1 nA, depends exponentially on the gap. If the gap is regulated to keep the current constant while the tip is scanning laterally, adjacent profiles of the surface topography can be assembled into an image via a computer.

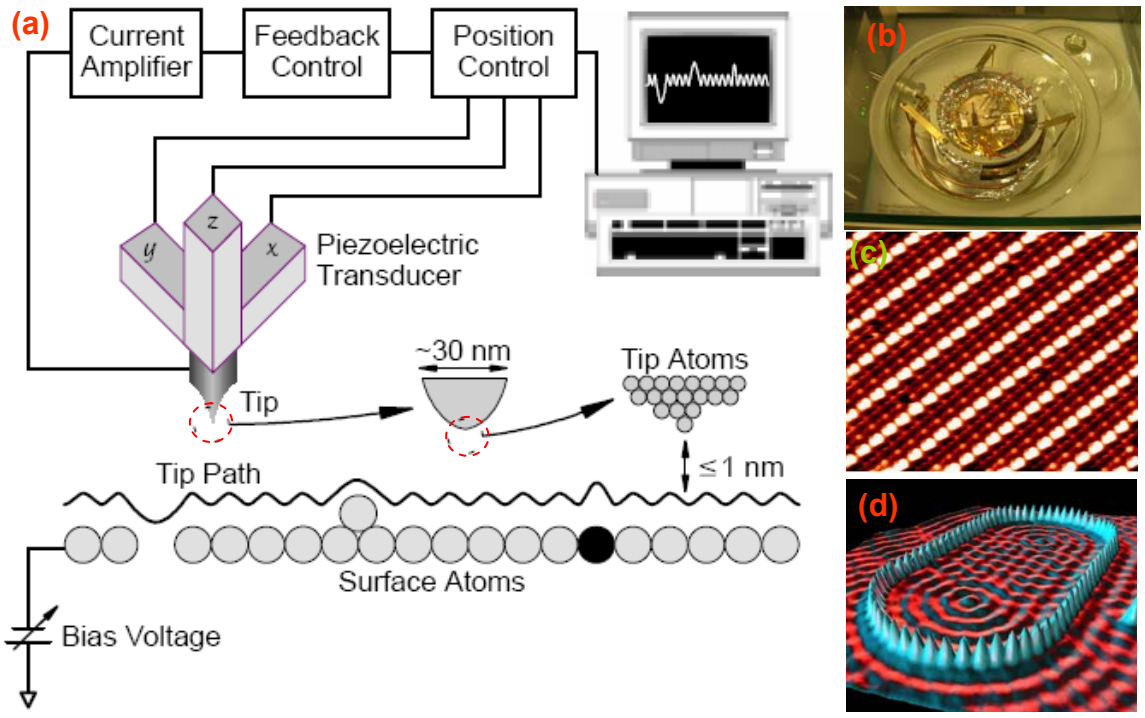

FIGURE 2.3 (a) Schematic diagram of a scanning tunneling microscope; (b) first scanning tunneling microscope in Deutsches museum (http://www.flickr.com); (c) Pt atoms adsorb

onto Ge (001) surface (www.omicron.de); (d) stadium corral by placing iron atoms on Cu (111) (http://www.almaden.ibm.com).

To achieve atomic-scale resolution, the mechanical and electrical components of the STM must enable the tip to be positioned approximately 1 nm above the surface. The tip is also required to be controlled both vertically and laterally with a precision less than 0.01 nm. Therefore, the STM must include a coarse approach mechanism capable of bringing the tip into tunneling range with the sample. Once in the tunneling range, a scanning transducer controls the vertical and lateral position of the tip over the sample. The sample and the scanner are mounted in a rigid framework to minimize the effect of mechanical resonances. A vibration isolation system, often based on a magnetically-damped spring suspension, is usually required to reduce transmission of external vibrations. The first STM developed by IBM Research Zurich in 1981 is shown in Fig. 2.3(b).

The inherent resolution of an STM is a direct consequence of the quantum mechanical tunneling between the tip and the surface. This current depends both on the width and height of the tunneling barrier, and on the electronic structure of the tip and the surface. By measuring the interdependence of the various tunneling parameters, e.g., the bias voltage, the tunneling current and the tunneling gap, the images and spectra of a variety of surface electronic properties can be recorded in addition to the topography of the surface.

The STM can be used for a variety of applications, such as the surface structural characterization of crystal materials, adsorption and film growth, electrochemistry, surface electronic structure, chemically selective imaging, bulk electronic structure,

electron-stimulated patterning, the positioning of single atoms [see Fig. 2.3(c, d)], nanolithography and the surface nanostructuring [77].

2.3.2 Introduction to surface nanostructuring

Recent years have witnessed the rapid progress in the field of nanotechnology, which have led to many potential applications for nanostructured materials. Nanostructures are crucial for devices in future information storage and processing, communications and biotechnology. The key feature that nanostructures offer such a diverse range of potential applications is the ability to tailor the electronic, optical, and magnetic structure and properties of materials. Surface nanostruturing techniques aim at building those nanostructures [78].

Conventional lithographic processes, which have been developed for the semiconductor industry for manufacturing microelectronic circuits and components, are incapable of fabricate the desired nanostructures as they tend to approach their fundamental size limits. Therefore, novel cost-effective and technically feasible fabrication techniques are highly demanded. The increased availability and quality of SPM instruments in recent years propelled the development of a number of SPM-based surface nanostructuring techniques, which allow us to fabricate complex nanostructures from constitutes small as individual atoms. The advantage of using an SPM-based approach is that the structures can be fabricated, characterized and modified by the same instrument, eliminating the contamination problem during the period of transportation when other approaches are used. In addition, this approach is also inexpensive, reliable and easy operative [79-81]. One of the challenges using this approach is that the

fabrication speed is relatively low as only a single probe can be used. Probe-tip arrays may overcome the problem [82].

2.3.3 Nanostructuring on semiconductor surfaces using a scanning tunneling microscope

Besides surface characterization, the STM can be used to fabricate nanostructures on different substrates, including polymers, metals, semiconductors, and ceramic materials, in a precise location and with a predefined pattern. Compared to conventional lithography processes such as EBL and photolithography, nanostructures fabricated by the STM feature more advantages including ultrahigh spatial resolution, inexpensive equipment and relatively convenient operation. Ultrahigh spatial resolution is achieved by the nanoscale electrostatic, electrochemical and thermal energy sources induced by the STM tip through the tip-substrate gap, because the tunneling current can be treated as a miniature electron beam at a diminishing scale. Five types of surface nanostructuring can be performed: material modification, material deposition, material remove and atomic manipulation.

Material structures, especially those on the surfaces, can be changed through material modification using an STM. Surface nanostructuring on Si is one of the typical applications. In 1989, Van Loenen *et al.* made indentations with diameters of 2-10 nm on Si (110) and Si (001) surfaces using the W tip of an STM mounted in an Ultrahigh Vacuum (UHV) chamber [83]. Later, Dagata *et al.* fabricated lines and dots with 100-nm resolution on hydrogen-passivated Si surfaces using an STM operated in open air, and suggested that these features arise from electronic structure effect rather than from topographic differences between the modified and unmodified substrates [84]. Using

pulsed voltage across the tunneling gap of an STM, Yau *et al.* fabricated permanent nanostructures with the feature size of 10 nm on chemically prepared Si surfaces, and concluded that the features are topographic structures rather than electronic consequences. They attributed the modifications to chemical activation of loosely bounded hydrocarbon clusters triggered by the voltage pulses [85]. Hartmann *et al.* used an STM to locally modify p-n junctions on a scale of a few tens of nanometers, and obtained electronically active nanostructures with the feature size of 50 nm under conditions of high current densities and forward-bias p-n junction. Barniol *et al.* used an STM operated in open air under normal imaging conditions to fabricate nanostructures with the feature size of 25 nm on hydrogen-passivated Si (100) surfaces, and affirmed that the modifications come from the combination topographic changes with electronic structural changes by the simultaneous acquisition of topographical, current image tunneling spectroscopy and local barrier-height images [86]. Snow *et al.* fabricated Si nanostructures, line patterns with line width of 25 nm, on HF-passivated Si (100) surfaces by direct chemical modification with an STM operated in open air followed by a liquid etching process, and predicted the sub-10 nm are feasible using this technique [87].

Material modification can be performed on metal surfaces using an STM. Matsumoto *et al.* used an STM in open air to oxidize lines completely through a thin (3 nm) Ti film deposited on insulating substrates. Using different applied bias, they fabricated oxidized lines with different line widths varying from 20 to 35 nm. These oxidized lines were used as tunnel barriers to isolate small Ti islands, and single electron transistors at room temperature thus formed [88]. Xie *et al.* applied a STM to induce oxidation in a Cr film and the induced Cr oxide acts as a mask for the subsequent CR-14

Cr etching [89]. Material modification using STM can be performed on ceramic material surfaces. Day *et al.* selectively oxidized Si_3N_4 surfaces using an STM operated in open air with a Pt-Ir tip. Those patterns in the nitride film were then transferred to the underlying Si with an ammonium fluoride etching [90].

Another application of nanostructruing with an STM is material deposition, in which the STM serves as a miniature emission source. When a gap voltage is applied, atoms or nanoparticles at the tip apex can be deposited onto the sample surfaces within the tunneling range. Houel *et al.* deposited Pt dots and lines on n-type Si substrates by Pt STM tips and pulsed gap voltages [91]. Fujita *et al.* fabricated sequential Ag dots on an n-type Si (111) substrate with the pitch equal to the pitch size obtained using an Ag-coated W tip [92]. Deposition of other materials from precursors like SiH_4 and SiH_2Cl_2 and Si- and Ge-based nanostructures with lateral sizes of 10 nm were also successfully demonstrated by Rausche *et al.* [93].

STM can be used to remove materials from a nanometer-sized region of substrate surfaces. Nanolithography on SiO_2/Si surface is a typical example. Iwasaki *et al.* used a field-emitted electron beam extracted from the STM to selectively remove the oxide film by e-beam-induced reduction and thermal annealing, and fabricated the patterns with a feature size of 25 nm on SiO_2/Si surfaces. Single atoms can be manipulated by an STM [94]. Hla et al made a quantum corral nanostructure from Ag atoms on a Ag (111) surface [95]. Avouris *et al.* demonstrated that atoms can be decomposed from a Si (111) surface to the tunneling tip, and deposited elsewhere on the substrate [96]. Salling *et al.* wrote nanoscale trenches in Si (100) surfaces with a 2.4 nm resolution from Si films that are only three atomic layers thick [97].

2.3.4 Nanostructuring on semiconductor surfaces using a laser-assisted scanning tunneling microscope

Microstructures fabricated by laser microprocessing have been widely applied in semiconductor and data storage industry. Comparably, the fabrication of nanostructures is difficult due to the optical diffraction limit. In combination with an STM, this diffraction limit can be overcome using an STM tip by taking advantages of near-field optics. Compared with surface nanostructuring with an STM only, Laser-Assisted STM (LASTM) with additional energy source of lasers is more powerful. For example, the lasers can be used to generate a thermovoltage, induce thermal expansion and excite photoelectrons. The ways to fabricate nanostructures include nanoindentation due to the mechanical contact between the STM tip and the sample surface, nanoscale surface heating by the enhanced optical field attributed to laser-STM tip coupling, chemical desorption of atoms from the sample surface by the increased tunneling current, enhanced chemical interaction between the STM tip and the sample surface, and dissociation and deposition of gas species between the STM tip and the sample surface [98]. Therefore, LASTM provides a wide variety of potential applications in nanoscience and nanotechnology. Examples of such applications include surface repair, the fabrication and characterization of nanoelectronics and nanophotonics, and the machining and aligning of nanoparticles and nanotubes.

In 1985, Wessel proposed that the combination of lasers with an STM can provide a localized and enhanced optical fields under the tip apex by which nanostructures would be generated just underneath the tip apex using the effects of thermal or photochemical damage. At that time, he envisioned the technique might be applied to high-density

optical data storage and the fabrication of Very Large Scale Integrated Circuits (VLSIC) and X-ray optics [70].

In 1990, Liu *et al.* performed the etching process on CdSe semiconductor film with a He–Ne laser, and observed that the film with a 20-nm thickness was modified to create holes located only underneath the tip apex. They attributed this formation to a dry electrochemical process, in which photoelectrons are injected from the semiconductor into the tip, to create holes at the surface, leading to a local decomposition of the film [99].

Later, Gorbunov *et al.* used a mode-locked Ti/Sapphire laser with a Ag tip to produce hillocks on Au surfaces with diameters of 20 - 40 nm and a height of 10 - 20 nm. They presented the theoretical possibility and mechanisms of the near-field enhancement of optical radiation by very small conductive objects [100]. Followed this experiment, Jersch *et al.* used an STM in combination with laser excitation to modify metal surfaces in open air, and fabricated nanostructures of craters, ditches and hillocks with a lateral resolution of approximately 10 nm. This experiment was conducted on Au and Au/Pd substrates with W, Ag, and platinum (Pt)/Iridium (Ir) tips. They found that with Ag-coated W tips, pure Ag tips, and Pt/Ir tips hillocks were created, whereas pure W tips produced holes. Field evaporation was used to explain this occurrence [101].

Lu *et al.* are the pioneers of using the technique to fabricate nanostructures on semiconductor surfaces like Si and Ge substrates. They fabricated a 3×2 dot array and a single line with feature sizes ranging from 20 to 30 nm on hydrogen-passivated Si (100) surface with a pulsed Nd:YAG laser and an STM operated in open air [102]. They also created a 2×2 dot matrix with dot sizes between 20 and 30 nm on hydrogen-passivated

Ge (100) surfaces [103]. The nanostructures produced in this way appeared as depressions in STM images but elevations in AFM images, and were attributed to local photothermal oxidation of the surface promoted by field enhancement. The oxide formation was verified using Auger Electron Spectroscopy (AES). Two mechanisms, optical enhancement and thermal mechanical indentation, were proposed to explain the surface modification [104].

Single atoms were successfully deposited on Si (001) surfaces from a W tip by Ukraintsev *et al.* in an UHV environment with 8-ns-long pulses of a frequency-doubled Nd:YAG laser. The process was accompanied by a strong transient increase of the tunneling current. They attributed the deposition to a considerable temperature rise of the tip due to the localized optical field [105].

Boneberg *et al.* investigated the mechanism of nanostructuring based on nanosecond laser irradiation of an STM tip. The observation of a transient increase of the tunneling current on the time scale of μs is indicative of thermal expansion, which amounts to several nanometers for the necessary energy density of nanostructuring. Furthermore, they suggested quantized electrical resistance can be observed upon illumination, which shows the formation of mechanical contact between the tip and the surface [106].

CHAPTER 3 NUMERICAL SIMULATION OF OPTICAL FIELDS INDUCED BY SILICA MICROPARTICLES, METALLIC TIPS, AND METALLIC NANOSTRUCTURES

3.1 Introduction

Knowing the optical field distribution underneath the tip apex or at the backside of the microparticles along the light propagation direction is critical to optimize the experimental conditions under which the Raman enhancement can be maximized or the smallest nanostructures could be achieved. For the field enhancement by tips, the conditions include the tip material (plasmonic material, lightning-rods or dielectrics), the tip shape (spheroid, cone, ellipsoid or pyramids), the laser illumination (polarization, incident angle, and wavelength), the laser type (continuous or pulsed), and the substrate type (dielectrics or metals) [1]. Different algorithms, including the Discrete Dipole Approximation (DDA) method, the Finite-Different-Time-Domain (FDTD) method, the T-matrix method, the Finite Element (FE) method, the Multiple Multipole (MMP) method, and the Modified Long Wavelength Approximation (MLWA) method, have been developed to calculate the optical field [2].

The electronic resonance, the lightning-rod effect and the optical antennas are the three enhancement mechanisms involved in the simulation for tip enhancement. Denk *et al.* generalized the modeling of the tip by studying the eigenvalues of hyperboloids with boundaries stretching to infinity and the presence of a plane, and claimed that the enhancement factor as high as 2,000 can be achieved when wavelengths are close to the surface plasmon excitation [3]. Zayats *et al.* studied the influence from the substrates under the resonance conditions of an ellipsoid particle made of different metals. Their investigation revealed that the main resonance red-shifts when the particle-surface separation becomes smaller [4]. Martin *et al.* calculated the field intensity underneath a W tip on a glass substrate, and found that the enhancement factor of 100 for certain

excitation conditions can be achieved. Their findings indicate that the field enhancement is not necessarily limited to the metal surfaces on which surface plasmons would occur and to the tips which support Plasmon resonance [5]. Notingher *et al.* integrated the samples and the substrates into their models, and concluded that the electric properties of the samples and the substrate have significant impact on the field enhancement at the tip apex. They suggested that the Raman intensity can be well optimized by tuning the geometry factors and electric properties of the materials. In general, they believed the strongest enhancement tends to occur for the cases where the metal is employed [2]. By calculating the surface charges localized along a Au tip for two different excitation polarizations using the MMP, Novotny *et al.* showed that if the polarization is aligned with the tip axis, the density of the surface charges is maximized at the tip apex, leading to an enhanced optical field [6]. Sun *et al.* systematically studied the effects of a number of parameters, e.g., the polarization, the incident angle, the wavelength of the incident laser, the tip material, and the tip length, on the field enhancement, and concluded that those parameters have a significant influence on the enhancement and that care must be taken in the design of the experiment in order to maximize the near field [7]. Bohn *et al.* investigated the antenna effect of a Si tip, which is a material without resonance, by including the effect of a dielectric substrate very close to the apex of the Si ellipsoid. They found that if a certain geometric condition is satisfied, an enhancement factor of 250 can be achieved [8].

The algorithms also have been applied to calculate the field distribution around dielectric microparticles when illuminated by lasers. Li *et al.* studied the distribution of the optical field within and in the vicinity outside a dielectric particle illuminated by a

plane electromagnetic wave, using the Lorenz-Mie theory and the FDTD method for spheres and spheroids, respectively. They found that the electric and magnetic energy densities are locally different within the microparticles, and predicted the potential applications of this technique to Raman and fluorescence spectroscopy [9]. Chen *et al.* reported the first evidence of localized nanoscale jets generated at the backside of circular dielectric cylinders illuminated by a plane wave. They found that these nanojets have waists smaller than the diffraction limit and can propagate over several optical wavelengths without significant diffraction, and such nanojets can enhance the visible light scattered by dielectric nanoparticles located within the nanojets by several orders of magnitude. They also suggested that this technique may provide a new means to detect and image nanoparticles of size well below the diffraction limit applied in ultramicroscopy for detecting proteins, viral particles, and even single molecules [10]. Lecler *et al.* studied the nanojects generated by a sphere with several wavelengths in diameter, and found that when light is focused on the surface of the sphere, the width of the beam stays smaller than the wavelength along a distance of propagation of approximately two wavelengths and reaches a high intensity [11]. Itagi *et al.* systematically studied the detailed optics of photonic nanojets generated by a normal plane-wave incidence on dielectric cylinders. They summarized that the jetting of the nanoscopic optical spot over many wavelengths is a result of a unique combination of features in the angular spectrum, the finite content of propagating spatial frequencies, a small but finite content of evanescent spatial frequencies, and a peculiar distribution of the phase. They also presented that the effect is a result of the combination of the shape and size of the particle and the refractive index ratio [12].

3.2 Simulation method

The FDTD method is frequently used to simulate all wave effects including propagation, scattering, diffraction, reflection and polarization. It also can be used to model material anisotropy, dispersion, and nonlinearities. Recently, it has been demonstrated that this method can be extended into the areas of biophotonics, biomedical, and nanostructures. In this project, the optical fields induced by three structures including microparticles, metallic tips and metallic nanostructures were performed using this method based on the Lorentz-Drude model. Incorporating the Lorentz-Drude model solves the problem arising from the conventional optics in which only the surface effect is taken care of. In comparison, this approach includes the electromagnetic field effects on nanoparticles by considering the optical penetration to the metal surfaces which will affect all the wave properties such as near field, far field, scattering and diffraction.

The Drude dispersive model for surface plasmons in the frequency domain can be expressed as [13, 14, 15]

$$\varepsilon_r^f(\omega) = 1 + \frac{\Omega_p^2}{j\Omega\Gamma_0 - \omega^2}. \tag{3.1}$$

The Lorentz model is expressed as

$$\varepsilon_r^b(\omega) = \sum_{m=1}^{M} \frac{G_m \omega_p^2}{\omega_m^2 - \omega^2 + j\omega\Gamma_m}. \tag{3.2}$$

Here, ω_p is the plasma frequency, m is the number of oscillators with the resonant frequency ω_m, and the life time $1/\Gamma_m$, Γ_m is the damping factor or collision frequency. $\Omega_p = (G_m\omega_p)^{1/2}$ is the plasma frequency associated with interband transitions with oscillator strength G_0 and damping constant Γ_0.

In modeling, a complex dielectric function, $\varepsilon_r(\omega)$, for the W tip based upon the Lorentz-Drude model in frequency domain is given by

$$\varepsilon_r(\omega) = \varepsilon_{r,\infty} + \sum_{m=0}^{M} \frac{G_m {\Omega_m}^2}{{\omega_m}^2 - \omega^2 + j\omega\Gamma_m} . \tag{3.3}$$

Here, $\varepsilon_{r,\infty}$ is the relative permittivity in the infinity frequency.

Using the polarization principle in the Maxwell equations, the transformation of Eq. (2.3) from frequency domain to time domain can be expressed as

$$\mu_0 \frac{\partial \vec{H}}{\partial t} = \nabla \times \vec{E} , \tag{3.4}$$

$$\varepsilon_{r,\infty}\varepsilon_0 \frac{\partial \vec{E}}{\partial t} + \sum_{m=0}^{M} \frac{\partial \vec{P}_m}{\partial t} = -\nabla \times \vec{H} , \tag{3.5}$$

$$\frac{\partial \vec{P}_m}{\partial t^2} + \Gamma_m \frac{\partial \vec{P}_m}{\partial t} + {\omega_m}^2 \vec{P}_m = \varepsilon_0 G_m {\Omega_m}^2 \vec{E} . \tag{3.6}$$

Here, P_m is the dispersive polarization denoting the nonlinear polarization, G_m is related to the oscillation strengths, μ_0 is the permeability of vacuum, and ε_0 is the permittivity of free space. Using the finite-difference technique to solve Eqs. (2.4) to (2.5), we can generate the FDTD scheme [15].

3.3 Optical fields induced by silica spherical microparticles

Two physical models used to simulate the electrical field around a silica microparticle with and without the presence of a substrate are shown in Figs. 3.1(a) and 3.1(b), respectively. The particle has a diameter of D_p, and the incident laser has a beam waist of D_l. The parameters n_1, n_2, and n_3 are referred to as the refraction index of air, the particle and the substrate at the irradiate wavelength of 514.5 nm, which are 1.0, 1.4 and

4.24, respectively. The extinction coefficient of Si is 0.06. The laser has a Gaussian beam shape with a waist of D_l = 2.5 μm. The amplitude of the electric field is 1 V/m. The light propagates along the positive Z direction, normal to the surface of Si substrates. The incident light is polarized in the Y direction.

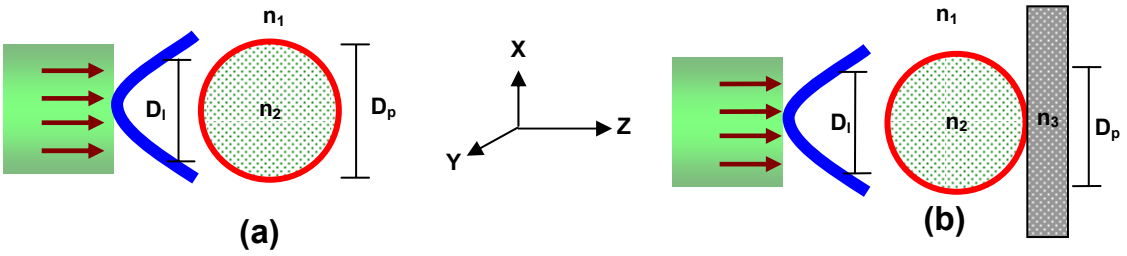

FIGURE 3.1 Physical models for the formation of nanojets by microparticles, (a) without the substrate and (b) with the substrate. D_l: beam waist; D_p: particle diameter; n_1, n_2, n_3: the index of refraction of air, the particle and the substrate. The incident light is polarized in the Y axis.

The calculated electric fields in the XZ plane at Y = 0 for the particles with the diameter of 1.01 μm and 2.34 μm without the Si substrates are shown in Figs. 3.2(a) and 3.2(b). It can be seen that the fields inside the particles are not uniformly distributed with a manner of caustics. The electric fields are focused in the forward direction along the incident light near the shadow surface. They resemble jets from a space shuttle when launching but with nanometer sizes, so they are called nanojets. Although for two cases the fields of the nanojets are different, with a higher one for the larger particle, their waists are almost the same, around 100 nm, which is similar to the reported results [10]. The phenomenon indicates that the nanojet waist is independent on the particle size. On the other hand, there is a large difference on the length of the nanojets for different particles. The strongest electric fields occur inside the particles in Fig. 3.2(a) while it appears outside the particles in Fig. 3.2(b). This is due to the larger internal reflection

resulting from the inner side of the shadow surface of the particles of 2.34 μm compared to that of the particles of 1.01 μm.

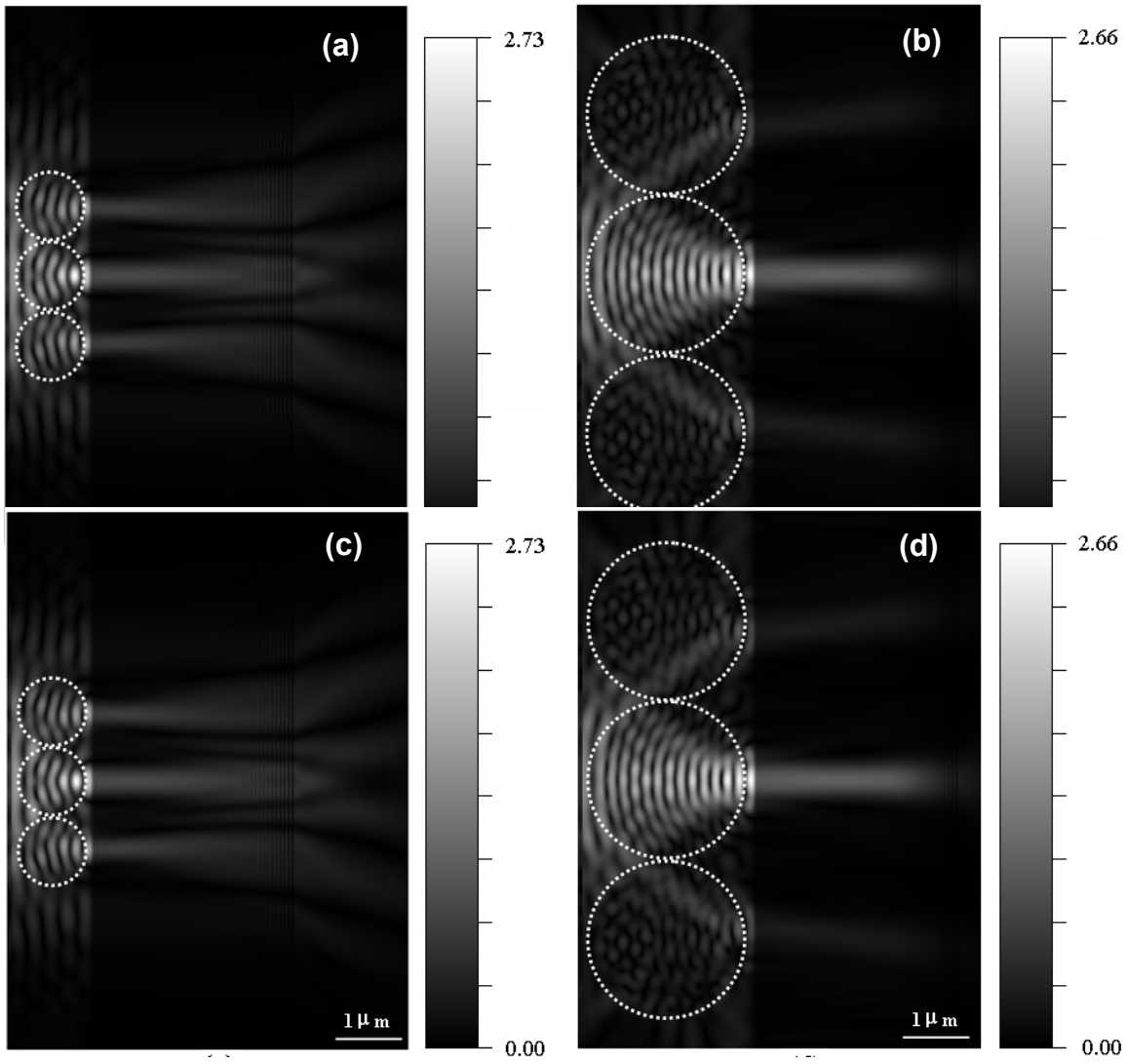

FIGURE 3.2 Calculated distributions of the electric fields for the different sizes of particles with and without the substrates from the *XZ* cross-sectional view using the software OptiFDTD™, (a) the particles of 1.01 μm without the substrate; (b) the particles of 2.34 μm without the substrate; (c) the particles of 1.01 μm with the substrate; (d) the particles of 2.34 μm with the substrate. The area in the white dotted circle indicates the location of the particles.

The calculated electric fields for the particles of 1.01 μm and 2.34 μm on the Si substrates are shown in Figs. 3.2(c) and 3.2(d). The distributions of the electric fields are

significantly changed due to the presence of the high-index substrates. Interestingly, even though the beam waists are not changed, the lengths of nanojets become much smaller, shrinking into about 100 nm from 120 nm. This result indicates that the electric field is well confined on the surface of substrates in a nanoscale region, overcoming the conventional optical diffraction limit. Since the presence of the substrate can be used to change the field distributions, it is possible that selecting a substrate with an adequate refraction index might give rise to nanojets with diameters less than 100 nm. When varying the particle sizes from 0.33 to 5.08 μm, the amplitudes of the electric fields vary, as shown in Fig. 3.3.

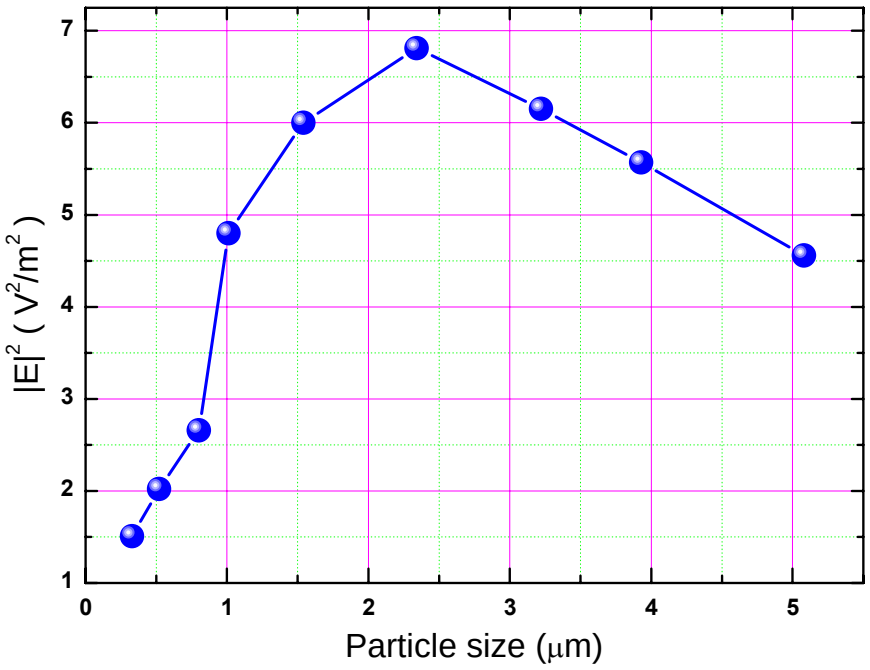

FIGURE 3.3 $|E|^2$ as a function of the particle size.

The square of the amplitude, $|E|^2$, which is proportional to the optical intensity, as a function of the particle, is shown in Fig. 3.3. It can be observed that the curve has a peak at 2.34 μm. The peak value is slightly less than 7 V^2/m^2. This peak corresponds to those particles with the diameters approximating the beam diameter. All particles, although they are different in diameter, can increase the optical intensity at the interface to a certain degree. The localized and enhanced optical fields can be used in Raman spectroscopy for the detection of substances in nanoscales.

3.4 Optical fields induced by tungsten tips

In this simulation, the tip apex is modeled as a semi-sphere. As illustrated in Fig. 3.4, a W tip is assumed to be placed above a flat Si surface. The tip-surface gap is illuminated by a continuous plane wave with a transverse Gaussian profile which propagates along the *k* direction (*Z* axis). The tip axis (*X* axis) is hence perpendicular to the *k* direction.

The influences of the beam polarization, the tip radius, and the Si substrate were investigated. Specifically, the tips with radii (*r*) ranging from 15 to 50 nm were used to approximate the practical conditions. A typical tip-surface distance (*H*) was selected to be 1 nm. The electric field of the plane wave was 1 V/m.

Figures 3.5(a) and 3.5(b) show the images of the electric field distributions around a 10-nm-radius W tip with the laser polarization in parallel with or perpendicular to the tip axis, respectively. The simulation results show that a polarization in parallel with the tip axis is required to achieve a strongly enhanced optical field underneath the tip apex. Lightning-rod effects can be used to explain this enhancement phenomenon. The free electrons in the tip react to the external electromagnetic excitation by inducing surface

charges. Due to the presence of a geometrical singularity, the local surface charge density is drastically increased in the near field of a tip apex, leading to a localized optical enhancement. In the following simulations, the laser polarization is kept in parallel with the tip axis [7].

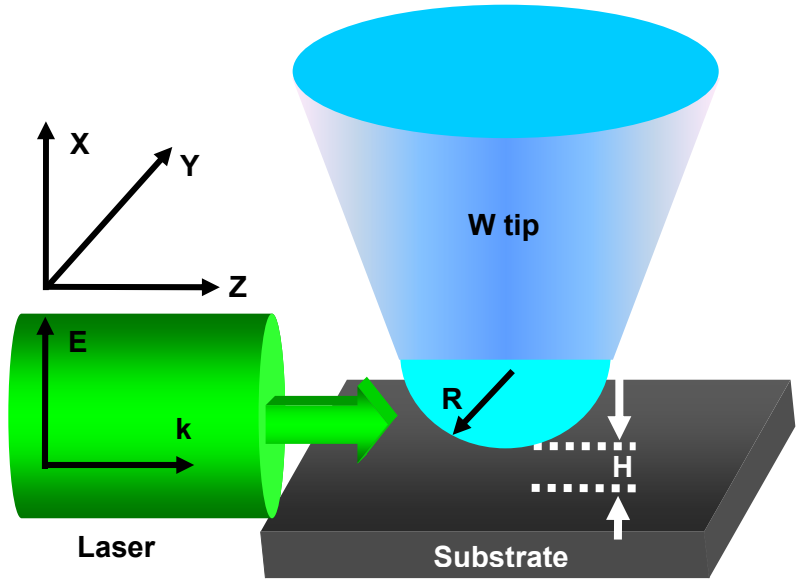

FIGURE 3.4 Representation of an STM tip under laser illumination used in the FDTD simulation.

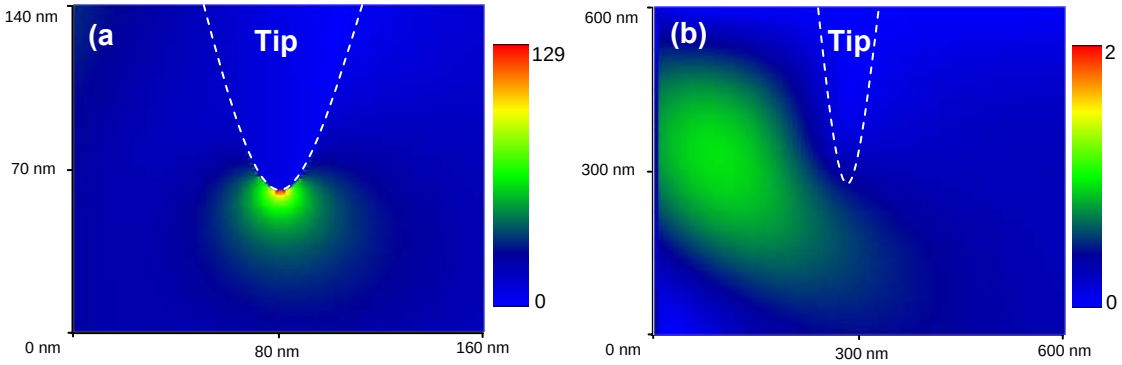

FIGURE 3.5 Images of the electric field distributions near a W tip with a 10-nm radius, irradiated by a laser beam with the polarization (a) in parallel with and (b) perpendicular to the tip axis.

Figures 3.6(a) and 3.6(b) show the images of the electric field distributions around a tip of a 25-nm radius with and without the presence of the Si substrate. Figures 3.6(c) and 3.6(d) show the images of the electric field distributions around a tip of a 50-nm radius with and without the presence of the Si substrate. It can be observed that the optical field is enhanced more strongly for the tip of a smaller radius. The enhanced optical fields are mostly constrained in an area of 10×10 nm^2. In addition, it can also be observed that the enhancement in the presence of the substrate is over 2 times stronger than the case in the absence of the substrate, indicating that the interplay between the substrate and the tip apex is significant.

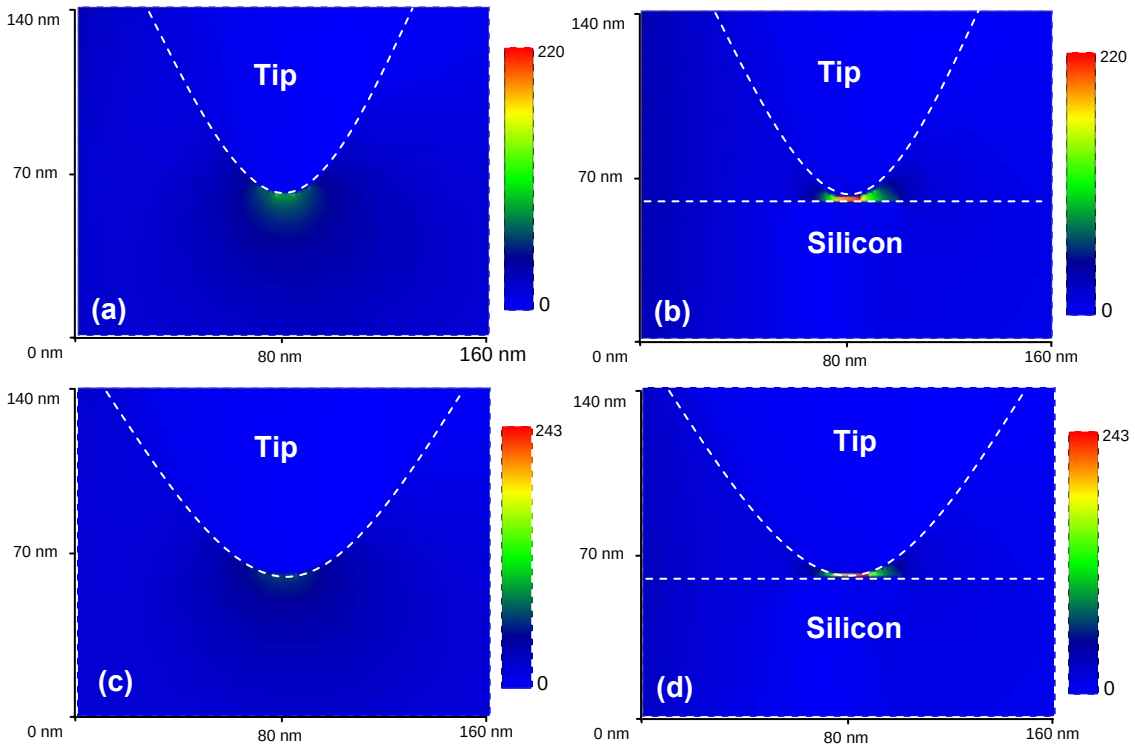

FIGURE 3.6 Images of the electric field distribution around (a) a 25-nm-radius tip alone, (b) a 25-nm-radius tip in the presence of the Si substrate, (c) a 50-nm-radius tip alone, and (d) a 25-nm-radius tip in the presence of the Si substrate.

Figure 3.7 shows the images of the electrical field distributions underneath a 25-nm-radius tip with the presence of a Si substrate under different tip-surface gaps of (a) 1 nm, (b) 3 nm, (c) 5 nm, and (d) 7 nm. It can be concluded that the optical field is enhanced more strongly for a smaller tip-surface gap, indicating that the interplay between the substrate and the tip apex is stronger when the tip and the substrate surface are closer. As a result, we can fabricate small structures by keeping the tip-surface distance as small as possible. The enhanced optical fields are mostly constrained in an area of 10×10 nm^2.

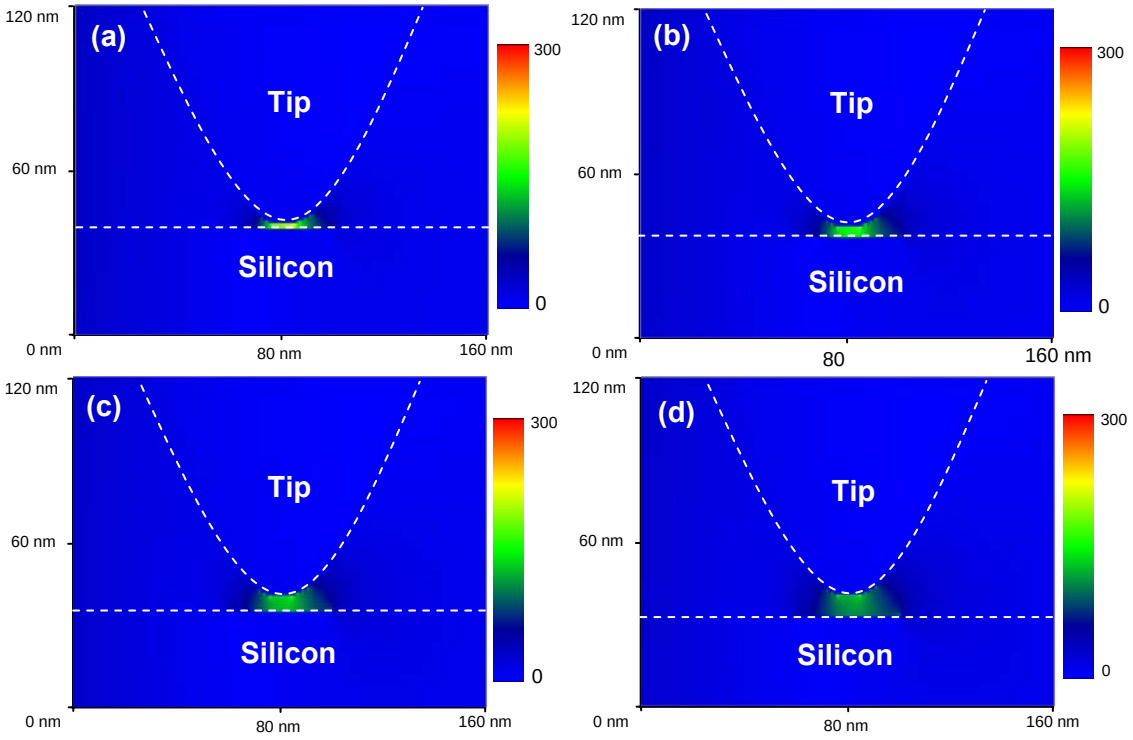

FIGURE 3.7 Images of the electrical field distributions around a 25-nm-radius tip under different tip-surface distances of (a) 1 nm, (b) 3 nm, (c) 5 nm, and (d) 7 nm with the presence of the Si substrate.

3.5 Optical fields induced by Ag tips

The physical model is depicted in Fig. 3.8(a). The influence of the substrates on the field enhancement was taken into account for better accuracy.

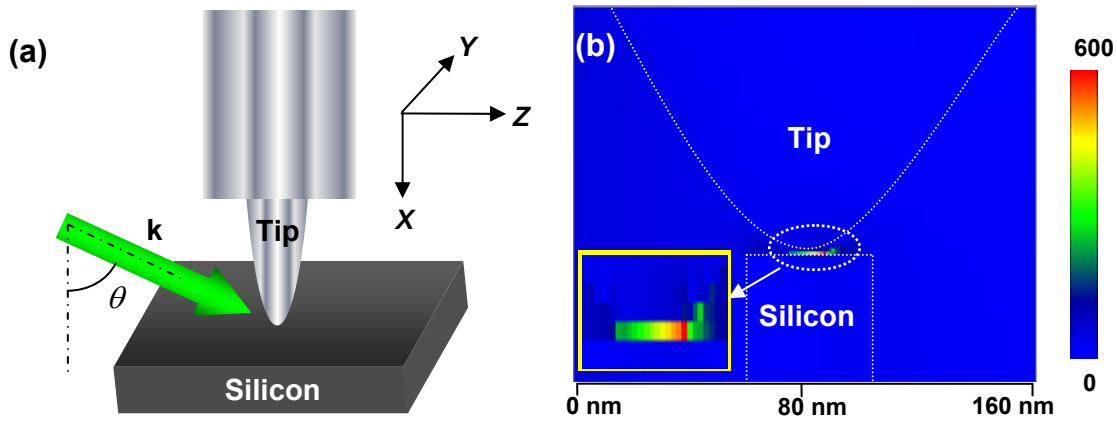

FIGURE 3.8 (a) Physical model for the simulation of electric field distributions underneath a Ag tip; (b) Optical field distribution in the proximity of a Ag tip illuminated by a 514.5-nm laser beam. The inset is a zoomed view of the optical field distribution.

As illustrated in Fig.3.8 (a), a conical Ag tip is placed above a flat Si surface. The tip-surface gap is illuminated by a continuous-wave laser with a wavelength of 514.5 nm propagating along the *k* direction. The incident angle is 65° with respect to the tip axis (*X* axis). The tip apex radius is 50 nm. The tip-sample distance is 1 nm. The electric field amplitude of the beam is assumed to be 1 V/m. The mesh step is 0.5 nm, uniform for each axis. Figure 3.8(b) shows the calculated electric field distribution. It can be observed that the electric field as high as 600 times is locally enhanced in the space between the tip apex and the substrate surface in a region of 14 nm along the *Z* axis, indicating that a spatial resolution of 14 nm could be achieved.

3.6 Optical fields induced by the interactions between Ag nanostructures and tips

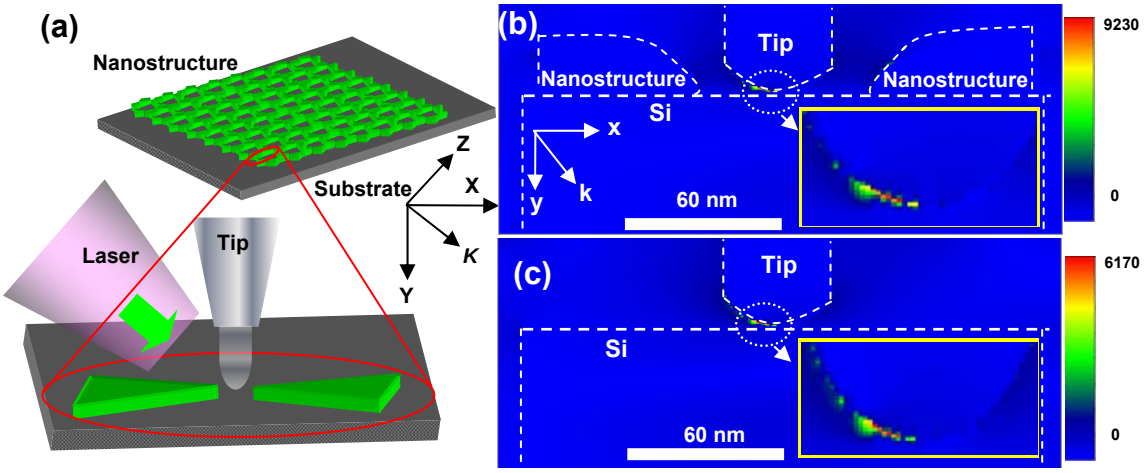

FIGURE 3.9 (a) Physical model to simulate the optical field beneath a Au tip under a laser irradiation. Electric field distribution beneath a Au tips (b) in the presence of the nanostructures and (c) in the absence of the nanostructures simulated by the FDTD algorithm. Insets in (b, c) show zoomed views of the electric field distributions.

The physical model is depicted in Fig. 3.9(a). This model has taken the Si substrate into consideration. One conical Au tip with a diameter of 50 nm is placed 1 nm above the Si substrate and illuminated by a continuous-wave laser with a transverse Gaussian profile and a wavelength of 514.5 nm propagating along the *k* direction which is 70° with respect to the substrate normal. The tip apex diameter is 50 nm. The height of nanostructures is 30 nm with a 75-nm terminal distance. The mesh step for each axis is 0.5 nm. Figures 3.9(b) and 3.9(c) show the electric field distributions beneath the tip along the *XY* plane in the presence and in the absence of Ag nanostructures, respectively. From Fig. 3.9(b), the enhanced electric field is confined in a 1-nm range but spreads a distance of 20 nm along the *X* direction. A higher local electric field (1.5 times) is found in Fig. 2.9(b) than

in Fig. 3.9(c), indicating the obvious impact of the nanostructures on the field enhancement.

The Raman intensity is approximately proportional to the fourth power of the field amplitude. Therefore, the presence of nanostructures can further enhance the Raman signals by more than 5 times, similar to the enhancement from the Au sharp step [16].

3.7 Conclusion

Using the Finite Difference Time Domain (FDTD) method and the Lorentz-Drude model, theoretical calculations of optical near fields induced by microparticles, the tips made of W, Ag and Au, and Ag nanostructures were performed. Nanojets, with apparently enhanced intensity and a diameter of 100 nm, were found at the backside of the micropartcles along the optical propagation direction. The intensities within the nanojets are dependent on the particle sizes. When the particle size approximates the beam diameter, the maximum optical intensity is achieved, corresponding to the maximum Raman enhancement. However, the influence of particle sizes on the diameter of the nanojets is slight. The presence of the substrates and the distance between the tip and the substrates can influence the optical fields. The tip assisted by Ag nanostructures was found capable of further enhancing the optical field. Those findings from the simulations provide us a compass to design the experiments.

CHAPTER 4 DEVELOPMENT OF A MICRO- AND NANO-RAMAN SPECTROMETER

4.1 Introduction

Raman scattering is an inelastic light scattering process in which an excitation source, e.g., laser photon, bounces off molecules and losses a certain amount of energy. The laser photons with less energy scattered from the surface of the sample exhibit a frequency shift. The various frequency shifts associated with different molecular vibrations give rise to a spectrum from which a specific compound can be characterized. Raman spectroscopy (RS) based on Raman scattering has a variety of applications due to the unique capability of chemical identification [1]. Until the combination of RS with optical microscopy, i.e., the emergency of the micro-RS, it has not played an important role in material science and industry in history. The sensitivity, lateral and axial resolution of RS are much improved by objective lens with high Numerical Aperture (NA) and more compact optical path which are available in microscope. In general, the lateral or spatial resolution of a micro-Raman spectrometer is 1 μm, and the axial or depth resolution is 2 μm. Equipped with a motorized XYZ stage, a laser spot scanner or a galvanometer mirror-type scanner, the micro-Raman spectrometer is used to characterize the composite distribution on a sample surface visualized by two-dimensional (2D) or three-dimensional (3D) images [2, 3]. UV, visible and infrared Raman is categorized by different laser sources, which are used for the dispersive Raman spectrometer. Raman signals excited by UV light are much enhanced for some materials like carbon films due to resonance effect [4]. The drawbacks of the UV RS, such as high cost, low detection sensitivity and difficulty in system adjustment, render it not as popular as the visible and infrared Raman. The infrared Raman is a good choice for suppressing the fluorescence associated with the Raman excitation. Although the high fluorescence causes visible

Raman less competent than infrared Raman, it is still widely applicable partially because most detectors like CCD devices in the infrared region are inefficient but efficient in the visible range. Meanwhile, the influence of the fluorescence can be reduced to a certain degree if the optical efficiency and the sensitivity of detector are improved. FT-Raman is another kind of Raman system using Fourier transform algorithm to identify Raman signature instead of using dispersive spectrometer [5].

There have some efforts to make the Raman system more compact, cheaper and operable remotely. Brian *et al.* developed a handheld Raman instrument using an acousto-optic tunable filter suitable for field operation [6]. Kim *et al.* designed a Raman spectrometer with mapping functionality using a commercial Compact Disc Optical Pickup Unit (CD-OPU). The performance can be improved if the CD-OPU is replaced by an OPU used in a Blue-ray Digital Versatile Disc (Blu-ray DVD) drive since the NA of a DVD objective lens (0.8) is higher than that of a CD-OPU (0.55) [7]. Paipetis A. *et al.* designed a remote Raman spectrometer with a confocal remote optical fiber for medical applications, testing under extreme environment and explosive detection [8].

Most of the improvements for RS can be immediately employed in industry. For example, the RS has been applied to test impurity, contamination, temperature profile, crystalline orientation and stress in semiconductor devices [9]. One-dimensional (1D), two-dimensional (2D) or three-dimensional (3D) Raman fingerprint from the interested area of devices is mapped by a confocal or non-confocal micro-RS. The Raman image can be constructed under three criteria: the integral of the spectral window, the average of the spectrum window and the peak intensity. It is laborious to obtain a 2D and 3D Raman image where several thousands or even tens of thousands Raman spectra need to be

acquired. The sample size, the accumulation time and the spatial resolution determine the total measurement time. The point to point probing is the most time-consuming method compared with the line and the global scanning, but it can capture the image with high resolution and high contrast. A 2D detector like a micro-channel plate Photo Multiplier Tube (PMT) and a line laser beam are used in a line Raman scanning so that Raman spectra from a thousand points can be obtained simultaneously, which can dramatically reduce the testing time [10]. Early in 1990, based on a 2D detector, Veris *et al.* developed an imaging Raman system capable of collecting 1024 spatial resolved spectra. The image with 66,560 Raman spectra from an 8×6 mm^2 area on a partially stabilized Zirconia were acquired and analyzed in 5.4 hours to produce a 2D map of the fraction of a tetragonal phase transformed to a monoclinic phase during a crack propagation [3]. The fastest method is global mapping, in which the wide-field Raman maps can be obtained from a one time measurement and a 2D detector is responsible for the spatial discrimination. For small mapping area in nanoscales, the line and the global scanning have the advantage of reducing the testing time dramatically. However, for microscale mapping, the serious degradation on Raman intensity and relatively low signal to noise ratio (SNR) for most materials cause the line and the global scanning unrealistic.

A huge amount of data needs to be processed and the control instructions need to be synchronized in the entire Raman mapping process. These works are generally handled by software. Integrating the functions of the data acquisition, the spectrometer control, the motion control, the data analysis and the map visualization into one suite is always a difficult task, especially when the system requirements are very critical.

The conventional RS faces two challenges: 1) the inherent weak scattering sensitivity resulted from its small interaction cross-sections (10^{-29} cm^2/molecule) and 2) the low spatial resolutions (1 μm) due to the optical diffraction limit [11]. To face the challenges, different schemes have been proposed, such as the near-field RS (NFRS), the surface-enhanced RS (SERS) [12], and the tip-enhanced RS (TERS) [13]. These schemes are based upon one or more mechanisms of the electromagnetic enhancement, the chemical enhancement, and the near-field effects. The NFRS, as referred to as an aperture RS, has demonstrated a spatial resolution of 100 nm by employing an aperture with a diameter of 100 nm on a tapered fiber tip or micropipette [14]. Further resolution improvement is nearly impossible because of the extremely low optical throughput of the optical fiber with diameters below 100 nm. The SERS employs rough metallic surfaces (Ag, Au, etc.) formed by grains, fractals, clusters, and nanoparticles to achieve presently the strongest Raman enhancement with an enhancement factor of 10^{14}. This enhancement is mostly explained by the LSPs induced by the rough metallic surfaces. The LSPs are charge-density oscillations confined to the metallic nanoparticles or nanostructures. The excitation of LSPs by an optical field with a resonant wavelength results in strong light scattering, the appearance of intense absorption bands due to surface plasmons (SP), and the enhancement of the local electromagnetic fields. This technique allows the sensing of an individual molecule. However, the morphologies of the metal surfaces, which ultimately determine the SERS effect, are uncontrollable, and hence severely limit the quantitative analyses of the SERS.

The TERS, on the other hand, makes use of a metallic tip to induce LSPs. Investigators found that a highly localized and significantly enhanced electromagnetic

field can be generated in the proximity of the metallic tip when irradiated by a laser beam [15, 16]. It is suggested that in addition to LSPs, lightning-rod effect may also contribute to the enhancement due to the geometric singularity. One can take the advantages of the localized field to improve both the lateral resolution and the detection sensitivity because the enhancement only occurs in a nanometer range dictated by the geometry of the tip apex. However, this evanescent field degrades rapidly along the light propagation direction. To make use of the local field, one must precisely control the tip-surface distance at a nanometer or angstrom level. Practically, the precise distance control can be realized by a SPM which uses either the atomic force for an atomic force microscope (AFM) or the tunneling current for an STM as the control variables. Both the AFM and the STM can provide atomic-resolution images by scanning a tip across sample surfaces and monitoring either the atomic force or the tunneling current. The RS in conjunction with the SPM may provide a new insight into the understanding of the morphology, electronic, thermal, chemical, mechanical, and optical properties of nanoscale materials and devices in a correlated fashion, eliminating the sample contamination during the transportation among different instruments. Recently, both the AFM- (RAFM) and the STM-combined (RSTM) RS have been reported. In the RAFM, the AFM works in the contact mode with a Au or a Ag coated Si tip as the light scatter. While in the RSTM, an STM runs in the constant-current mode with the tip above the sample surface in a tunneling range. Till now, most TERS-related reports on how to build TERS systems are focused on the RAFM, while only a few reports have systematic description of building the RSTMs. One typical RSTM example is that a high-resolution RSTM system was built using a parabolic mirror to study thin layers and nanostructures in an ultrahigh vacuum

[17]. However, the presence of the parabolic mirror not only increases the system complexity, but also adds difficulties to the optical alignment. So far, there is no report on how to perform fast and reliable optical alignment although it is a critical prerequisite to realize high Raman enhancement. Several instrument suppliers such as Tokyo Instruments, Renishaw, Witec, JPK instruments, and Jobin-Yvon are making strong efforts on developing a versatile and dynamic TERS system.

The RSTM offers many advantages over the RAFM, such as 1) better lateral resolution by precisely controlling the tip-sample gap distance, 2) gap modes resonances of the tip-sample configuration, and 3) feasibility of electronic properties characterization in conjunction with RS chemical identification. TERS systems can be categorized into the bottom and the side illumination. For transparent samples, the bottom illumination is more popular due to its high optical throughput and convenient optical alignment. For opaque samples, however, the side illumination is the only approach although it suffers from inconvenient optical alignment and strong background signals.

In this chapter, a low-cost, highly sensitive RS with 1D profile and 2D mapping functionality is reported first. The point to point probing method is chosen and the mapping time is much reduced with a highly sensitive CCD camera with a back-illuminated configuration and a high throughput delivery optics. The entire system, the optical path and the adjustment method are described in details. We choose Labview^{TM} as the platform to develop the testing suite because it provides powerful toolkits for the data processing, the motion control and the data visualization. The 2D Raman mapping can be viewed with both the flat 2D and the pseudo-3D mode. Instead of using normal mosaic display, the Raman image is visualized as true color transition mode, which is similar to

surface profile in the AFM. The Raman spectra as well as the maps can be given in real time so that the testing process can be monitored. The SWCNTs on the imprinted Si substrate and the patterned Si substrate were fabricated to evaluate the system performance. The Diamond-Like Carbon (DLC) film prepared by the Plasma Laser Deposition (PLD) was also studied using the developed instrument.

Secondly, an RSTM system using the side-illumination optics, with the capability of receiving both the far-field and the near-field Raman signals is developed. By using appropriate optical designs and three specific alignment steps, the fast and reliable optical alignment is achieved. Meanwhile, the far-field signals have been significantly suppressed by depolarization. As a result, a high contrast ratio has been achieved [18, 19]. The high contrast ratio allows the mapping of the nanostructures or the residual stress distribution in devices. This system can be converted to an RAFM system by simply replacing the STM nose cone with an AFM nose cone. The flexible transformation from RSTM to RAFM allows the nanoscale RS for both conductive and insulating samples.

The tip material and the geometry of the tip are important factors for the Raman enhancement. The preparation and the TERS performance of both the Au tips and the Ag-coated W tips are investigated in this study. Ag nanostructures fabricated on Si substrates by the Nanosphere Lithography (NSL) technique were used for the system evaluation because the LSPs induced by the nanoscale dipoles are promising to further enhance the local optical field in addition to the TERS.

4.2 Development of a micro-Raman spectrometer

4.2.1 System description

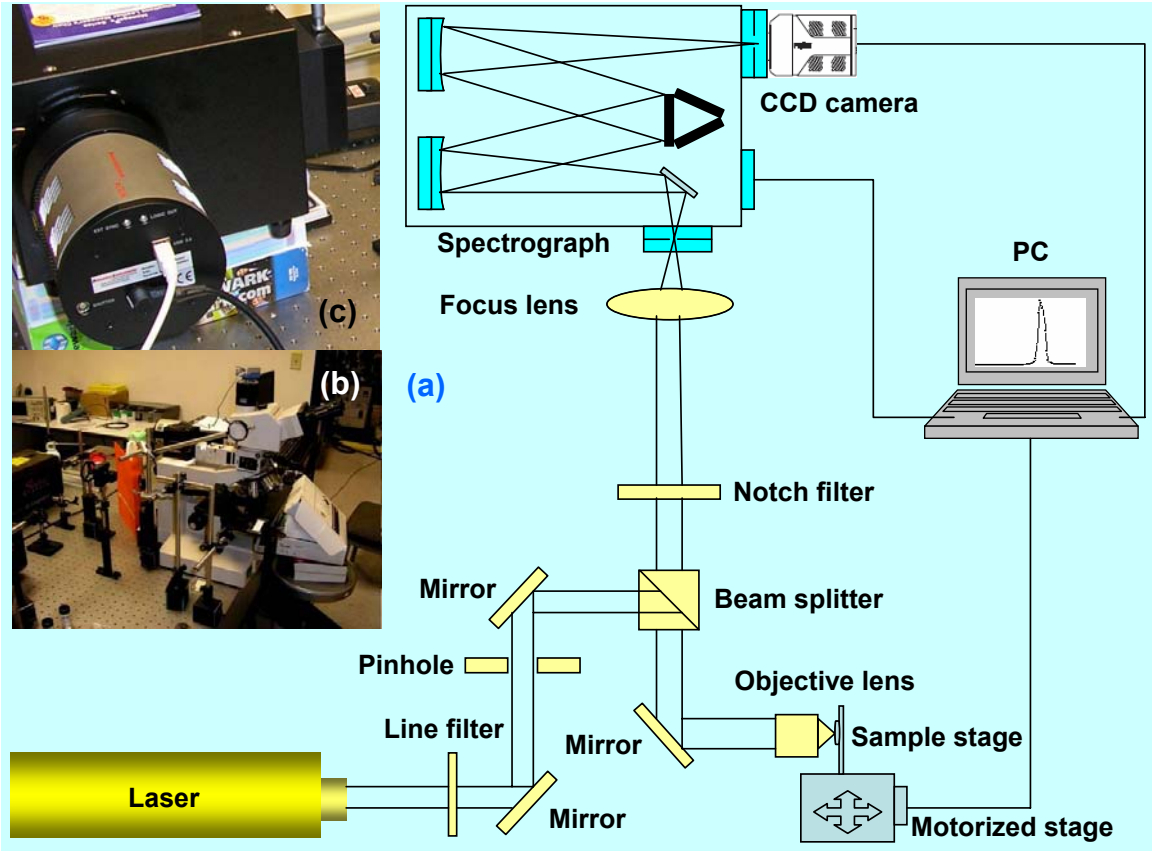

FIGURE 4.1 Schematic diagram of the micro-Raman spectrometer; (b) experimental setup of the micro-Raman spectrometer; (c) experimental setup of the spectrograph and the CCD camera.

The schematic diagram of a micro-Raman spectrometer with 180º back scattering configuration is shown in Fig. 4.1. The laser beam with 514.5 nm wavelength from the Argon laser passes through the line filter. The intensity of the laser plasma lines is much suppressed by the line filter while most of the laser line can pass. The beam splitter plays two roles: direct the laser light to the objective lens for excitation and deliver the

scattered signal back to the spectrometer for the detection. A 50X microscope objective lens (NA=0.55) with a long focal length (8 mm) is used to focus laser light reflected by the beam splitter to the sample surface. The scattered light is collected by the same objective lens. The holographic notch filter placed between the beam splitter and the focus lens attenuates the Raleigh scattering light which is much higher than the Raman signal. The collected scattered light is focused into the entrance slit of the spectrograph by the focus lens (triplet astigmatic lens), dispersed by gratings of the spectrograph and collected by the CCD camera. Raman images are obtained by translating the sample across the microscopic objective focus with the motorized stage and using the Raman peaks extracted from each spectrum as the fingerprints. The focusing can be roughly adjusted manually or fine-tuned automatically. The coordination among the spectrometer, the CCD camera and the *XYZ* stage is managed by the self-developed mapping program.

4.2.2 Optical components

The dielectric beam splitter (25 mm in diameter, Newport) has a reflection/transmission ratio of 30/70 for the incident unpolarized light with the wavelength of 514.5 nm. As the laser power is not critical, this ratio ensures that most of the scattered light can be delivered through the beam splitter with high efficiency.

The sharp transition from high diffraction efficiency to high transmission renders the holographic filter a nearly ideal Rayleigh rejection filter for the Raman measurement close to the Rayleigh line (100 cm^{-1}). A notch filter (Kaiser Optics, SuperNotch®) is used in our system. The choice of the objective lens depends on the type of samples to be examined. If the samples consist of particles in the sub-micro size range then a high magnification, high numerical aperture objective lens will be a good choice because the

lens with high NA can collect the scattered light in a large solid angle, and thus more Raman signals can be detected. Meanwhile, the laser spot size is inversely proportional to the NA of the objective lens. Three objective lenses have been evaluated in the experiment: a standard 50X objective lens (NA=0.8) from Olympus, a standard 20X objective lens (NA=0.4) from Olympus and a 50X objective lens with a focal length of 8 mm (NA=0.49) from Leica. Although the highest Raman intensity is obtained by the standard 50X objective, it is inadequate for large scale mapping, e.g., millimeter scale mapping, because the system will be out of focus and this generates spurious signals. The focus depth of this lens is short, so the focusing can be strongly affected by the surface roughness, the defects of sample and the tilt of stage. The focus depth can be defined approximately by:

$$L = {16\lambda f^2}/{\pi d^2}. \tag{4.1}$$

Here, λ is the wavelength of excitation laser, f is the focal length of the objective lens, and d is the diameter of the laser beam. The focus depth of the 50X lens with a 18-mm focal length and the standard 20X lens is much larger than the standard 50X lens, thus they are not easy to be out of focus.

4.2.3 Spectrometer

A triple-grating dispersive imaging spectrograph (Princeton Instrument, SP-2300i), which has a focal length of 300 mm and is equipped with a CCD camera (Princeton Instrument, PIXIS 400B), is a highly efficient spectrometer optimized for the wide spectral field Raman or fluorescence measurement in the range from 0 to 1400 nm.

It features an astigmatism corrected optical system with a direct digital grating scanning mechanism and full wavelength scanning capabilities. Three gratings are provided: 1) 300 g/mm with 300 nm blaze and 11 nm/mm wavelength dispersion covering 279 nm range optimized from 200 nm to 500 nm, 2) 600 g/mm with 500 nm blaze and 5 nm/mm wavelength dispersion covering 127 nm range optimized from 300 nm to 900 nm, and 3) 1200 g/mm with 750 nm blaze and 2.3 nm/mm wavelength dispersion covering 58 nm range optimized from 800 nm to 2000 nm. Gratings can be selected to optimize the instrument to a specific application and a wavelength range. The dispersion and the spectral resolution are increased by increasing the grating density. The 600 g/mm grating is frequently used in the experiments due to its high optical throughput (~80%) at the wavelength of 514.5 nm. The spectrograph is optimized for a flat field and low level optical aberration and provides the 3200 cm^{-1} spectral field on the detector with a spectral resolution of 3 cm^{-1} at 514.5 nm. The positioning of the spectrograph is provided by the stepping motors through the linear encoders that give the repeatability of 0.05 cm^{-1}. The wavelength calibration can be performed with a neon and argon lamp or with the plasma lines of the laser sources.

The CCD camera is a fully integrated system with permanent vacuum/deep cooling and a high-performance, back-illuminated, spectroscopic-format CCD. It can be thermoelectrically cooled (air) down to -75 °C to provide the lowest dark charge. The imaging chip of the camera has a matrix of pixels of 1340×400, with the height of 8 mm and the width of 27 mm. Its spectral coverage is broad enough for multi-stripe spectroscopy. Another exclusive feature is the integration of the two software-selectable amplifiers to achieve the highest sensitivity for low signal levels and the highest dynamic

range with higher signal levels. The most prominent feature is that its quantum efficiency is as high as 90% in the wavelength ranging from 500 nm to 650 nm, which guarantees the sufficient sensitivity.

4.2.4 Scanning stage

The point to point scanning method is employed to perform the Raman imaging. The sample is scanned under the microscope objective lens in the *XYZ* plane using a commercial *XYZ* motorized stepper stage (ALIO Industries) equipped with position sensors and a closed-loop position feedback (Delta Tau). The sample can be moved in the range of 18 mm along each axis with adjustable steps. The travel resolution is 3.175 μm per step. A home-made Al plate is fixed on the *Z* axis serving as a sample holder. The sample can be focused with both the manual and the motorized mode after assembling the motorized *XYZ* stage with a precise vertical translation stage (Edmund Optics). The scanning process thus produces simultaneously a topographical image of the sample and the spectroscopic image.

4.2.5 Mapping program

The mapping software was developed using Labview^{TM} as the programming platform. The main operations and functions include the adjustment of focusing conditions, the data representation, the control of the scanning speeds, the control of the *XY* scanning area and the control of the spectra readout. The driver interfaces for controlling the *XYZ* motorized stage and the spectrometer are provided by the suppliers. Both individual spectra and spectral images can be analyzed either by the program or the available data analysis software. Represented by the 2D projection or the pseudo-3D

visualization, a spectral image is a multidimensional data set with two spatial dimensions and one wavenumber dimension. The fingerprints to perform imaging include the integral intensity in an interested range, the average value of several points near the interested peak, and the Raman peak. The interested peak is determined either by a priori known information or by the recorded spectrum.

4.2.6 Optical alignment

To have an optimal alignment, the laser beam should be perpendicularly focused onto the sample surface, and the scattered light should be horizontally delivered into the entrance slit of the spectrometer because the slit of the spectrograph is vertical.

The CCD camera should be well positioned to the output window of spectrometer. Using the software WinSpec32 coming with the spectrometer from Princeton Instruments, the detector can be precisely installed to the spectrograph. Using the image mode, the CCD camera can be adjusted to the right position by obtaining the narrowest image. Using the spectroscopy mode, the CCD camera can be fine-tuned to get the minimum spectral width at 0 nm, which is about 3 nm.

4.3 Development of a tip-enhanced Raman spectrometer

4.3.1 System description

The schematic diagram of the developed TERS system is depicted in Fig. 4.2. The system consists of an optical path, a spectral acquisition module (a spectrograph and a CCD camera), an STM module, a motorized stage module, an optical microscope, and a computer. The optical path is used to deliver the excitation laser beam onto the sample surfaces and collect the Raman signals from the surfaces. The spectral acquisition module

is used to collect the scattered signals and convert the optical signals into electronic data. The tip-surface distance is controlled by the STM. The motorized stage module is used to position the samples. The optical microscope equipped with another CCD camera plays the roles of locating the regions of interest and monitoring the optical alignment. The computer is used to control the STM and acquire, process, and visualize the Raman signals.

The instrument can accommodate both the AFM and the STM functionalities to combine with the Raman spectrometer. An SPM system (Agilent, SPM 5500) is used as a platform to build the TERS system. The tip is mounted on a piezoelectric transducer that has a stroke of 100 μm and a closed-loop control. In addition, a two-axis nanopositioner (Mad City Labs, nano-H100) is placed beneath the sample holder, which is used for mapping the sample surfaces. The software used for the mapping is developed using the LabView^{TM} programming platform together with the instrumental drivers provided by the hardware suppliers.

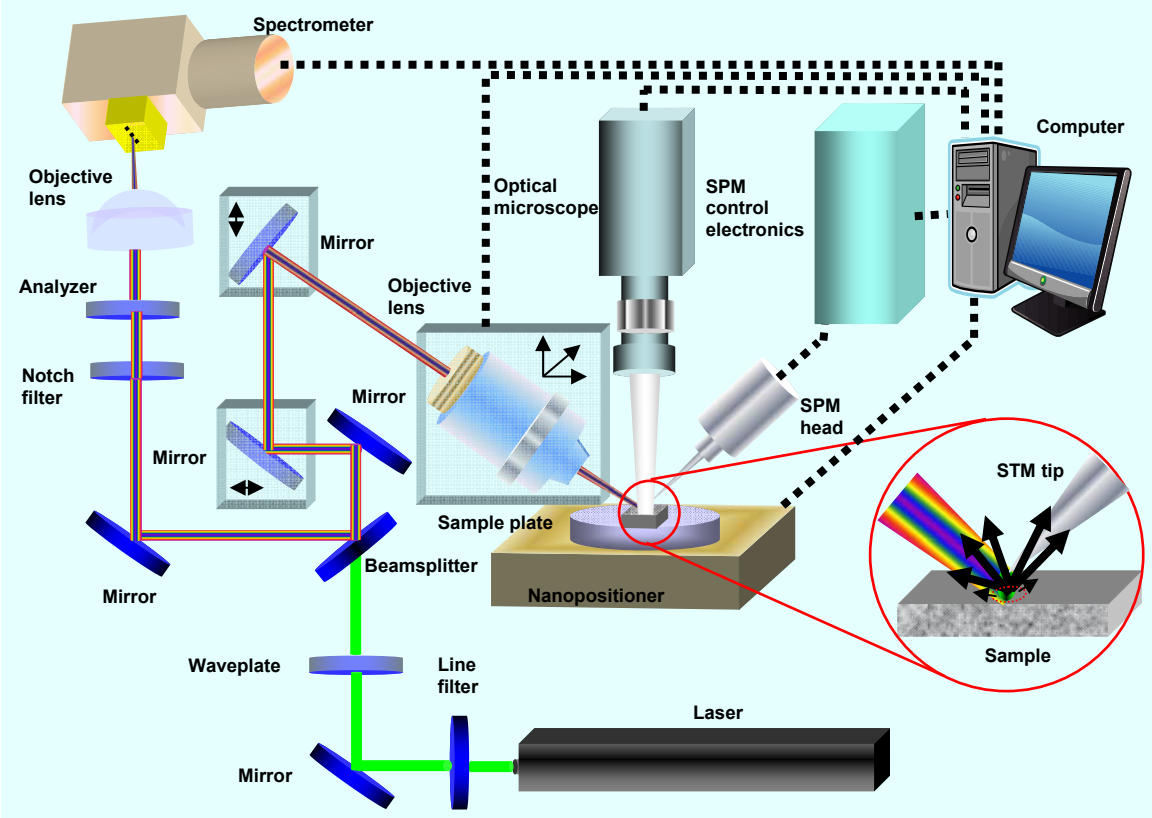

FIGURE 4.2 Schematic diagram of the TERS system.

In Fig. 4.2, the laser beam from the Argon laser (Coherent, Innova 300) passes through the line filter (Newport) that only allows the wavelength of 514.5 nm to pass through. The half-wave plate (CVI) is used to control the polarization of the beam. The beam is split into two beams by the beam splitter. The transmitted beam is focused on the sample surface by the objective lens (Olympus, LWD 50X, NA = 0.45, WD = 15 mm), and the reflected beam has to be wasted because the same splitter will be used to reflect the collected signal to the spectrometer. The STM tip approaches the sample surface with the tip-surface distance in the tunneling range of 1 nm. The status of the tip, the laser beam, and the substrate surface are monitored by the optical microscope. The position of the objective lens is controlled by the motorized *XYZ* stage (shown as the box outside the objective) with a resolution of 3 μm. After a successful optical alignment, the scattered

Raman signals are collected by the objective lens. After passing through the notch filter (Kaiser, SuperNotch®, OD = 4.0) and the analyzer (Newport), the beam with Raman signals is focused by the lens (CVI) into the slit of the spectrograph (Acton Research, Spectro-2300i). A back-illuminated CCD camera (Princeton Instruments, PIXIS-400B) with a high quantum efficiency (> 90% at 514.5 nm) is used to acquire the Raman spectra. The spectra are then analyzed, processed, and visualized by the computer.

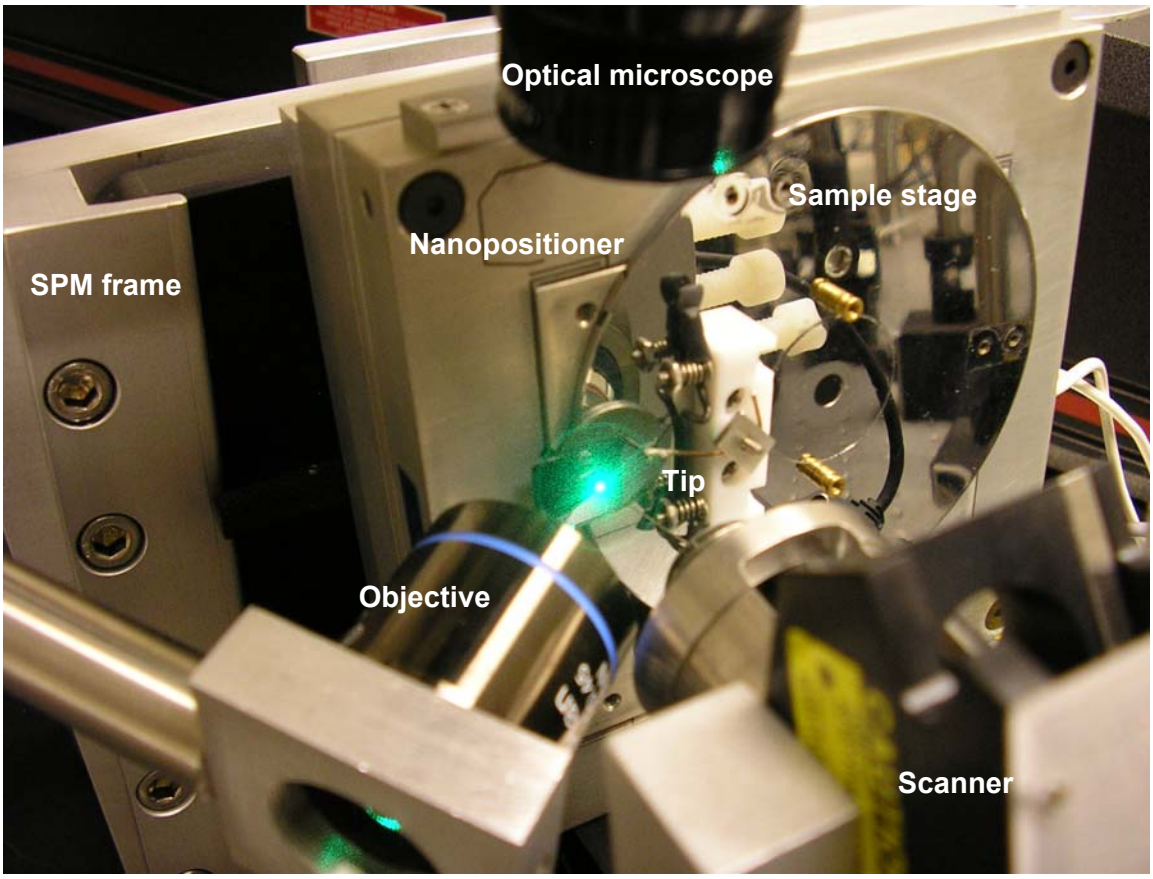

FIGURE 4.3 Experimental setup of the TERS system.

To perform Raman mapping, a sample is placed on the nanopositioner which has a lateral resolution of 0.2 nm and can be controlled by the developed mapping software.

Figure 4.3 shows a picture for the practical experimental setup. It can be seen that both the STM system and the motorized sample module are placed on a fixture frame.

4.3.2 SPM electronics

An SPM from Agilent Technologies was selected for building the TERS system due to its open architecture. This SPM has a sufficient space to incorporate other modules. The SPM system can accommodate different operation modes including the contact AFM, the non-contact AFM, the current sensing AFM (CSAFM), the STM, and the scanning tunneling spectroscopy (STS). The SPM system is composed of an optical microscope, a motor, a 4-segement PIN laser diode, an environment chamber, a main frame, and three scanners including one STM-only scanner with a 1-μm scanning range (9501A), one STM-AFM scanner with a 10-μm scanning range (9520A) and one STM-AFM scanner with a 100-μm scanning range (9524A).

4.3.3 Nanopositioner

The nanopositioner was selected based on four requirements: the travel range, the resolution, the control method (close-loop or open-loop), and the price. In addition, it is also important that the positioner has enough space to hold the STM sample stage. The module Nano-100H from Mad City Labs meets all the needs. It is a compact 2-axis positioning stage which provides excellent positioning performance at a low price. Internal position sensors provide an absolute, repeatable position measurement with a picometer accuracy when operated with the Nano-Drive™ controller. This module, with a resolution of 0.2 nm and a travel range of 100 μm, is controlled by a controller with a close-loop approach. The free space on it with an area of 100×100 mm^2 permits the

sample stage to be fully and firmly fixed on. The Labview™ drivers allow us to seamlessly incorporate this module into the Raman mapping program.

4.3.4 Tips

Tips are crucial for the TERS and the surface nanostructuring using an STM since the resolution, the sensitivity, and the image quality are unexceptionally determined by the tip properties, of which the two most important are the materials and the shapes of the tips. The selection of materials is based on two factors: the Plasmon resonance and the lightning-rod effect. For the past two decades, different metal tips, including Ag, Au, Pt, W, Ir and Al, have been investigated theoretically and experimentally by various researchers to find the materials with the largest resonance enhancement factor based on Plasmon resonance. The conclusion is that Ag and Au are the best candidates. Although the tips made of Ag have better optical properties in the visible, leading to higher enhancement and sharper resonance, they are chemically unstable when exposed in open air. On the contrary, the Au tips are very stable and easy to make. From the perspectives of lightning-rod effect, both Ag and Au tips are good candidates because in the visible region, their absorption losses are relatively low. The tip shapes are another factor that affects the field enhancement. The amplitudes and the widths of the Plasmon resonances for a given frequency and a given material depend on the shape of the nanostructure. Numerical simulations show that the tip apex with a prolate spheroid shape exhibits a much higher enhancement than the tip apex with a sphere shape. In the experiment, these two kinds of tip, i.e., Au tips and Ag-coated W tips fabricated using direct current electrochemical etching method, were used.

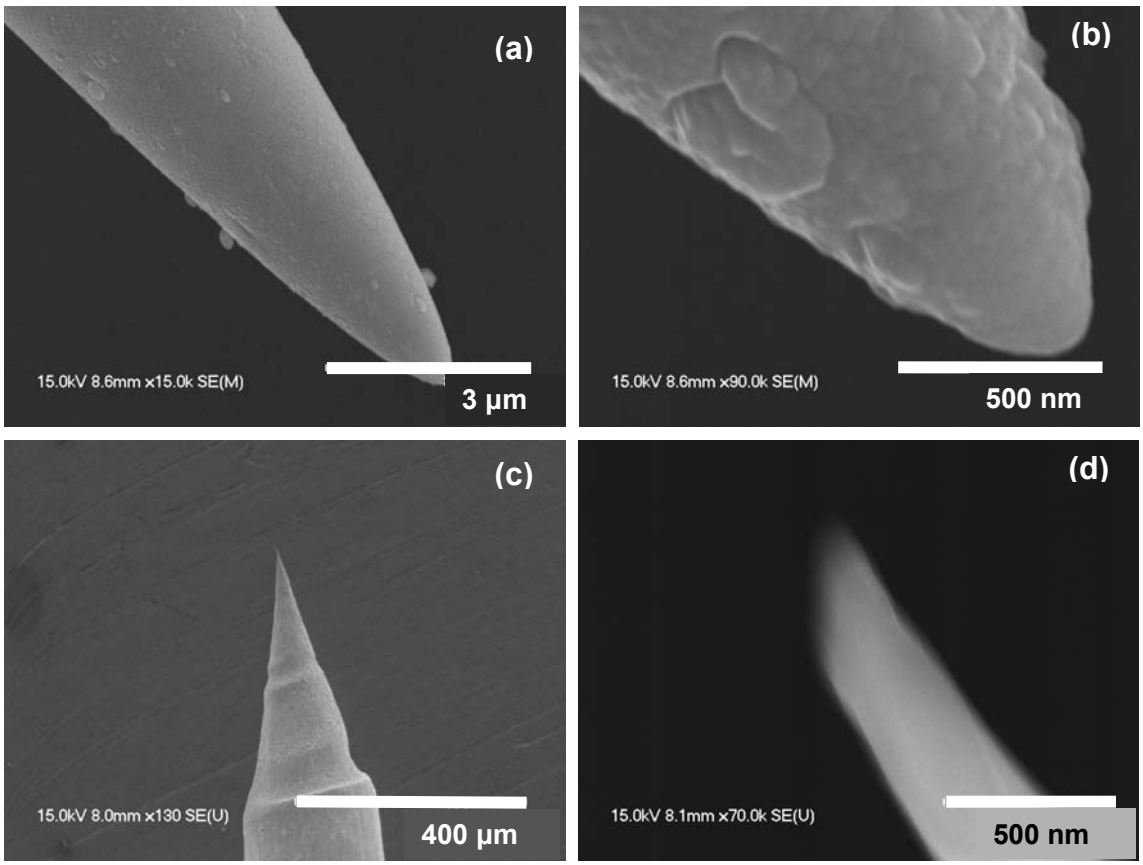

FIGURE 4.4 SEM micrographs of (a) the normal view, (b) the zoomed view of a Ag-coated W tip, (c) the normal view and (d) the zoomed view of a Au tip.

4.3.5 Optical alignment

To obtain the best enhancement, the precise alignment of the focused laser beam with respect to the tip is essential. The beam center should be aligned in between the tip-surface gap, in which the alignment of the microscale laser beam with the nanoscale tip apex is challenging. Three steps of alignments, which are the coarse, the intermediate, and the precise alignments, are used to address this challenge. More specifically, the laser beam is aligned to the tip with a millimeter range accuracy in the coarse alignment, a micron range accuracy in the intermediate alignment, and a nanometer range accuracy in the precise alignment.

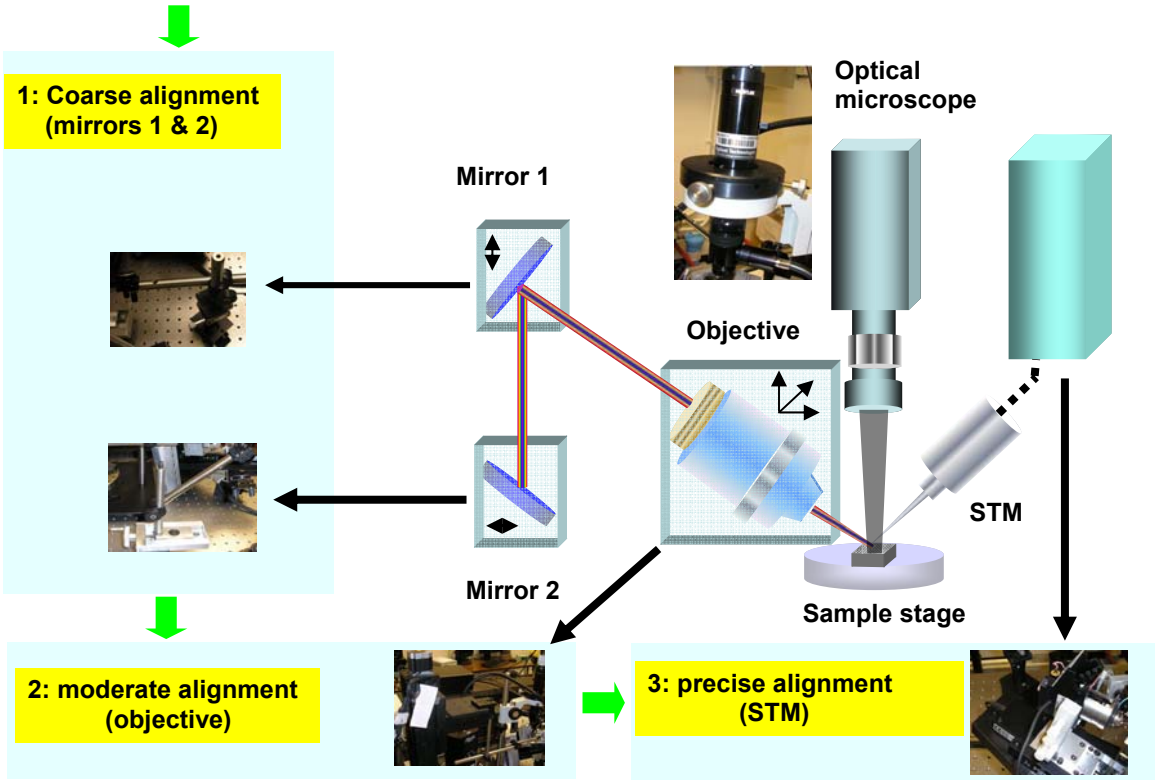

FIGURE 4.5 Representation of the optical alignment procedure for the TERS system.

As shown in Fig. 4.5, two mirrors (in boxes), one objective lens (in a box) and one tip, which are all movable, are the key components to perform the optical alignment. Both the mirrors are mounted on two orthogonally-arranged translation stages to perform the coarse alignment. The objective lens is mounted on the motorized *XYZ* stage for the intermediate alignment. The precise alignment is implemented by the piezoelectric transducer mounted on the STM scanner. The tip position and the sample surface are monitored by the optical microscope. Before the coarse alignment, the objective lens needs to be moved away from the optical path. The laser beam is positioned in the targeted region completely covering the tip apex. The objective lens then moves back and gradually approaches the sample surface. When the optical path is well aligned, the

focused laser beam is always along the propagation direction. At this stage, the position of the focused beam should be near the tip position. Subsequently, by moving the objective lens in the intermediate alignment, the focused beam is brought to the tip position with an accuracy of 50 μm. Finally, the tip is brought back and moves in a range of 100 μm with a resolution of 0.4 nm. Since the beam is within a range of 50 μm from the tip position, the laser beam eventually meets with the tip at a certain position.

Figures 4.6(a), 4.6(b) and 4.7(c) are the images of the Ag-coated W tip and the laser beam under different conditions monitored by the optical microscope. Figure 4.6(a) shows that the tip was away from the substrate, in which only far-field Raman signals can be obtained. A mirrored image of the tip can be observed due to the reflection of the substrate surface. Figure 4.6(b) shows the scattered light at the tip apex when the laser beam was focused on the tip. A mirrored diffraction image is present, indicating that the laser beam was not exactly positioned in the tip-surface gap but slightly on the tip side. The focused laser beam is thus partially blocked by the tip, so that the total Raman intensity is reduced. Figure 4.6(c) shows the diffraction pattern in an ideal alignment where the enhanced Raman intensity can be observed. The strong interference patterns around the tip apex are generally used to identify the optimal alignment between the tip and the sample surface. Likewise, Fig. 4.6(d) shows the diffraction pattern for a Au tip in a good optical alignment.

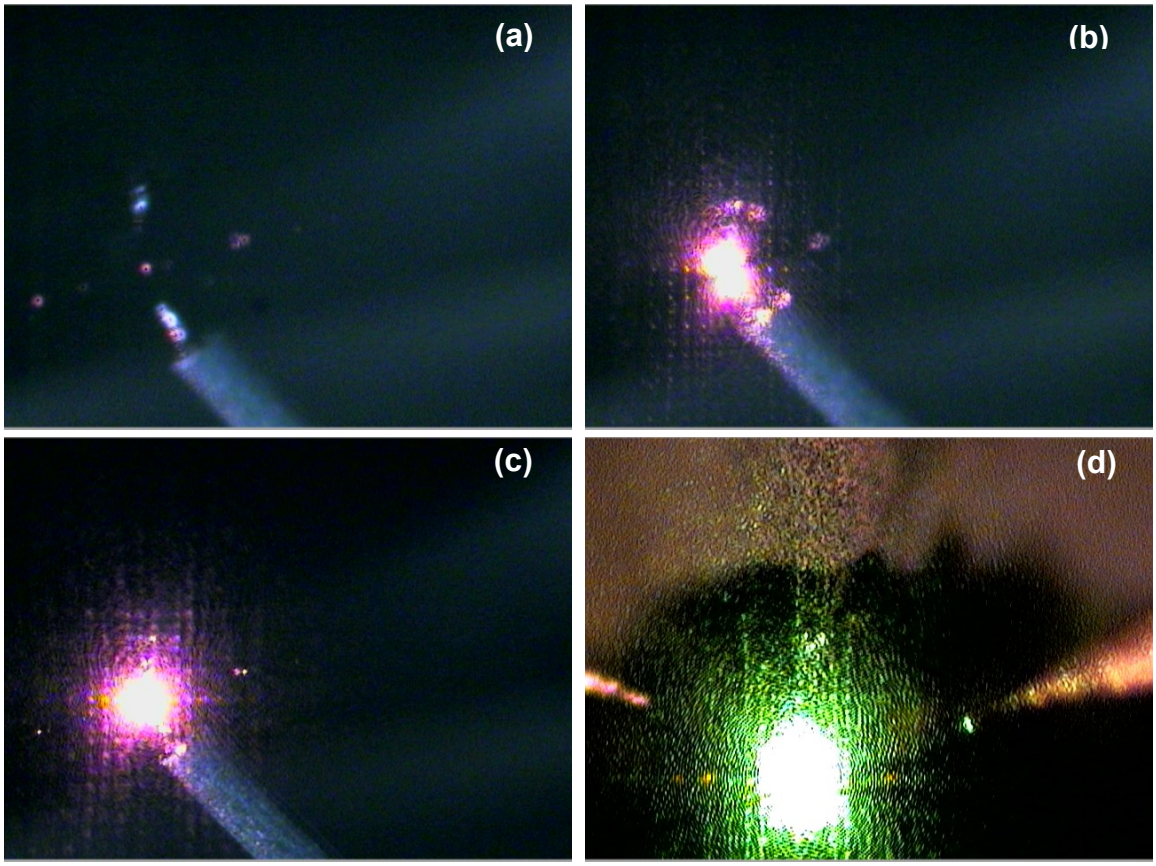

FIGURE 4.6 Images captured in the optical alignment under the conditions of (a) the beam away from the tip, (b) the beam on the tip, and (c, d) the tip in the center of the tip-surface gap (good alignment). (a, b, c) are for a Ag-coated W tip and (d) is for a Au tip.

4.3.6 Dependence on the tip-surface distance

Tip-surface distance also has a significant impact on the enhancement, because the optical field underneath the tip apex is strongly dependent on that distance [20]. The optical field decays rapidly with the distance away from the tip, so the sample should be placed very close to the tip in order to take advantage of the enhanced field. The fact that the measured signals in the RS is approximately proportional to the fourth power of the electric field indicates the Raman scattering enhancement decays even faster with the increase of the tip-surface distance. Figure 4.7 shows the near-field Raman intensity, i.e., the net enhanced Raman intensity, as a function of the tip-surface distance. The data were

collected by moving the tip away from the surface in a closed-loop control along the normal direction. The intensity exponentially decays with increasing the tip-surface distance. When the distance is larger than 20 nm, the enhancement becomes very weak, even no longer perceivable, which is different from the result of other groups that the maximum range to obtain discernable Raman enhancement is 20 nm for a Au tip in air [21].

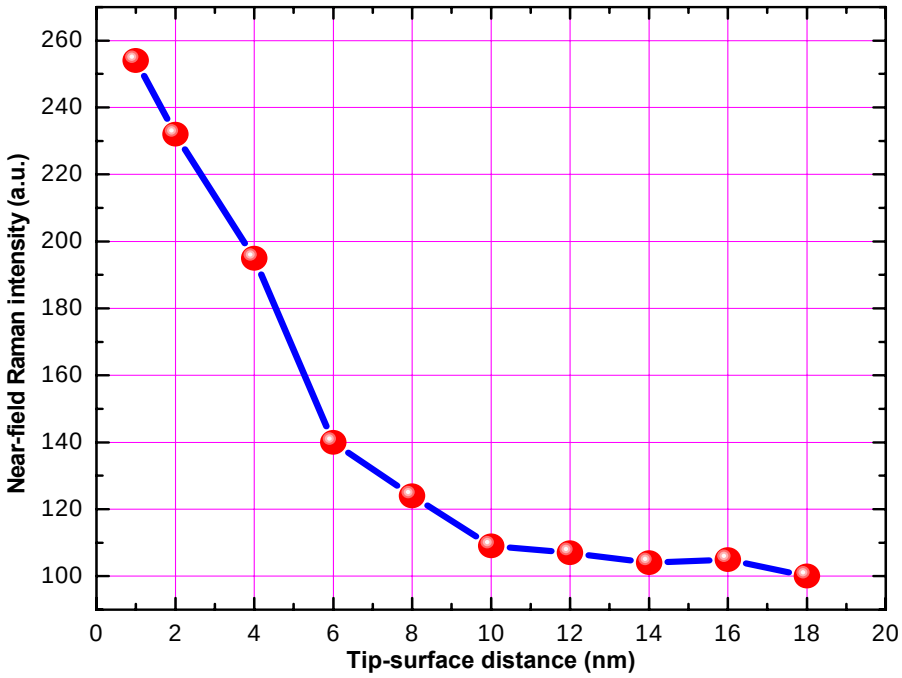

FIGURE 4.7 Near-field Raman intensity as a function of the tip-surface distance.

4.4 Performance of the developed Raman spectrometer

4.4.1 Raman spectra and imaging of diamond-like carbon films

The materials based on carbon elements have been applied to different areas due to their instinct properties determined by the carbon-carbon bonding that can form different molecular and crystalline structures. For example, the diamond with a cubic

structure by strong covalent sp^3 bonds can be doped to fabricate the substrates for integrated circuits, which will have properties superior to Si wafers due to their high thermal conductivity. Diamond Like Carbon (DLC) film is nowadays widely used to overcoat the surface of magnetic discs to prevent them from being scratched by the drive sliders because of its unique properties, such as high hardness, low friction, high chemical inertness, good optical transparency, and negative electron affinity [9].

RS is one of the most powerful tools for characterizing carbon materials, because the spectral shape exhibits wide varieties corresponding to the different forms of the carbon, and thus reveals fine structural information [22]. A typical DLC film shows a Raman band in the range between 1000 and 1800 cm^{-1}. It can be fitted by two Gaussian curves on a linear background. It consists a mixture of the sp^2, sp^3 and sp^1 bonding structures.

The DLC films were deposited by Pulsed Laser Deposition (PLD) using a pulsed Nd-YAG laser with a pulse width of 7 ns. The focused laser beam was incident at an angle of 45° on a pyrolitic graphite target (~99.999% purity) located 3 cm away from the substrate. The target had a rotational and translational motion to ensure a uniform erosion pattern over the target surface. The laser intensity was fixed at 700 mJ and the frequency was 10 Hz. The DLC films with a thickness of 2 μm were fabricated. The film was then post-treated with a KrF excimer laser to increase the surface roughness.

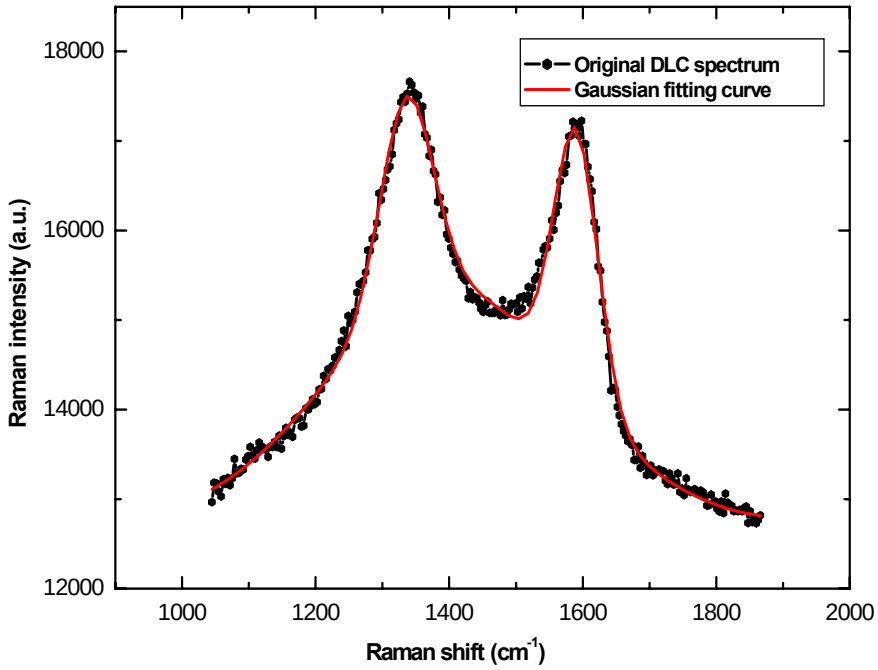

FIGURE 4.8 Raman spectrum of the DLC film fabricated by pulsed laser deposition.

Figures 4.8 and 4.9(a) show the Raman spectrum and the SEM micrograph of the DLC film, respectively. The peaks at around 1330 cm^{-1} and 1337 cm^{-1} (D-band) indicate that the film has an sp^2 bonded carbon structure. The fact that the film has an sp^3 bonding can be concluded from the peak at 1589 cm^{-1} (G band). The ratio between D band and G band, defined as *R*, is generally used to estimate in-plane crystalline size with the formula $L_a = 44/R$ for the extended range 2.5 nm < L_a< 300 nm. The DLC crystalline size is calculated to be around 4 nm. The Raman image in the region 100×100 μm^2 with 3.2 μm step resolution is shown in Fig. 4.9(b).

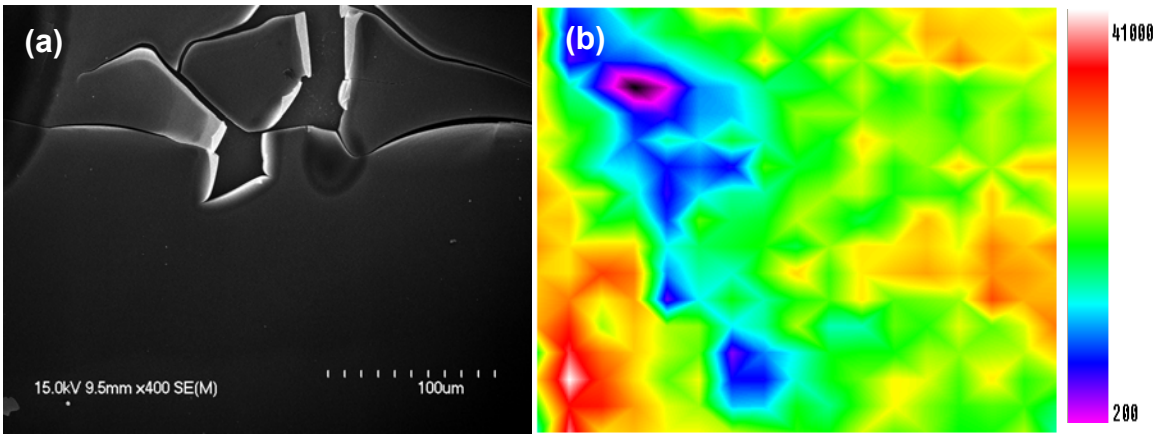

FIGURE 4.9 (a) SEM micrograph and (b) Raman image of the DLC film.

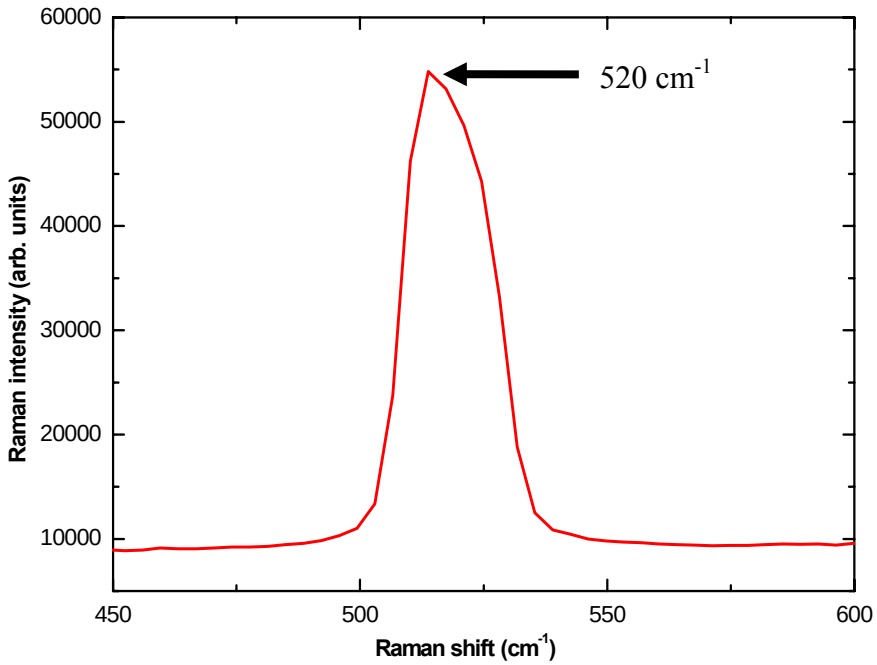

FIGURE 4.10 Raman spectrum of the Si substrate.

4.4.2 Raman spectra and imaging of Si substrates

A patterned metal film (Fe/Ni) with the smallest feature size of 6 μm, which includes some large and small strips, was fabricated on a Si substrate to evaluate the mapping function of the developed Raman spectrometer by using the Si spectra as the fingerprints

[23]. Figure 4.10 shows a typical Raman spectrum of the crystalline Si substrate with a sharp peak at 520 cm^{-1}. Figure 4.11 shows the 1D profile of the Raman fingerprint across the four large Si strips. SEM micrographs for the large and small strips on the substrate are shown in Fig. 4.12(a) and 4.12 (c), respectively.

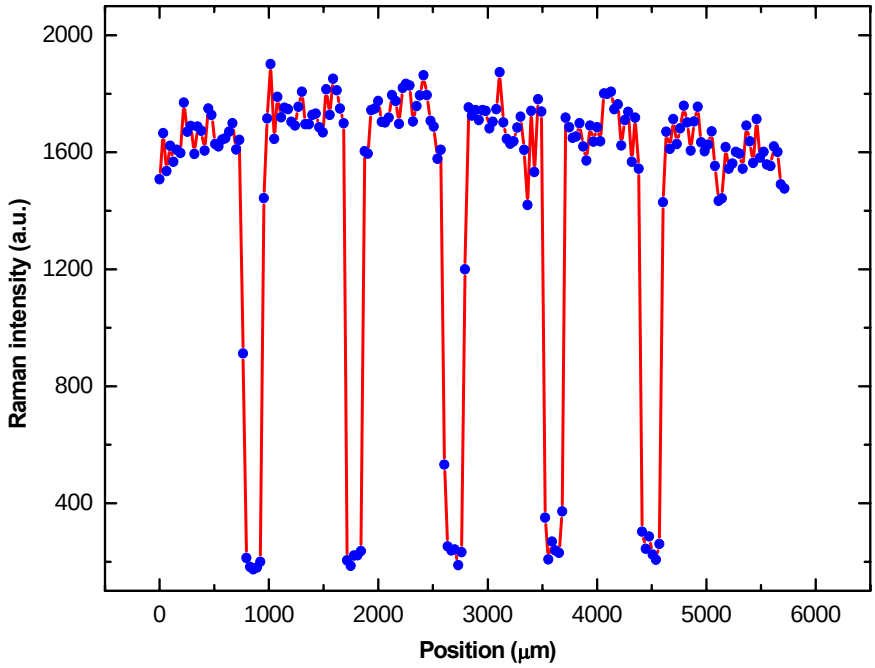

FIGURE 4.11 1D Profile of the patterned Si substrate with 1D scanning.

Some random deviations of Raman intensity in the entire region are found. The 2D Raman mapping for a large zone scanning (4.8×3.2 mm^2) with a step size of 32 μm is shown in Fig. 4.12 (b). Raman mapping for a small zone scanning (100×100 μm) with a step size of 3.2 μm is shown in Fig. 4.12(d). The clearly mapped images in the large and small regions demonstrate that the system is stable and valid for Raman mapping.

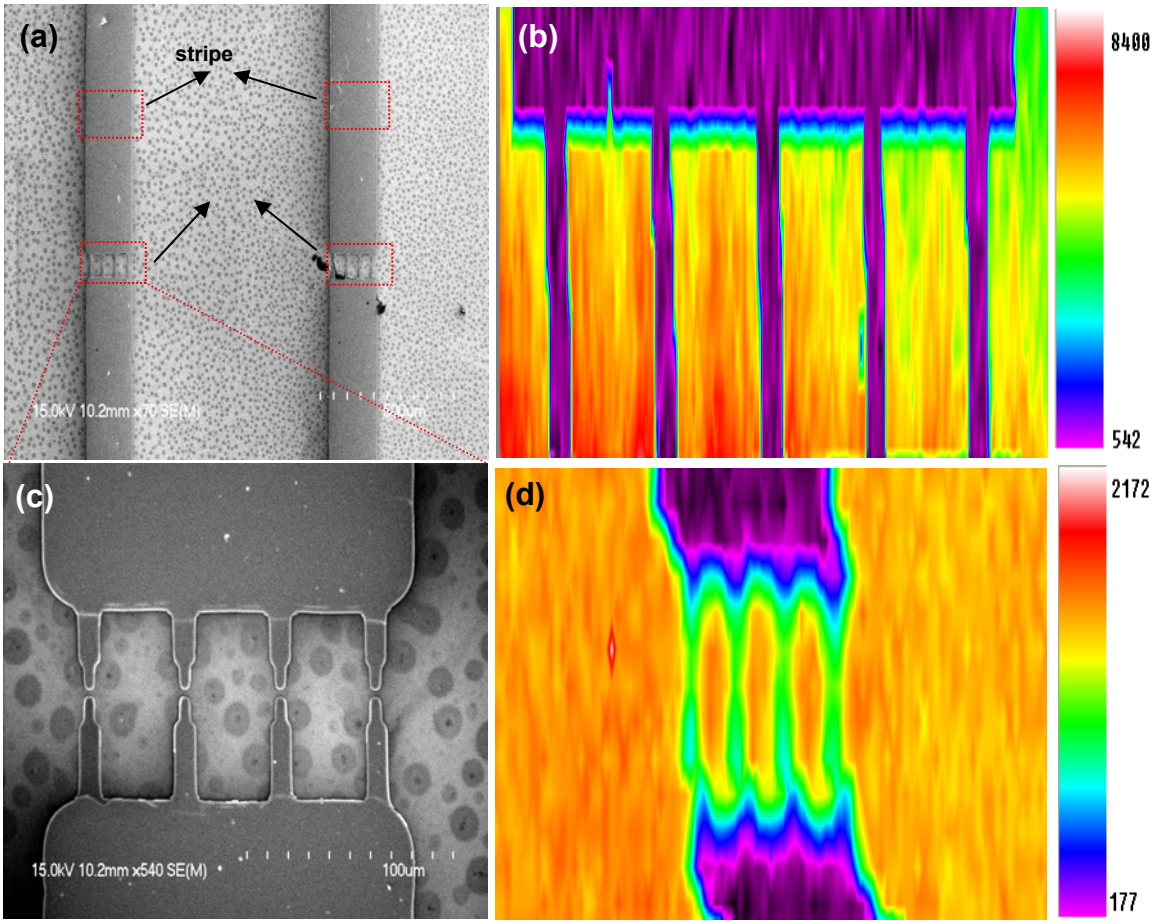

FIGURE 4.12 SEM micrographs and Raman images of patterned Si. (a) SEM micrograph of the large strip; (b) 2D Raman image of the large strip; (c) SEM micrograph of the small strip (e) 2D Raman image of small strip.

4.4.3 Raman spectra of Si substrates

Contrast ratio, defined as the ratio of the near-field to the far-field Raman intensity, is used to evaluate the extent of the enhancement. The far-field Raman intensity is obtained when the laser beam is far away from the tip, ensuring no tip-beam interaction exists. Subtracting the far-field Raman intensity from the total Raman intensity obtained from a tip-enhanced Raman measurement equals to the near-field intensity when the laser beam is well aligned with the tip to achieve strong near-field effects. It is reported that the

contrast ratio of the crystalline Si at 520 cm^{-1} is around 50% by Ag-coated W tips or Au tips.

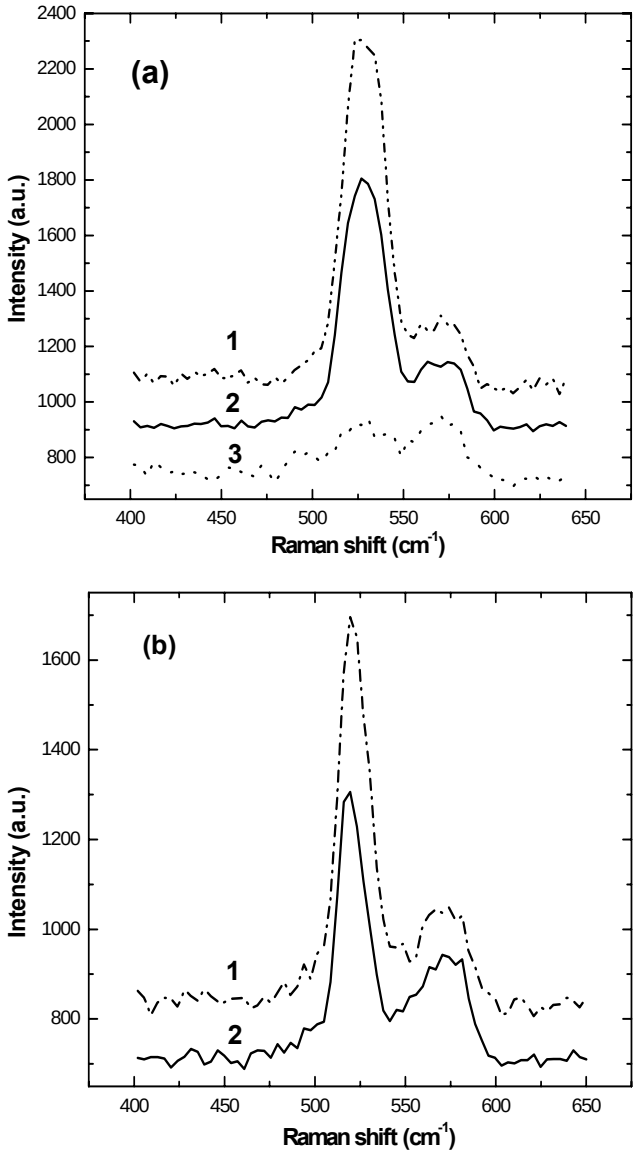

FIGURE 4.13 Raman spectra of the Si substrate using (a) a Ag-coated W tip and (b) a Au tip. Spectra 1, 2, and 3 were taken in the cases of good alignment, laser beam away from the tip, and laser beam on the tip but not in the gap, respectively.

Figure 4.13(a) shows the Raman spectra of the Si substrate with the Ag-coated W tip under different conditions. The total intensity in a well aligned case, the far-field intensity, and the total intensity in a misaligned case in which the laser beam was partially blocked are indicated by Raman spectra 1, 2 and 3 in Fig. 4.13(a), respectively. In a well aligned case, a contrast ratio of 52% can be observed (spectrum 1). When the beam was blocked by the tip, the intensity was significantly reduced (spectrum 3). Figure 4.13(b) shows the Raman spectra of the Si substrate with a Au tip. A contrast ratio of 47% was obtained.

4.5 Far-field suppression by depolarization

To further improve the contrast ratio, several methods have been employed including the modification of the tip material and geometry [24], the selection of the excitation wavelength or the tuning of the plasma resonance [25], and the use of the excitation and scattering light polarization [26]. The common rationale of these approaches is to increase the near-field Raman intensity. Nevertheless, there is an alternative way to increase the contrast ratio by suppressing the far-field Raman intensity. Raman scattering signals are generated from the interaction between a polarized incident laser beam and molecular vibrations. With different symmetry of the vibration mode, the scattered signal can be polarized either parallel or perpendicular to the polarization direction of the incident beam or both. For symmetric vibrations, the scattered light is almost completely polarized in the same direction as the incident field, and no depolarization can be observed. Whereas, the scattered light from asymmetric vibrations is polarized both parallelly and perpendicularly to the incident beam. Since crystalline Si has a highly asymmetric structure, the Raman scattering is strongly polarized. For example, the

polarization of the incident beam can be locally changed around the vicinity of diamond nanoparticles [27]. The sharp apexes of Ag tips should be able to play the same role as that of the diamond particles. If an analyzer were oriented perpendicular to a polarizer, the far-field signals could be blocked by the analyzer. The tip interaction changes the polarization, leading to the depolarization. Recently, using depolarization technique to efficiently suppress the far-field signals has been reported.[15] This depolarization technique was further optimized to successfully obtain Raman images with high contrast [28].

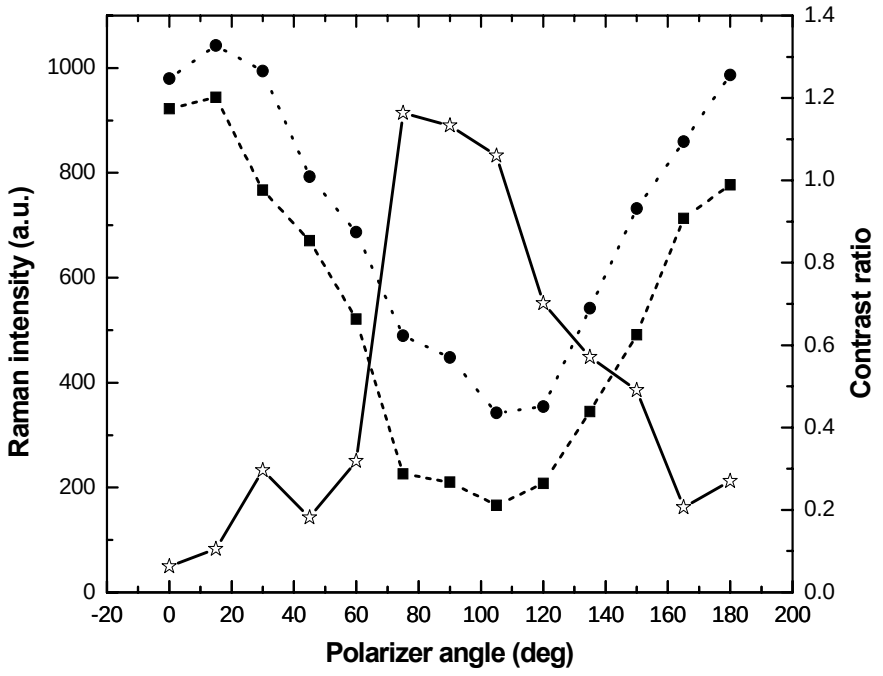

FIGURE 4.14 Far-field Raman intensity (squares), total Raman intensity (diamonds), and contrast ratio (stars) as functions of the polarizer angle.

In the experiments, the orientation of the analyzer was kept vertical to the the optical table surface to which the tip axis was almost parallel. The polarization direction

of the laser beam from the laser was vertical to the table surface. This polarization was varied by the half-wave plate. The initial angle of the plate with respect to the polarization of the input laser beam was 0°. Then the plate was rotated from 0° to 90° with a step of 7.5° so that the polarization direction of the output laser beam was varied from 0° to 180° with a step of 15°. Shown in Fig. 4.14 are the far-field Raman intensity, total Raman intensity, and contrast ratio as functions of the angle of the beam polarization, which is defined as the polarization direction of the incident beam with respect to the sample surface. The far -field Raman signals were collected when the tip was far away from the beam. The total Raman signals were collected when the tip was well aligned with the beam.

By changing the angle of the half-wave plate, different Raman intensities at the peak position of 520 cm^{-1} were captured, and thus different contrast ratios were obtained. It can be clearly seen that a high contrast ratio of 120% has been achieved when the polarizer angle is between 90° and 105° using the Ag-coated W tip. The Raman spectra of the Si substrate from the Ag-coated W tip are shown in Fig. 4.15(a) when the depolarization technique was employed. This enhancement is more than doubled with the depolarization. The Raman spectra of the Si substrate from a Au tip are shown in Fig. 4.15(b), with a high contrast ratio of 175% being obtained. The results demonstrate that the depolarization technique is highly efficient to improve the contrast ratio.

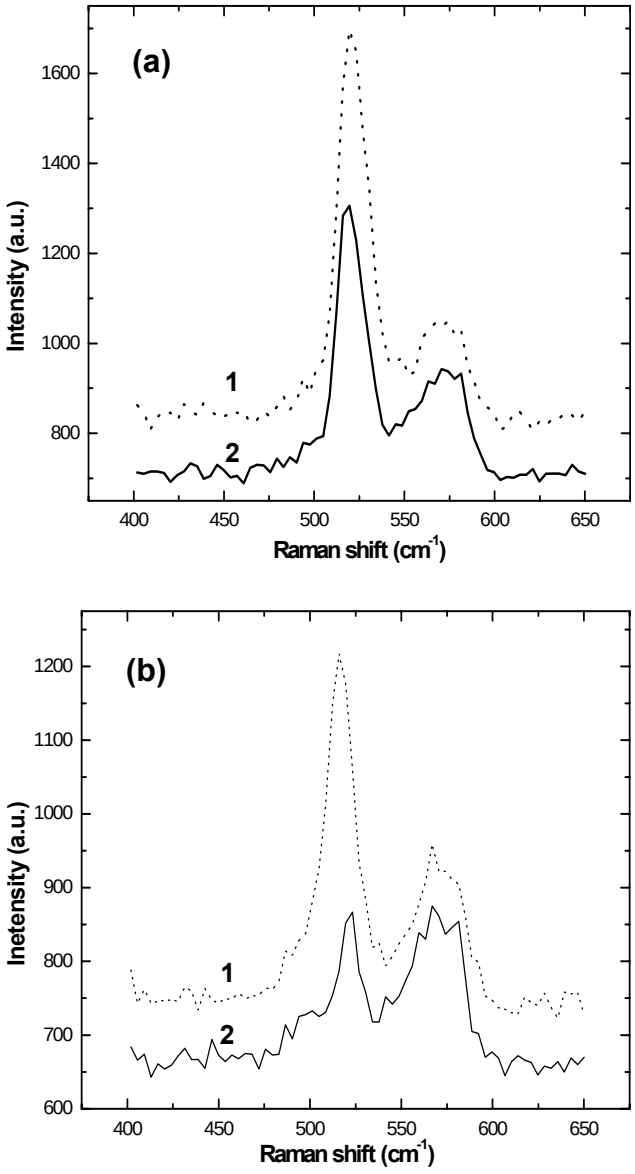

FIGURE 4.15 Raman spectra of the Si substrate using (a) the Ag-coated W tip and (b) the Au tip with depolarization. Spectra were taken in cases of good alignment and beam away from the tip, respectively.

4.6 Conclusion

Equipped with a highly sensitive back-illuminated CCD camera and a notch filter, the micro-Raman system allows us to characterize the chemical structures of materials such as SWCNTs. Raman mapping capability was demonstrated by imaging the patterned Si. The spectra and Raman images of the DLC film fabricated with the PLD process was studied. We also developed a TERS system, which consists of a Raman spectrometer and a scanning tunneling microscope, to improve the spatial resolution and detection sensitivity concurrently, for which we fabricated and tested Ag-coated W tips and Au tips. In order to improve the contrast ratio of the TERS system, we adopted a depolarization technique to efficiently suppress the far-field signals. The developed TERS system features fast and reliable optical alignment, versatile sample adaptability, and sufficient far-field signal suppression. The correlated characterization capability of the system provides a new approach to understand the relationship among the morphology, electronic, thermal, chemical, mechanical and optical properties of nanoscale materials and devices, while eliminating sample contaminations during the transportation among different instruments.

CHAPTER 5 ENHANCED RAMAN SCATTERING BY SELF-ASSEMBLED SILICA SPHERICAL MICROPARTICLES

5.1 Introduction

In order to render RS applicable to nanoscience and nanotechnology, both the sensitivity and the resolution need to be highly improved. Till present, researchers have developed several techniques to achieve the enhancement of Raman scattering, represented by interference-enhanced Raman scattering (IERS)[1], total internal reflection RS (TIRRS) [2], resonance Raman scattering (RRS) [3], near-field Raman microscopy (NORM, only refer to aperture type) [4], surface-enhanced Raman scattering (SERS) [5, 6] and tip-enhanced RS (TERS, only refer to apertureless type) [7-10]. Each of these methods has advantages over the others, but also has disadvantages. Taking SERS as an example, the most prominent advantage of SERS is that a very strong Raman enhancement can be achieved by using metal particles, e.g. Ag and Au, or substrates with roughness as sample carriers. The disadvantage is that those SERS-active substrates are irreproducible and unpredictable. But the common disadvantage of those proposed approaches is the complexity.

In order to overcome this disadvantage, we propose a simple and reliable approach to realize the Raman scattering enhancement in the order of 10^4. This technique is based on the nanojet phenomena, in which the light incident onto micro/nanoparticles can be redistributed and concentrated to generate nanojets on the other side of the particles in the propagation direction [11, 12]. Comparing with the incident light, the nanojets have higher intensity and much smaller waists, as shown in Fig. 3.2. This phenomenon has been experimentally verified using the fluorescence from iodine vapor to image the near-field intensity distribution and the fluorescence from ethanol droplets impregnated with rhodamine 590 to image the internal distribution [13]. The application

of this technique to enhance Raman scattering has also been proposed [11]. However, no experimental demonstration can be found so far. In the following, we show that the Raman scattering can be enhance to the order to 10^4 by using the nanojets generated by illuminated silica microparticles. The advantages of microparticles-enhanced RS over other methods such as SERS and TERS include good controllability of dielectric microparticles, simple synthesis process and adaptability to versatile samples.

5.2 Experimental details

The samples, which are Si substrates covered with a monolayer of silica microparticles were prepared using the self-assembly method. First, Si substrates, cleaved into 10×10 mm^2 pieces along the crystal direction, were cleaned by ultrasonic agitation in methanol, acetone and deionizer water for five min each. The prepared substrates were then placed into a bath of freshly-prepared Piranha solution (H_2SO_4/H_2O_2, 7:3). Hydrofluoric (HF) acid was then used to remove the oxide film. After the substrates were rinsed thoroughly with deionized water and ethanol, they were ready for self-assembly of silica particles. The fixed substrates were tilted with an angle (40°~ 60°) to the base. A drop of surfactant was applied on the substrate to reduce interfacial tension on the surface. After the surfactant was air dried, a drop of monodisperse suspensions (10% solution of silica microparticles) was dropped on the tilted samples to obtain a hexagonally closely-packed assembly of silica particles over an area of around several hundred square microns.

The enhanced RS experiment was conducted using the micro-Raman spectrometer. The instrumental setup is illustrated in Fig. 5.1.The detailed description of the system can be found in Chapter 4. The system is capable of testing samples in three different modes: the point mode (obtaining the Raman spectra at a specific point), line

mode (line scanning to locate the interested area), and zone mode (Raman mapping in a specified region). The sample was placed on a motorized motion stage with a resolution of 3.175 μm. A Raman shift resolution of 3.15 cm^{-1} can be achieved through an optical grating with a density of 600 g/mm.

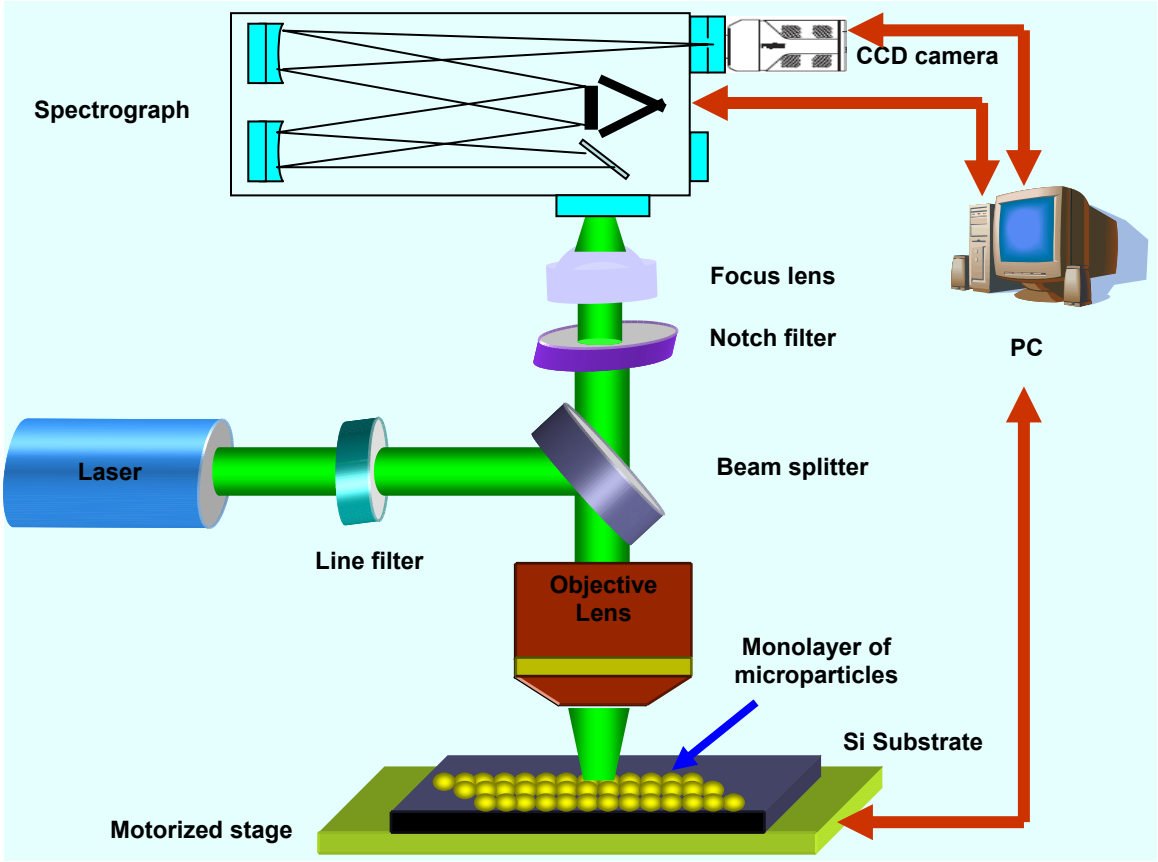

FIGURE 5.1 Experiment setup for measuring microparticles-enhanced Raman scattering using the micro-Raman spectrometer.

Because the Si substrate surfaces were not fully covered with the silica particles, the samples were first measured with the line mode to locate the interested region, during which the Raman spectra were recorded with the point mode. A CCD camera was placed in front of the notch filter to capture the particle images in scattering mode. The brightness of the camera was adjusted in order to obtain pictures with high contrast. The

surface morphologies of the samples were observed through an optical microscope (Olympus, BH-2) equipped with a high-resolution CCD camera.

5.3 Scattered optical images by the microparticles

Spherical silica particles with nine different diameters (0.33, 0.52, 0.81, 1.01, 1.52, 2.34, 3.22, 3.93, and 5.08 μm) were studied to find the dependence of particle sizes on the Raman scattering. Figures 5.2(a) and (b) show the two prepared sample covered with the 2.34 um and 1.01 um silica particles, respectively.

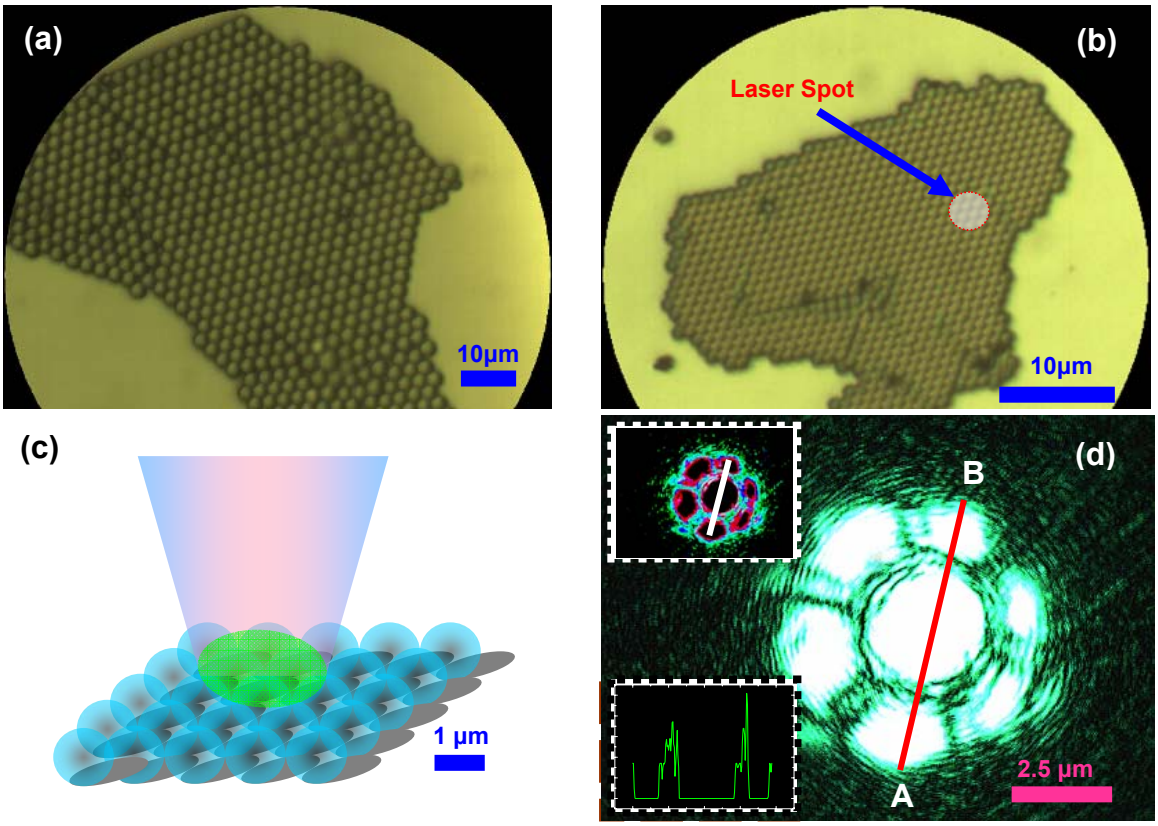

FIGURE 5.2 (a) Surface morphology of the Si substrate covered with the silica particles of 2.34 μm by optical microscope; (b) surface morphology of the Si substrate covered with the silica particles of 1.01 μm by optical microscope; (c) schematic diagram of the closely-packed silica particles of 1.01 μm illuminated by a focused laser beam;,(d) image in scattering mode for the silica particles of 1.01 μm. The part enclosed area in white color in (c) indicates the incident laser beam. The bottom left inset is the profile of (d) along the line AB, while the top left inset is the contour of (d).

The focused laser spot at the wavelength of 514.5 nm can cover 1.01 μm particle and part of its six adjacent particles, as shown in the schematic diagram in Fig. 5.2(c). A large circular spot in the center and six fan-shaped spots surrounding the center spot can be clearly observed. The optical image of this illumination pattern is shown in Fig. 5.2(d), from which we can see that the image is not perfectly symmetrical because of the limited step resolution of the stage. The image resulted from the reflected as well as the scattered light, including Rayleigh and Raman scattering. The upper-left inset in Fig. 5.2(d) is the contour of the image, while the bottom-left inset gives the profile. Clearly, the image shape in the scattering mode is determined by the geometries of both the particles and the laser beam (size and beam shape). Since the particle size and beam geometry were known in the experiment, the beam size could be estimated through the observed image. In Fig. 5.2(d), two to three particles are contained along the line AB, indicating the beam size is between 2.02 and 3.03 μm, probably around 2.5 μm, verifying our previous estimation. Furthermore, the beam size can be figured out through the size dependence of Raman scattering, as discussed afterwards.

5.4 Enhanced Raman spectra of Si substrates covered with microparticles

The intensity of the scattered Raman signal from the particles illuminated by a focused laser spot is dependent on the beam parameters (wavelength, power, mode, and beam size) and the particle properties (size and complex index of refraction). The Raman spectra of the Si substrates covered with the silica microparticles of different sizes from 0.33 to 5.08 μm as well as the Raman spectrum of the bare Si substrate as a reference are shown in

Fig. 5.3. We can see that the Raman signals around 520 cm-1 for all the particles were enhanced, as compared to the Raman signal for the bare Si.

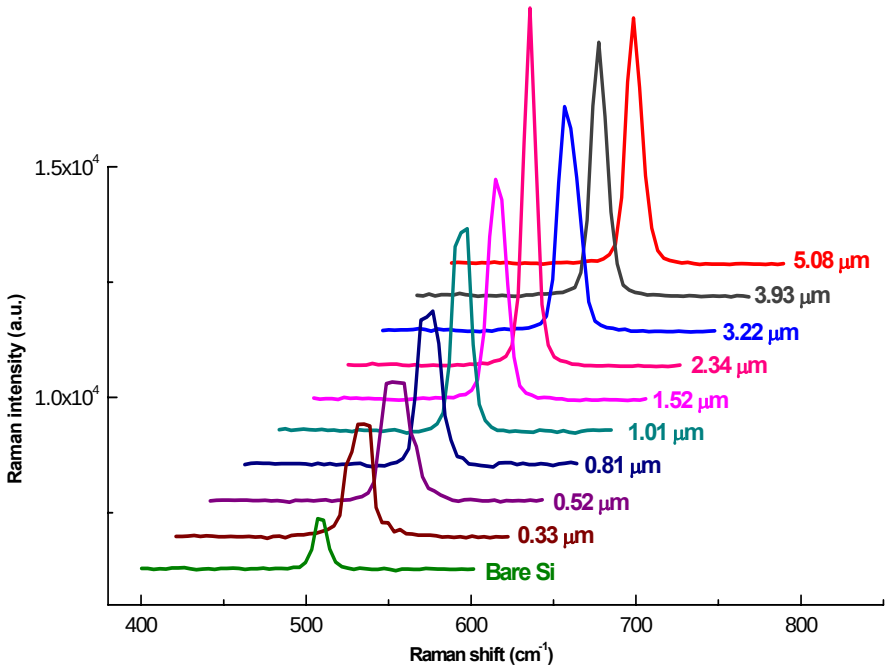

FIGURE 5.3 Raman spectra of the bare Si and the Si substrates covered with the different sizes of silica particles with the diameter from 0.33 to 5.08 μm.

In the calculation of the Raman signal intensity, the three highest points near the peak were averaged and the background signal was subtracted. The obtained data were applied to calculate the Enhancement of Raman Intensity (ERI), defined as the ratio of the net enhanced Raman intensity of the Si substrates (background subtraction) covered with microparticles to the net intrinsic Raman intensity from the reference Si (background subtraction). However, in order to calculate the enhcancement factor, the scattering volume must be considered. The penetration depth of the far-field light in Si is around 500 nm. Then the far-field volume was calculated as 2.45 μm^3. The penetration

depth of the near-field nanojets is 100 nm (calculated value). The diameter of the beam in near field is around 120 nm (calculated value) for the 2.34 μm particles. Thus, the near-field volume is around 1.13×10^{-3} μm^3. Thus, the enhancement factor for the 2.34 μm particle was calculated to be as high as 1.4×10^4, comparable to the enhancement factor reported using the tip-enhanced mechanism, which is 1×10^4 [14].

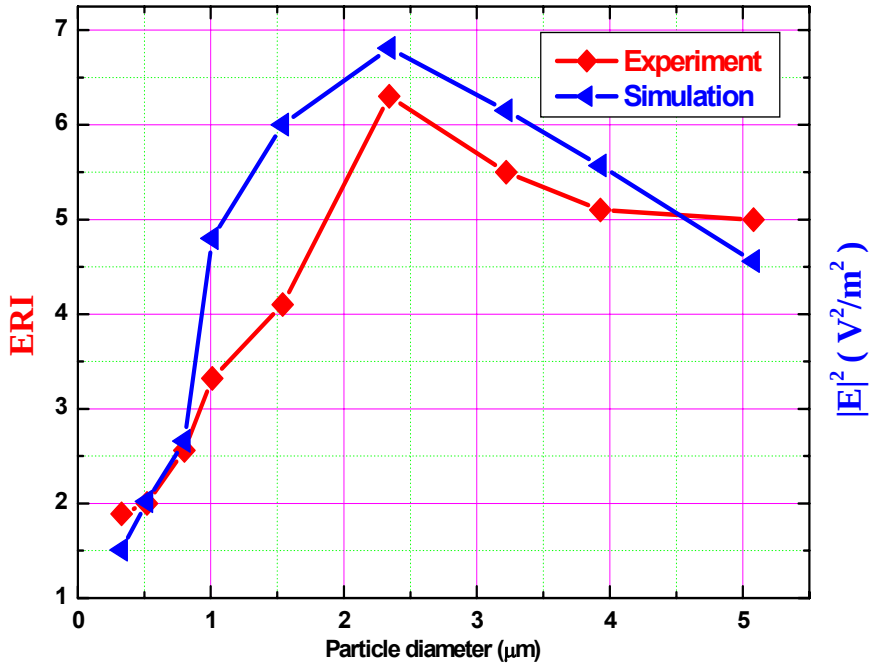

FIGURE 5.4 Size dependence of ERI in experiments (diamonds) and size dependence of $|E|^2$ in calculations (triangles).

Figure 5.4 shows the dependence of the particle sizes on the ERI obtained experimentally (diamonds) and calculated dependence of the particle sizes on the $|E|^2$ (squared electrical filed) in calculations (triangles), both of which agree with each other well. As particle sizes increase, the ERI increases continuously when the particle size are smaller than 2.34 μm,, but starts to decrease when the particle sizes are larger than 2.34 μm. The maximum ERI at 2.34 μm might indicate that this diameter is close to the waist

of the incident laser beam (2.5 μm). Thus, the particle size is an important factor for the optimization of the enhancement.

5.5 Conclusion

We prepared Si substrates covered with spherical silica microparticles to study the particle-enhanced Raman spectroscopy for the first time in the field. It is observed that the Raman peaks of Si could be significantly enhanced with the micrometer dielectric particles, due to the nanojets effect. An enhancement factor of 10^4 was achieved. In addition, this technique features good controllability of dielectric microparticles, simple synthesis process and adaptability to versatile samples, as compared to other enhancement methods. However, we point out that the samples in our experiments have to be specially prepared, such as using the self-assembly method, which might limit its application.

CHAPTER 6 ENHANCED RAMAN SPECTROSCOPY BY COMBING A METALLIC TIP WITH SURFACE NANOSTRUCTURES

6.1 Introduction

Tip-Enhanced RS (TERS), which is a noninvasive an optical characterization technique with a noninvasive fashion and especially with a high spatial resolution far beyond the optical diffraction limit, has attracted great attention largely because of its potential applications in a variety of areas such as microscopy, spectroscopy, optoelectronic devices, molecular electronics, semiconductor nanodevices and biophotonics. [1-3] For instance, by using a Ag -coated dielectric AFM tip as a light enhancer, the nanoscale residual stresses in Si devices have been characterized [4]; using a Au (Au) tip and an STM or a sensitive shear-force feedback system, single molecules and the individual SWCNT have been be resolved [5, 6]. In both cases, the tips served as the optical antennas by which highly localized and significantly enhanced optical fields were generated when they were irradiated by laser beams. The driving forces of this enhancement come from two sides: 1) the LSPs on metal surfaces due to the optical response of the metal on laser wavelengths, and 2) the "lightning-rod" effect due to the tip singularity. Currently, the exploration on LSPs is growing rapidly, driven by its potential applications in ultrafast optical switching, optical tweezers, biomolecular labeling, optical filter and waveguide design, chemosensing, radiative decay engineering, and SERS [7]. The SERS, an analogue of TERS, has been extensively investigated in the past decade, especially for single molecule detection [8, 9]. Compared to SERS, the TERS has much lower sensitivity, i.e. 10^5 to 10^{14} in terms of enhancement factor. This significant enhancement of SERS originates from the strong Surface Plasmons Resonance (SPR) induced by some "hot sites" created on SERS-active substrates with metallic nanoparticles, fractals, nanoclusters or nanostructures [7, 10].

Among those SERS-active substrates, the substrates with metallic nanostructures become increasingly popular because of two reasons: 1) they can be fabricated conveniently and controllably, and 2) their optical responses can be tuned intentionally and precisely. The nanostructures on the substrates, such as metal strips, nanorods, bow-tie particles, nanodiscs, spheres, core-shell structures, etc., can be fabricated by different processes [8]. Nanosphere Lithography (NSL), pioneered by Van Duyne and co-workers, is one of major methods to fabricate large arrays of nanostructures [11]. While metallic nanostructures have been extensively explored in SERS, they are rarely reported for TERS applications. Recently, surface roughness, nanoparticle or nanogap has been found to be able to further increase the Raman intensity in TERS. For instance, Zhang *et al.* experimentally and theoretically demonstrated that the nanoscale roughness formed by a nanoscale sharp step of 2 nm on the Au surface can significantly increase the TERS intensity by an order of magnitude [12]. Olk *et al.* studied a RS enhanced by two particles, and found that the additional Ag particle can enhance optical fields more significantly when the particles and the tip are properly aligned [13]. Since both the nanostructures and the tip serve as the optical nanoantennas, the interactions between the LSPs excited from the nanostructures and the tip might be strongly coupled, resulting in higher Raman intensities. This coupling can lead to dramatic changes of both the spatial distribution and the magnitude of the scattered electric field. As a result, the combined use of nanostructures with TERS may provide us an efficient approach to further improve the detection sensitivity.

Based on this idea above, we developed a technique, by combining TERS with the metallic nanostructures, to further improve the detection sensitivity of RS. The self-

built TERS system using an STM and the side-illumination optics, also referred to as a gap-mode TERS, has been demonstrated in Chapter 4. Using this TERS system, we characterized the Raman spectra of the substrates with triangular Ag nanostructures fabricated using the NSL. Comparing the Raman intensities from these nanostructures and the bare substrates, we found that those Ag nanostructures could further enhance the Raman intensity of the Si substrates by an order of magnitude.

6.2 Experimental details

Figure 6.1(a) shows the schematic diagram for the physical concept of the nanostructure-assisted TERS technique. A highly localized and significantly enhanced optical field can be induced due to the interaction between the LSPs from the tip and the surrounding nanostructures, when the focused laser beam, the tip, and the nanostructures are properly aligned. The enhanced local optical field can be significantly higher due to the presence of the nanostructures. Figure 6.1(b) shows the schematic diagram of the TERS system used to measure the enhanced Raman spectra and perform Raman imaging with nanoscale resolutions.

Two types of tips, i.e., the Au and Ag-coated W tips, were used in the experiments. The Au tips were fabricated by a direct current electrochemical etching apparatus in which a solution prepared using analytical grade fuming hydrochloric acid and ethanol (Merck) was used to etch a Au wire (Aldrich) with a diameter of 0.25-mm. A bias voltage of 2.4 V was applied between the cathode (the Au wire) and the anode (a Cu ring) to drive the etching for about 5 minutes. The anode is a ring, because this shape is helpful to achieve a smooth tip. To fabricate a W tip, a W wire (Aldrich) of 0.25-mm diameter was immersed in a solution of the mixture of concentrated $HClO_4$ and pure

methanol (1:4) at an anodic voltage of 1.8 V. The etching time was around 9 min, at which the W tip became around 50 nm. Then the W tip was coated a 40-nm thick layer of Ag with a sputtering system.

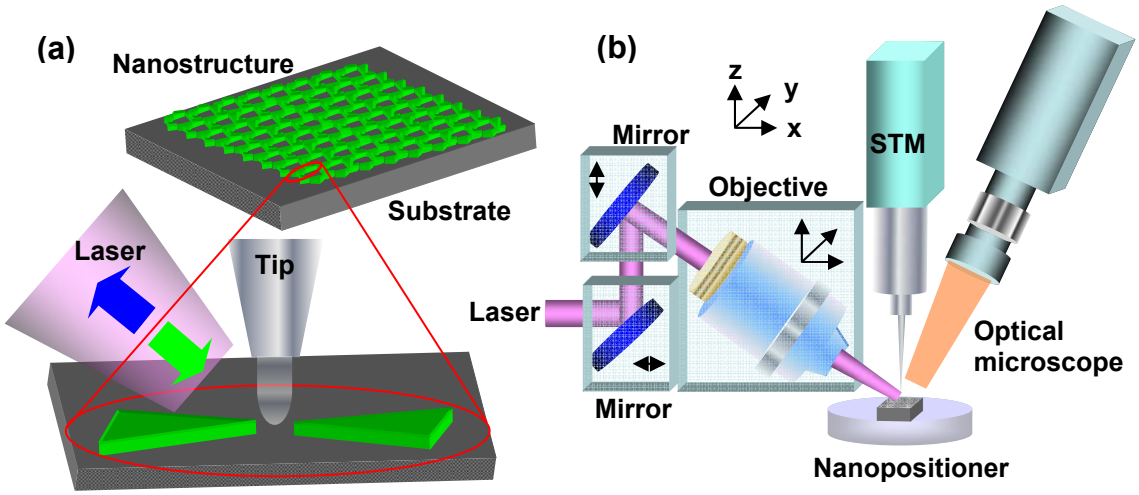

FIGURE 6.1 Schematic diagrams of (a) nanostructure-assisted TERS and (b) TERS system used in experiments.

The Ag nanostructures were fabricated by the Nanosphere Lithography (NSL) [14, 15], which typically includes five steps: the substrate cleaning, the solution dropping, the self-assembly of nanoparticles, the sputtering of metallic layer, and the lift-off, as shown in Fig. 6.2. Each NSL structure begins with the self-assembly of size-monodisperse nanospheres to form a 2D colloidal crystal deposition mask. The methods of depositing a nanosphere solution onto the desired substrate include the spin coating, the drop coating, and the thermoelectrically cooled angle coating. All of these deposition methods require that the nanospheres be able to freely diffuse across the substrate, so that a lowest energy configuration of these nanospheres can be formed. As the solvent (water) evaporates, the capillary forces draw the nanospheres together, and the nanospheres

crystallize in a hexagonally close-packed pattern on the substrate, forming a nanosphere mask on the substrate. A metal or another material is then deposited to the substrate through the nanosphere mask to a controlled mass thickness by using DC sputtering from a source normal. After the metal deposition, the nanosphere mask is removed by sonicating the entire sample in a solvent, leaving behind the deposited material on the substrate.

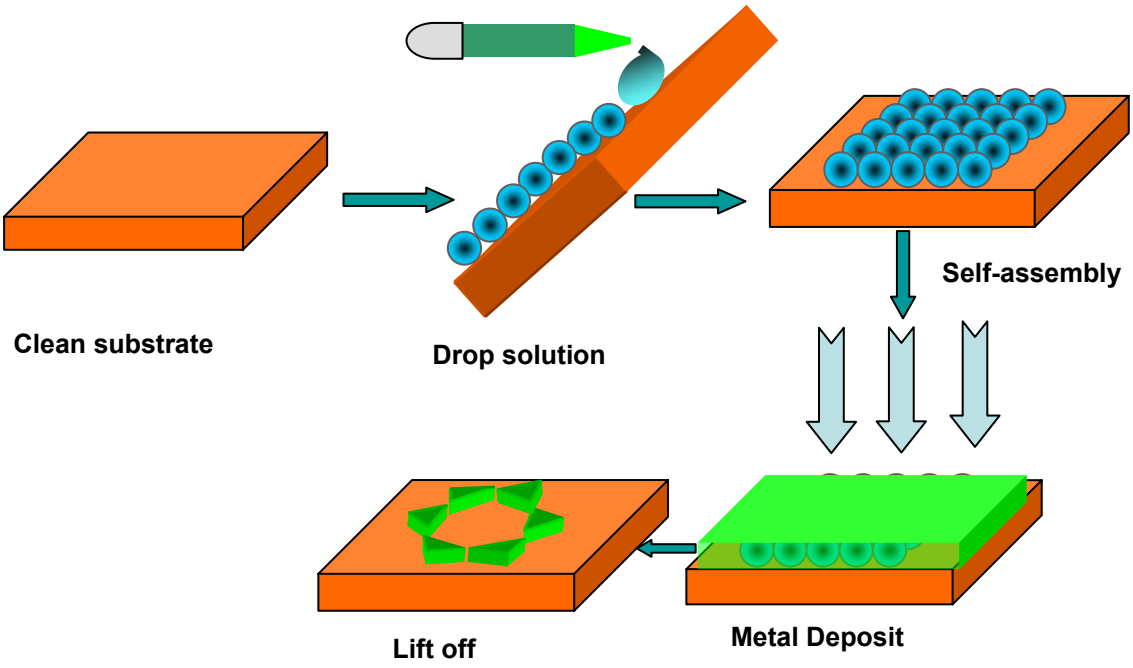

FIGURE 6.2 Procedure of nanosphere lithography.

6.3 Nanostructures fabricated by nanosphere lithography

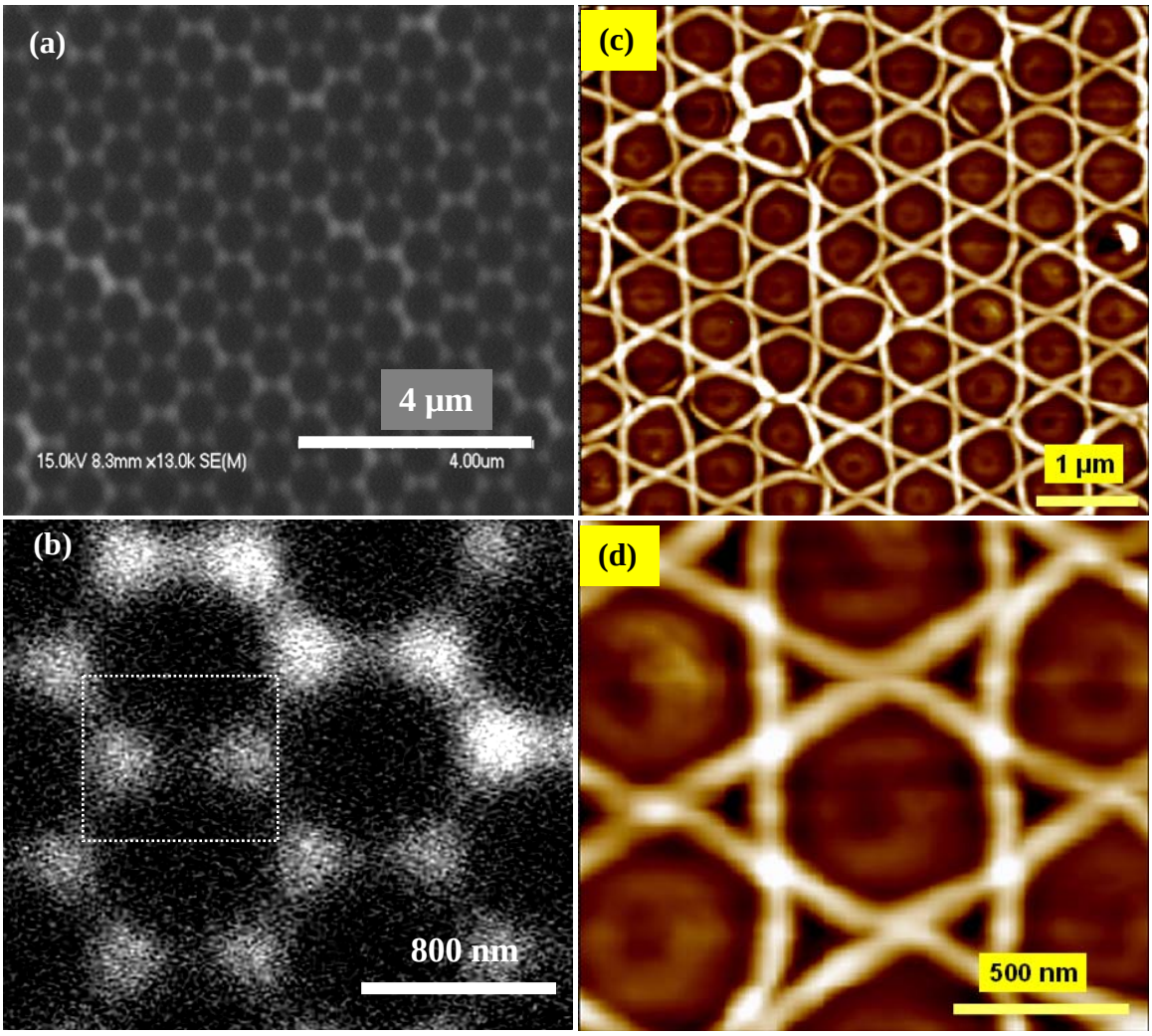

FIGURE 6.3 SEM micrographs of the triangular Ag nanostructures in (a) the normal and (b) the zoomed views; AFM micrographs of the ring-shaped Ag nanostructures in (a) the normal and (b) the zoomed views.

Different shapes of nanostructures were fabricated using the NSL technique. Figures 6.3(a) and 6.3(b) show the SEM micrographs of the triangular Ag nanostructures on Si surfaces in the normal and the zoomed views, respectively. They have triangle geometries with a side length of around 200 nm and a tip-to-tip distance of around 100 nm. Figures 6.3(c) and 6.3(d) show the AFM micrographs of the ring-shaped Ag

nanostructures in the normal and the zoomed views, respectively. It can be seen that the minimum gap distance between two nanostructures is around 20 nm, or less.

6.4 Raman spectra of Si substrates under different conditions

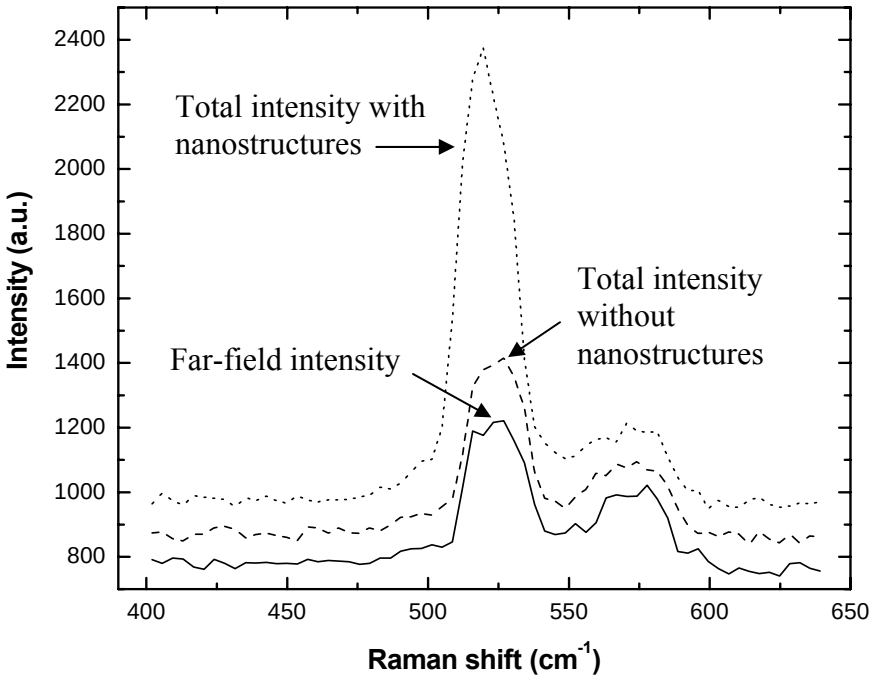

FIGURE 6.4 Raman spectra of the Si substrate under different cases: signals from far field only (solid trace), sum of signals from far field and near field in the absence of the nanostructures (dashed trace), and in the presence of the nanostructures (dotted trace).

TERS is an essential tool for the characterization of Si-based devices in nanoscales. For instance, the nanoscale residual strains, which are directly related to the carrier mobilities in Si, can be characterized by measuring the Raman shifts with respect to the vibration mode of 520 cm^{-1} [16-19]. In addition, the distribution of the strains is useful to identify the device performance. Under normal conditions, the enhancement contrast ratio, defined as the ratio of near-field to far-field Raman intensity, is usually 50%, which is not sufficient to obtain a clear Raman image. Suppressing the far-field signals using a

doparization technique has been proposed to increase the ratio. In this study, we demonstrated that this ratio can also be increased by increasing the near-field signals using the nanostructures-assisted TERS technique. Figure 6.4 shows the Raman spectra of the Si substrate for three different cases: signals from the far field only, sum of signals from far field and near field (total intensity) in the absence and in the presence of the nanostructures. All spectra were accumulated with a time period of 1 sec. In the absence of the nanostructures, the contrast ratio is around 40%, in agreement with the previous report. When the nanostructures are present, the contrast ratio is increased up to 250%, which is more than 5 times higher than the contrast ratio obtained without the nanostructures. We also found that the strongest enhancement occurred when the tip was positioned in between the apexes of two adjacent nanostructures [see Fig. 6.3(b)] by mapping a certain region, which will be discussed later. The enhancement factor (EF), which is a widely accepted term in this field, is generally defined as the actual signal enhancement per scattering volume, i.e., [6]

$$EF = \frac{I_{near-field}}{I_{far-field}} \bullet \frac{V_{far-field}}{V_{near-field}} = \left(\frac{I_{total}}{I_{far-field}} - 1 \right) \bullet \frac{V_{far-field}}{V_{near-field}} . \qquad (6.1)$$

Here, $I_{near\text{-}field}$ and $I_{far\text{-}field}$ refer to the near-field and far-field Raman intensities, respectively. $V_{near\text{-}field}$ and $V_{far\text{-}field}$ refer to the near-field and far-field scattering volumes, respectively, and $I_{total\text{-}field}$ refers to the total Raman intensity, which is the sum of the far- and near-field intensities. The term $I_{near\text{-}field}$ / $I_{far\text{-}field}$ in Eq. (6.1) is the enhancement contrast ratio, which is 250% in this study. For a Si sample, $V_{far\text{-}field}$ is defined as the surface area of the focused laser beam times the smallest one of three parameters: the sample thickness, the light penetration depth or the focus depth. The light penetration depth, D, which can be estimated using $D = \lambda/4\pi k$, with k being the extinction coefficient

of Si at the wavelength λ. Using the value of k = 0.06 at λ = 514.5 nm, i.e., the wavelength of the excitation laser, the light penetration depth is estimated to be 0.68 um. The focused beam diameter is estimated as 3 μm. Subsequently, the far-field scattering volume is $1500^2 \times 680 \times \pi$ nm^3 ≈ 4.8×10^9 nm^3. The near-field scattering volume depends on the tip radius and the decay length of the enhanced optical fields. Because the radius of the enhanced optical fields is one half of the tip radius [20], it is estimated to be 12.5 nm in this study. The decay length of the enhance field is estimated to about 2.5 nm. Then, the near-field scattering volume is $12.5^2 \times 2.5 \times \pi$ nm^3 ≈ 1.23×10^3 nm^3. As a result, the *EF* is calculated to be 9.75×10^6, which is more than one order higher than the reported results without the surface nanostructures.

6.5 Raman mapping of nanostructures on Si surfaces

Near-field TERS is able to resolve individual nanostructures. When the tip is right on the top of the nanostructures on the silicon substrate, the Raman signal of Si can not be excited because the Si surface around the tip apex region is blocked by the nanostructures. When the tip is placed in between the terminal ends of two adjacent nanostructures (dipole), a significant Raman enhancement can be observed. When the tip is located in the lift-off area, only the normal tip enhancement is present. By identifying different Raman intensities, Raman mapping images can be obtained. These images can be used to differentiate different regions. Fig. 6.5 shows the image of the rectangular area enclosed with dashed lines in Fig. 6.3(b). It is clearly seen that the individual nanostructures have been spatially resolved, leading to a conclusion that the system has a spatial resolution below 100 nm. We attribute this significant Raman enhancement to the strong coupling between the LSPs from the tip and the nanostructure dipole. The metallic nanostructures

have nanopyramid geometries, as shown in Fig. 6.3(b), therefore it is easy to understand the significant enhancement occurs between the dipole tips, because the Raman signal in this gap is the highest. The enhancement of the localized optical fields in the proximity of the dipole tips is determined by several factors such as the material, geometry, angle and radius of curvature of the tip, and the wavelength of the excitation light[21].

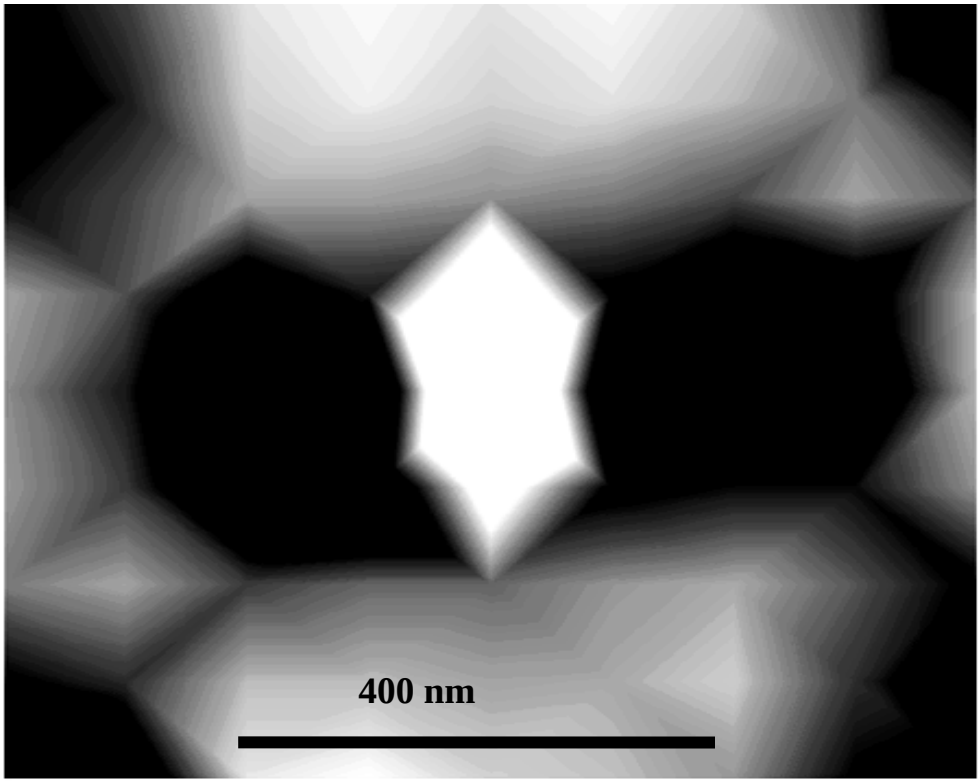

FIGURE 6.5 Raman mapping of the nanostructures. The scanning region corresponds to the area enclosed by the dashed lines in Fig. 6.3(b).

Matching these factors to an optimal condition might lead to an optical resonance, while can ultimately benefit the generation of extremely highly enhanced optical fields. Previous simulation and experiments concluded that increasing number of dipoles, for example, 2 dipoles, dipole chains or dipole arrays, might further enhance the optical fields [22]. Another interesting point is that the resonance frequencies vary with the

nanostructure geometries by either blue shift or red shift. We studied the dipole chains that are formed by the nanostructures periodically distributed in a large region on the Si substrate. It is unlikely that the enhancement comes from a resonant state of dipole chains because the obvious enhancement could not be observed when the STM tip didn't approach the nanostructure dipoles. The facts that the excitation wavelength in this study was 514.5 nm and the nanostructures had nanopyramid shape with a terminal distance of 100 nm further prove the optical resonance can not occur based on the reports by Jenson *et al.* On the other hand, the two tips of one nanostructure dipole and the STM tip may serve as three tip structures, leading to the formation of three dipoles. The three dipoles may be acting to further enhance the Raman signals either by increasing the region of interrogation by a factor of 2, for two separate dipoles or a resonant state of three tips. Our result, the Raman intensity enhancement of 2.5 in the presence of the nanostructures, strongly supports the analysis. It should be noted that different dipole-STM tip configurations lead to different enhancement. For instance, a combination of the local dipole created by the two triangular tips as they approach each other and the placement of the gap between the dipoles in relation to the substrate might affect the enhancement performance. Therefore the variation of the nanostructure geometries may affect the enhancement performance. As presented in Fig. 6.5, the significant enhancement selectively occurred near one specific dipole while the enhancements from the rest four dipoles were not obvious. Another explanation of this selectivity is that this enhancement is strongly dependent on the polarization direction of the incident laser and Si crystal orientation according to Raman selection rules [23].

6.6 Conclusion

In conclusion, a technique, using metallic nanostructures in conjunction with TERS, was developed to further enhance Raman signals. With this approach, a contrast ratio of 250% was achieved, which is more than 5 times of the contrast ratio obtained without the nanostructures. The Raman enhancement factor was calculated to be 9.75×10^{6}, which is more than one order of magnitude higher than the previously reported results obtained using tips only. This technique is promising for various applications such as biomolecualr labeling and nanodevice characterization.

CHAPTER 7 CHARACTERIZATION OF SINGLE-WALLED CARBON NANOTUBES USING THE RAMAN SPECTROMETER

7.1 Introduction

The large leakage currents induced from quantum effects seriously degrade the device performance for Si-based microelectronics when the feature size of devices approaches the physical limitation. It is predicted that the scalability of MOSFET devices will come to an end within a decade. This limitation has sparked intense researches for alternative technologies, new device physics and new materials. Carbon nanotube is a promising candidate due to its remarkable physical and electrical properties [1-4].

The Single-Walled Carbon Nanotubes (SWCNTs), envisioned as a honeycombed graphite sheet rolled into a 1D tube, has been successfully applied as the gate channel of field effect transistors (FET). The device demonstrated unparalleled and unprecedented performance [1]. The quantum confinement of the electrons in the circumference direction prevents the electrons from backscattering, thus a ballistic transport occurs, leading to enormously high current density. Meanwhile, the SWCNT metallic wires can effectively suppress the system noise. They can be semiconductor or conductor depending on the chirality or the (n, m) indices [5]. Previous studies revealed that SWCNT-based FET can be n-type, p-type or ambipolar with different gate voltages. The ambipolar behavior is crucial to optical sensor and light emitter, two of key components in optoelectronics. Consequently, developing all carbon based nanochips which comprise both optical and electronic processing elements is possible in the future. Recently, a simple logic circuit has been demonstrated using the SWCNT-based FET [6].

Topography is a direct approach to analyzing the defects and stresses in semiconductor devices. Both the SEM and AFM are popular tools used to study the structure of SWCNTs, and the transmission electron microscopy (TEM) is another

instrument to characterize the diameters and structure defects of the SWCNTs. The RS has demonstrated the incomparable capability of identifying the chiralities and diameters of nanotubes by studying the particular features of various vibration modes from Raman spectra. The Raman intensity can be highly enhanced from the resonance Raman behavior due to the sharp van Hove Singularities (vHS) in the electronic density of states. The Raman image of one individual SWCNT can provide rich information about the tube-like intermolecular junctions and the metal-semiconductor junctions [7].

The essential prerequisite for SWCNTs used in electronic devices is that their size, location, and orientation can be precisely controlled. Three methods can be used to fabricate the SWCNTs: the electrical arc discharge, the laser ablation, and the chemical vapor deposition (CVD). The CVD is the most widely used process for the direct SWCNT device fabrication. A laser-assisted CVD (LCVD) was recently proposed and has shown great potentials with several unique features over other conventional CVD process, such as the precise control of the growth position, the ambient furnace temperature, and the potential for the chirality selection of the nanotubes [8].

A home-made micro-Raman spectrometer, which has been demonstrated in Chapter 4, was used to characterize the SWCNTs grown between two Mo electrodes. The CNT-based devices with the MOSFET configuration on Si wafers were fabricated using the LCVD process. The SEM was used to characterize the morphology of the patterned Si and the location and shape of the SWCNTs. The Raman peaks of the SWCNTs from the Radial Breathing Mode (RBM) were found to be sufficiently strong to construct Raman images. The grown SWCNTs were found to be semiconducting. The SWCNTs grown on inverse-opal Si substrates was also characterized. Because the nanojets from

illuminated microparticles can enhance the Raman signals, we fabricated SWCNTs on the Si substrates, in which the nanotubes were covered by the silica microparticles. We characterized them using the microparticles-enhanced RS, of which the details can be found in Chapter 5. Finally, we used the TERS system to obtain the enhanced Raman spectra and the Raman image of the individual SWCNTs dispersed on the Si substrates.

7.2 Experimental details

The SWCNTs were grown between two Mo electrodes patterned on a p-type Si wafer covered with a layer of Si dioxide using the LCVD process. The oxide layer served as the gate dielectric material. Mo was used as the electrode material due to its high melting point (2625 °C).

The experimental setup is shown in Fig. 7.1. Briefly, Mo electrodes were fabricated by first depositing a 100-nm thick Mo film on a patterned photoresist using DC sputtering, followed by a lift-off process. Porous Fe-Mo-alumina was employed as the catalyst for SWCNT growth. The LCVD process was conducted in a vacuum chamber. A CW CO_2 laser (Synrad, Firestar v40, wavelength 10.6 μm) was used to irradiate the substrates. In order to grow well-aligned SWCNTs, an electric field between two electrodes was applied with a DC power supply. The magnitude of the DC bias varied according to the gap width, with typical values of 1–1.5 V/μm. The growth was monitored by an Ampere meter. When SWCNTs bridges across the electrodes, a current flow will be detected and then the process is terminated immediately to prevent SWCNTs from burning. The monitoring circuit was protected by a 10 kΩ resistor to avoid large short currents. Prior to the CVD process, the vacuum chamber was first pumped down to

1×10^{-3} Torr. Acetylene and ammonia (C_2H_2/ NH_3) gas mixture was then released into the chamber, with a volume ratio of 1 to 10. The gas pressure remained constant at 10 Torr during the entire process. During the laser irradiation, the substrate temperature under the laser spot was monitored using a pyrometer (Omega, single color OS 3750). The reaction temperature was controlled in the range from 690 to 720 °C and the growth period varied from 3 to 6 min.

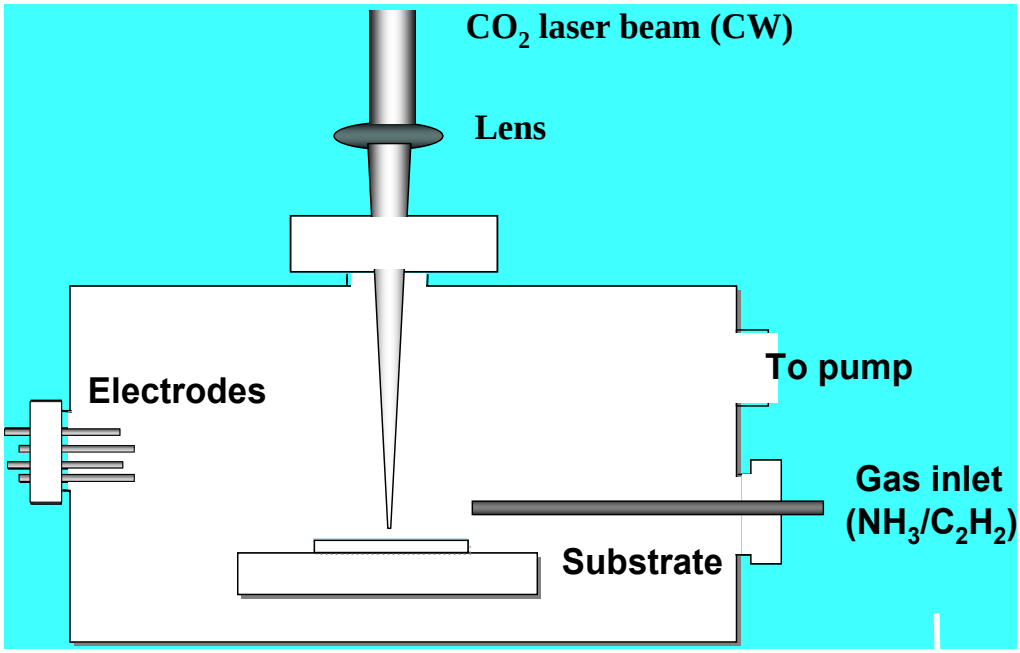

FIGURE 7.1 Experimental setup of the laser-assisted chemical vapor deposition system.

The inverse-opal Si substrates were formed using a a laser imprinting method. On the surface of these special substrates, hexagonally close-packed monolayers of particles (about 500 nm in diameter) were assembled on the Si surface. In the LCVD process, the feed gas was a mixture of acetylene and ammonia with a volume ratio of 1/10. The whole

process continued about 6 min with 35-mW laser (CO_2) power and 70-80 Torr reaction pressure.

The SWCNT samples covered with silica microparticles were prepared in the same method described in the experimental part of Chapter 5 except that the SWCNT powders were dispersed on the Si substrate prior to the self-assembly process.

The SWCNT samples used for the TERS experiments were prepared by the direct dispersion of solutions containing SWCNT powders on the Si substrate.

7.3 Raman characterization of SWCNTs at micrometer scales

7.3.1 Raman spectra and imaging of SWCNTS grown across two electrodes

The SWCNTs grown in between two electrodes are shown in Fig. 7.2. There are several individual nanotubes extending out from the electrode B, but only one (CNT 2) is successfully across the two electrodes. The minimum distance between two Mo electrodes is about 3 μm. It can be observed that the growth of CNT 2 is direction selective, i.e., it prefers the shortest path to bridge the gap of the electrodes. The other CNTs (CNTs 1 and 3) can be removed by some special techniques [9].

The full-range Raman spectra of CNTs 1, 2 and 3 are shown in Fig. 7.3. The typical bands of the RBM band (radial breathing mode, 181 cm^{-1}), D-band (disorder mode, 1340 cm^{-1}), G-band (tangential mode, 1591 cm^{-1}) and G´ band (overtone of D-band, 2668 cm^{-1}) are clearly observed. The Raman peaks of the Si at 520 cm^{-1} and the Si dioxide at 303 cm^{-1} are also observed since the tubes were grown on the Si substrate with 1 μm thick layer of silica on the top.

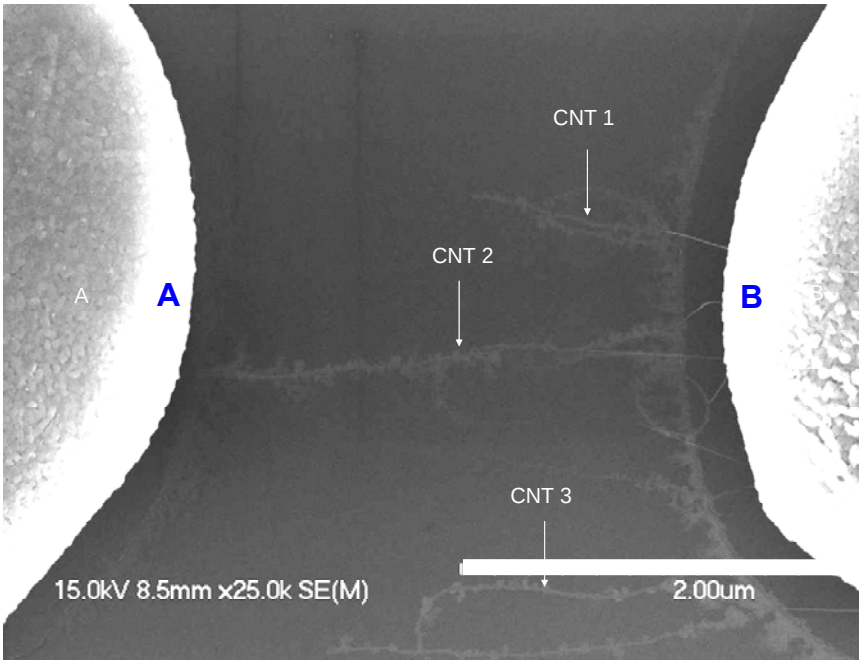

FIGURE 7.2 SEM micrograph of the SWCNTs grown between Mo electrodes A and B.

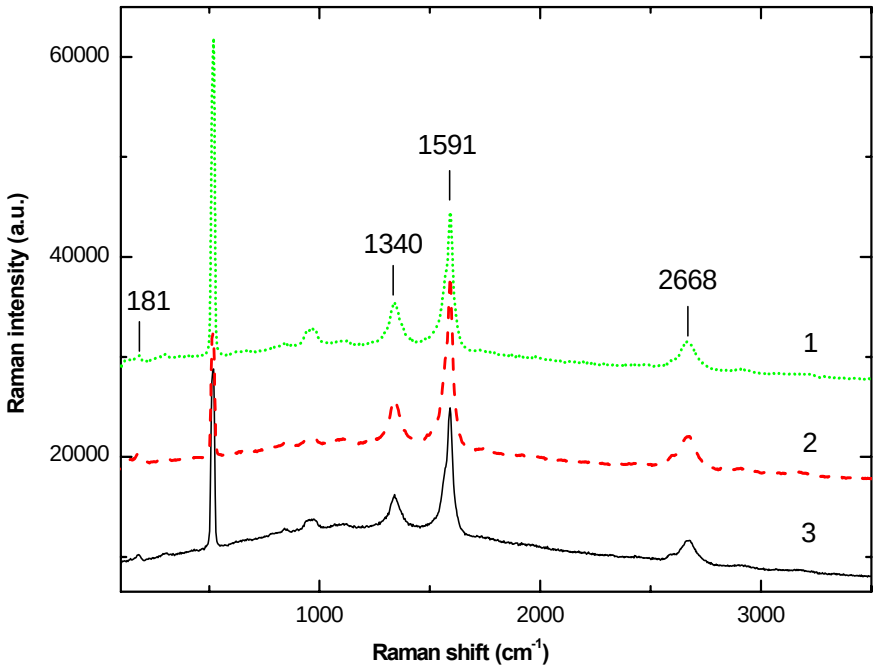

FIGURE 7.3 Full-range Raman spectra of CNTs 1, 2 and 3 grown in between two electrodes.

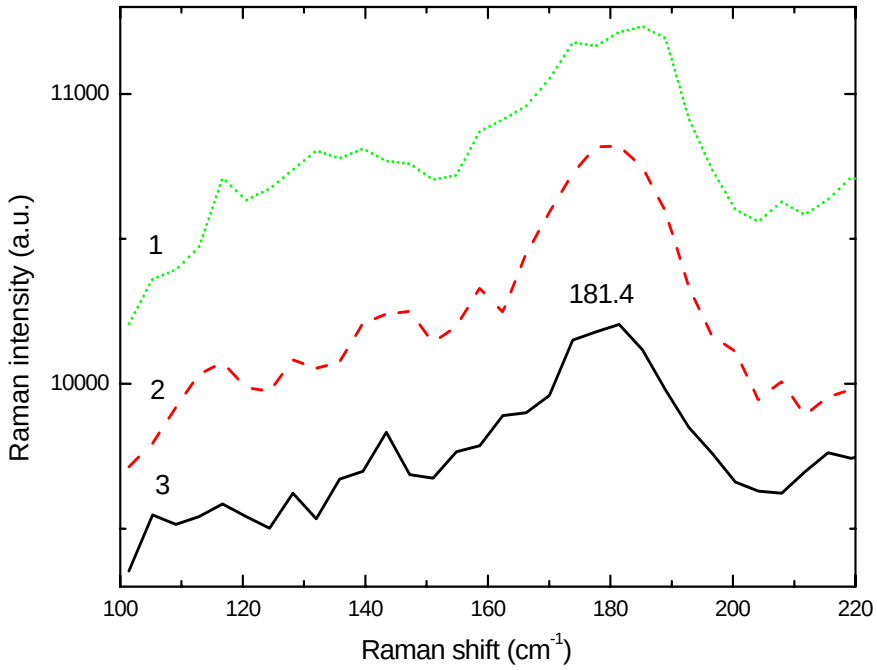

FIGURE 7.4 Raman spectra of the RBM band for the CNTs 1, 2 and 3 grown between two electrodes.

The RBM band, a unique feature of the Raman spectra of the SWCNTs with the frequency (ω_r) ranging from 120 to 350 cm^{-1}, denotes that the CNT is single-walled. In addition, it can also be used to estimate the diameter of the CNTs, probe the electronic structure of the CNTs, and perform the (n, m) assignment to the CNTs [10, 11]. This spectral feature is directly related to the coherent vibration of the carbon atoms in the radial direction, as if the tube is "breathing". Only those SWCNTs with diameters ranging from 0.7 to 2 nm exhibit the RBM band. It has been theoretically and experimentally proven that the frequency of the RBM has a direct relation with the diameter (d_t) of a SWCNT, i.e., $d_t = 224/\omega_r$ [12]. In our case, the RBM band occured at around 181 cm^{-1} for all the three CNTs, indicating their diameters were about 1.24 nm, which agrees with the TEM result well. The high similarity of the diameters of the three

CNTs evidences that homogenous CNTs can be fabricated using our synthesis process. The stable growth temperature might be one of the reasons for this uniformity.

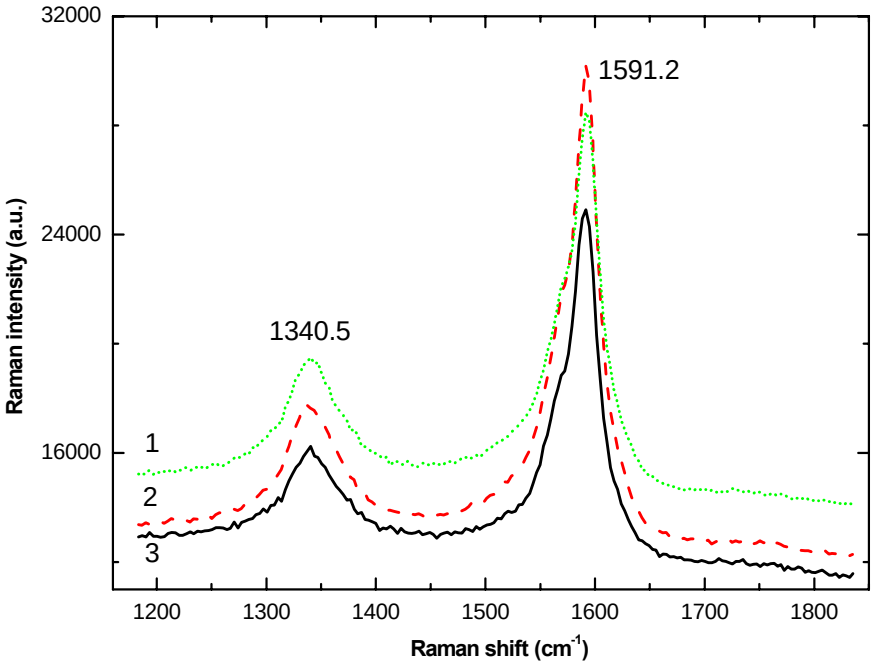

FIGURE 7.5 Raman spectra of the D and G-band for the CNTs 1, 2 and 3 grown between two electrodes.

The G-band of the SWCNTs is inherited from the graphite, involving an optical photon mode between two dissimilar carbon atoms in the unit. However, the G-band of the graphite has only one Lorentzian peak at 1582 cm^{-1}, while the G-band of the SWCNTs has several peaks which can be decomposed by the Lorentzian fitting. The G-band of the SWCNTs can be used to distinguish the metallic and semiconducting tubes, probe the charge transfer and study the selection rule in various Raman scattering processes and scattering geometries [13].

Figure 7.5 shows the spectra of the D-band and G-band of the tubes. Figure 7.6 shows the G-band spectrum of CNT 2 and the spectra obtained using the Lorentzian fitting. The dotted curve is for the origin data, and fitted curve is solid. The fitted curve is further decomposed into two individual curves (dashed line), i.e., the G^+ (1591 cm^{-1}) and G^- (1569 cm^{-1}) bands, respectively. This band has two types of lineshape, i.e., the Lorentzian lineshape and the Breit-Wigner-Fano lineshape, as shown in Fig. 7.6, which can be used to determine whether the SWNT is semiconducting or metallic [14]. The Lorentzian lineshape denotes a semiconductor tube and the Breit-Wigner-Fano lineshape denotes a metal tube. Based on this criterion, all the CNTs we fabricated are semiconducting as their spectra exhibit the Lorentzian lineshape.

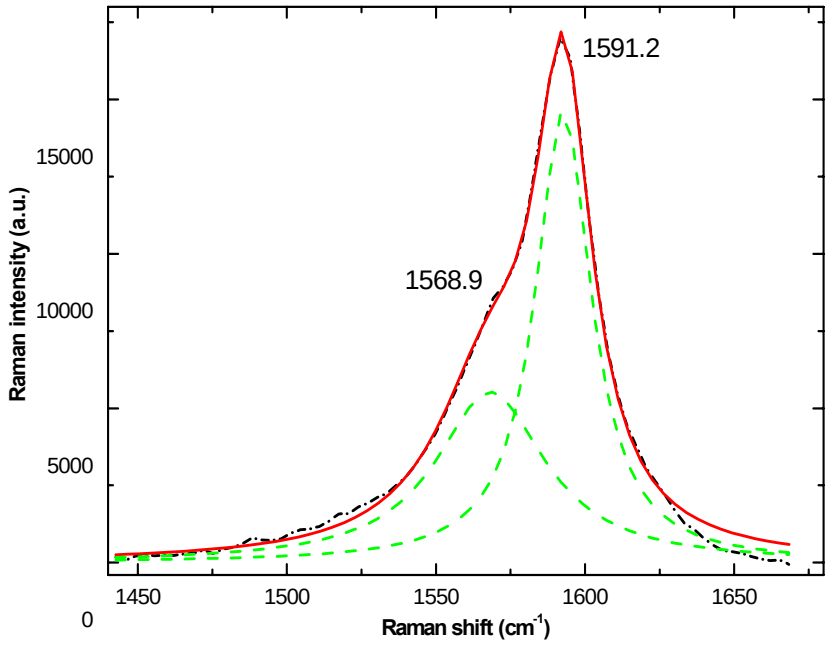

FIGURE 7.6 Lorentzian fitting of Raman spectrum of the G-band for the CNT 2.

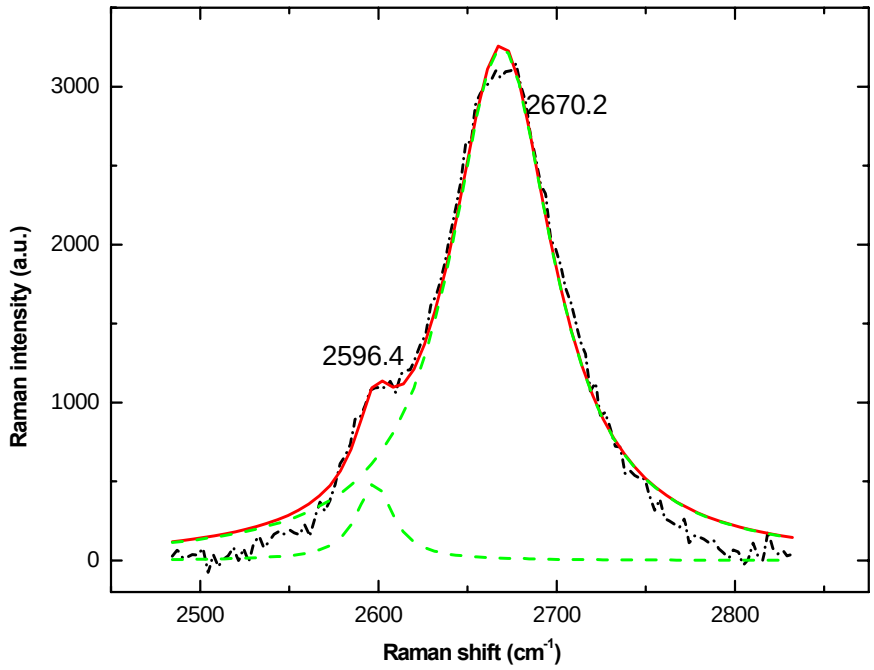

FIGURE 7.7 Raman spectra and Lorentzian fitting of the G´-band for the CNT 2.

The G´ band at 2668 cm^{-1}, i.e., the second harmonic band, is shown in Fig. 7.7. The double resonance features are commonly found in the Raman spectra of the SWCNTs due to the disorder-induced mode from the defects in the tubes [15]. Both the D and the G´ bands are sensitive to the diameter and chirality of the SWCNT. They can be used to determine the magnitude of the trigonal warping effect in the electron and photon dispersion relations. The two-peaks after fitting, 2596 and 2670 cm^{-1}, demonstrate that they are specially (n, m) isolated SWCNTs. This can be explained by combining the double-resonance effect with the singular structure of the SWCNTs. The G´ band is strongly dependent on Joint Density of States (JDOS), thus providing rich information about the electronic structure and the (n, m) indices for the specific SWCNT that is in resonance with the excitation photons, which is the fundamental of selectively removing unwanted CNTs using lasers.

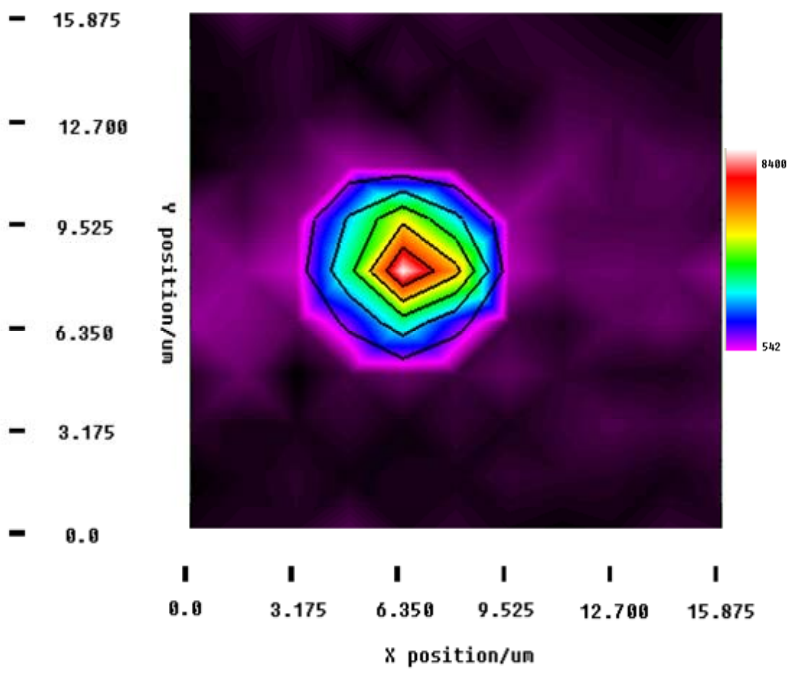

FIGURE 7.8 2D Raman imaging of the SWCNTs grown between two electrodes.

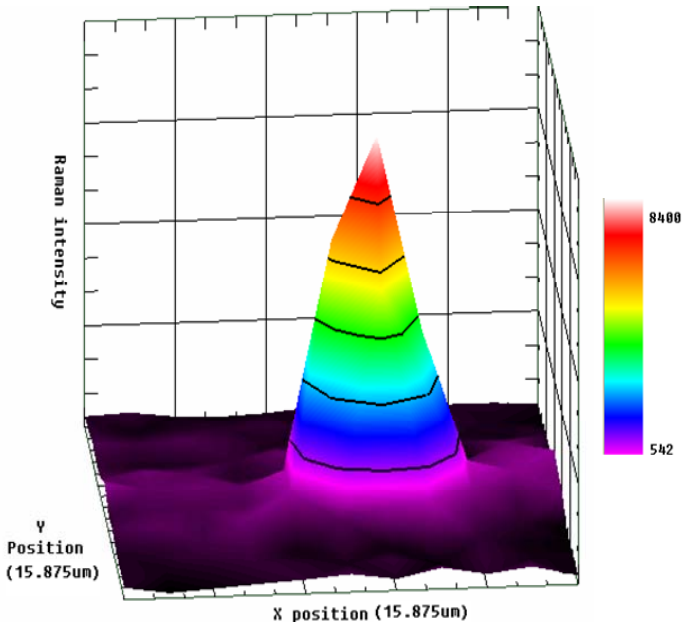

FIGURE 7.9 Pseudo 3D Raman imaging of the SWCNTs grown between two electrodes.

Figures 7.8 and 7.9 show the 2D and pseudo 3D Raman images of the CNTs obtained using the mapping function of the developed Raman spectrometer. The Raman peak of the RBM mode was used as the fingerprint to perform the Raman mapping. It can be observed that the individual SWCNT can not be resolved because the size of laser spot is much larger than that of one individual SWCNT. This limitation can be circumvented by using the TERS [16, 17].

7.3.2 Raman spectra of SWCNTs grown on inverse-opal Si substrates

Figure 7.10 shows the SEM micrograph of the SWCNTs grown on the inverse-opal Si substrate. The SWCNTs form a suspended network on the patterned Si arrays with the density of 6 tubes per square micrometer. Figure 7.11 shows the Raman spectrum of the SWCNTs. The peak in the RBM band is 187 cm^{-1}. By using the relationship between the SWCNT diameter and Raman shift, the average diameter of the SWCNTs was estimated to be 1.33 nm. The peak in the G band is 1582 cm^{-1}. It was interesting that the Raman intensities of the SWCNTs on this substrate are much higher than the intensities from the SWCNTs on the flat substrate, indicating that the surface roughness helps to enhance the Raman intensities. Figures 7.12 and 7.13 show the Lorentzian fittings of two distinguished bands, the RBM and G bands, respectively.

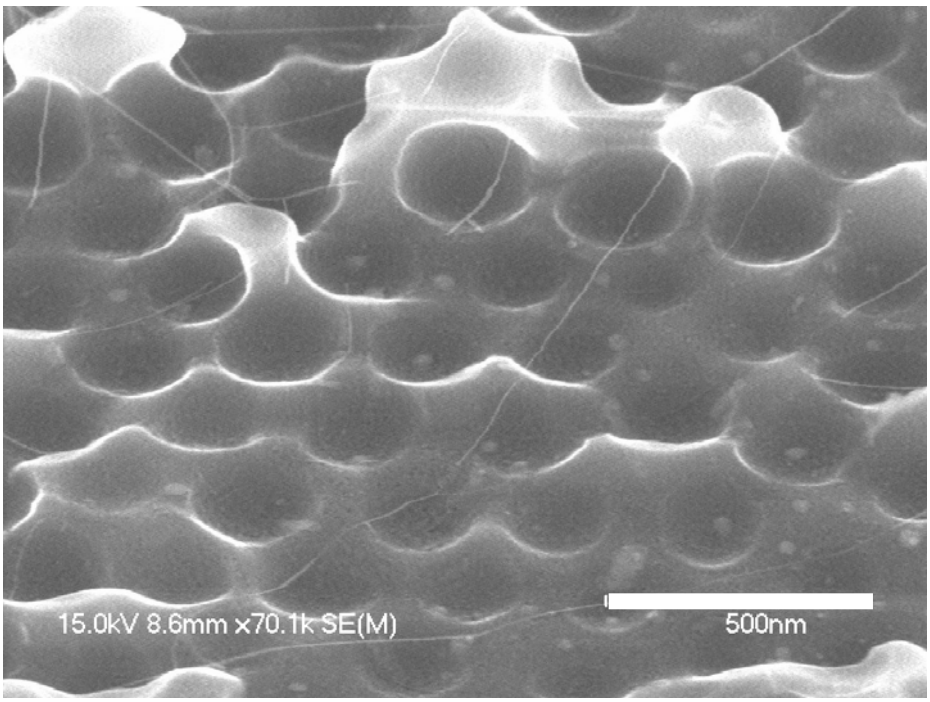

FIGURE 7.10 SEM micrograph of the SWCNTs grown on the inverse-opal Si substrate.

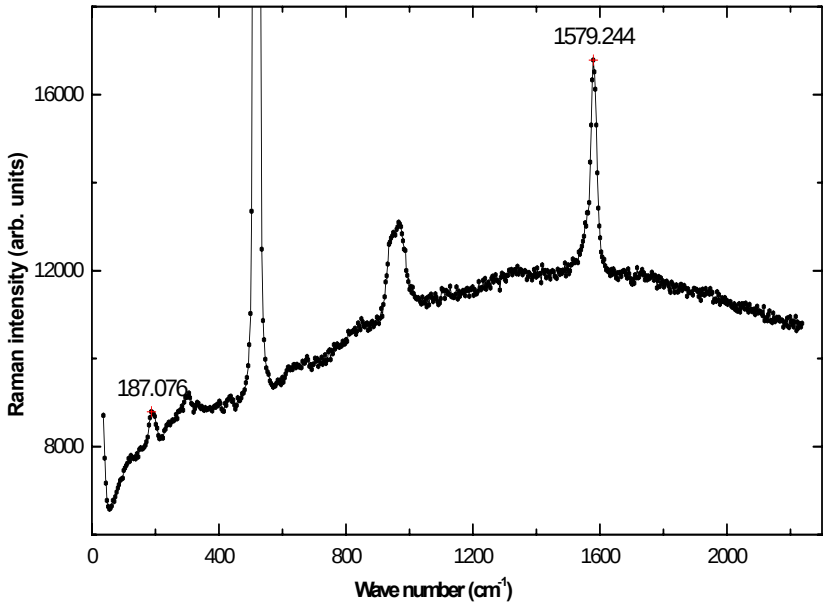

FIGURE 7.11 Raman spectrum of the SWCNTs on the inverse-opal Si substrate.

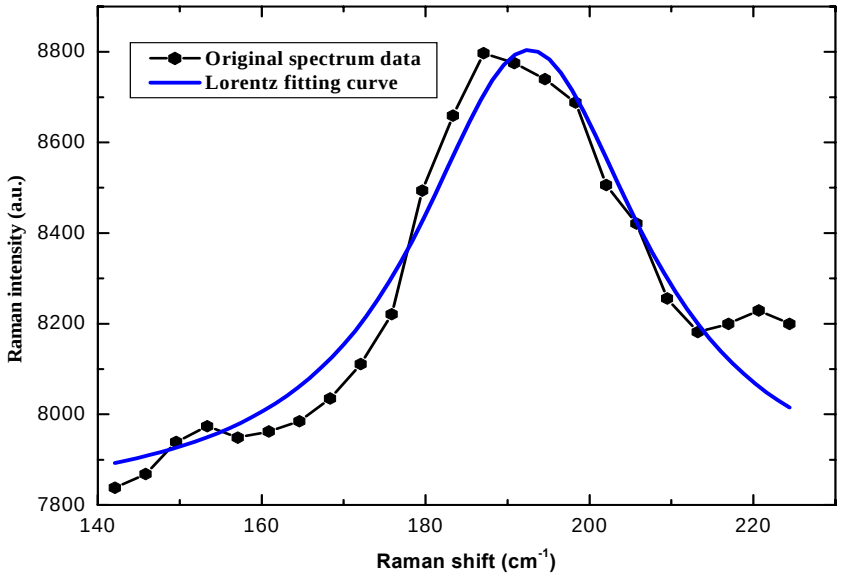

FIGURE 7.12 Lorentz fitting of the Raman spectrum in RBM band for the SWCNTs grown on the inverse-opal Si substrate.

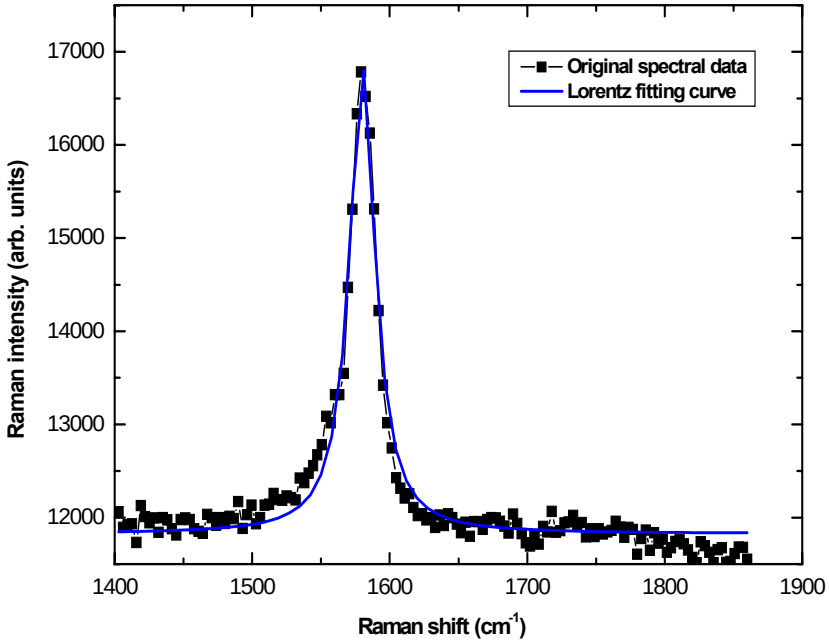

FIGURE 7.13 Lorentz fitting of the Raman spectrum in G band for the SWCNTs grown on the inverse-opal Si substrate.

7.3.3 Enhanced Raman spectra of SWCNTs by microparticles

Using the silica microparticles, the Raman scattering on the SWCNTs can be enhanced. As shown in Fig. 7.14, some SWCNTs (area B) are covered with particles (2.34 μm), while others (area A) are not. As a consequence, comparing the Raman intensity at a same peak allows us to find the influence of the nanojets generated by those microparticles. Figure 7.15 shows the Raman spectra from these two areas. The ERI in this case is 3, indicating that the significant impact of the microparticles on the Raman enhancement.

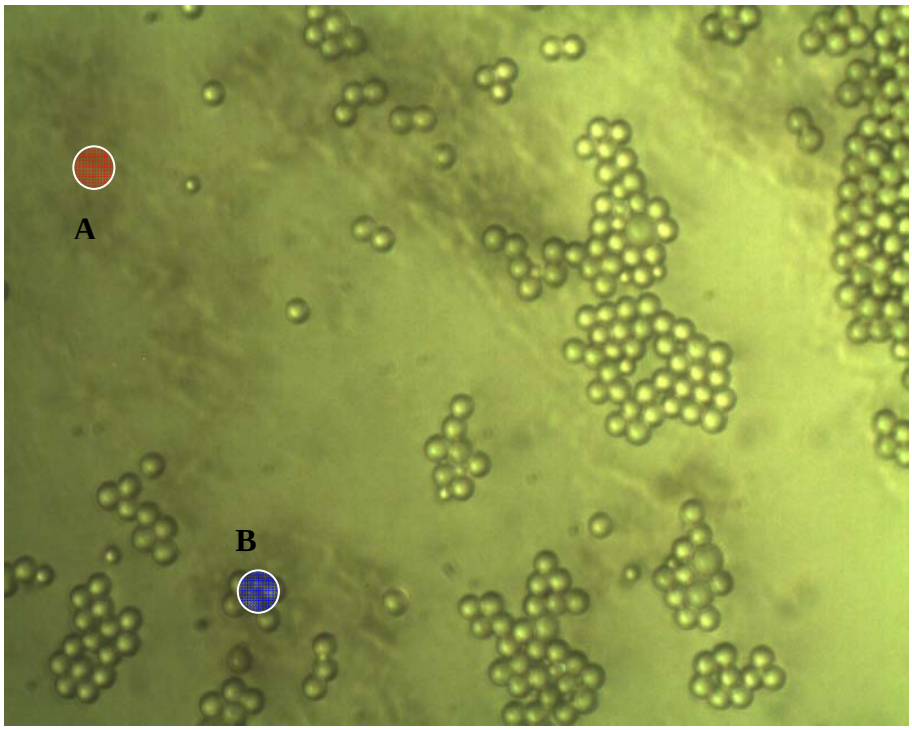

FIGURE 7.14 Images of the SWCNTs covered with self-assembled silica microparticles.

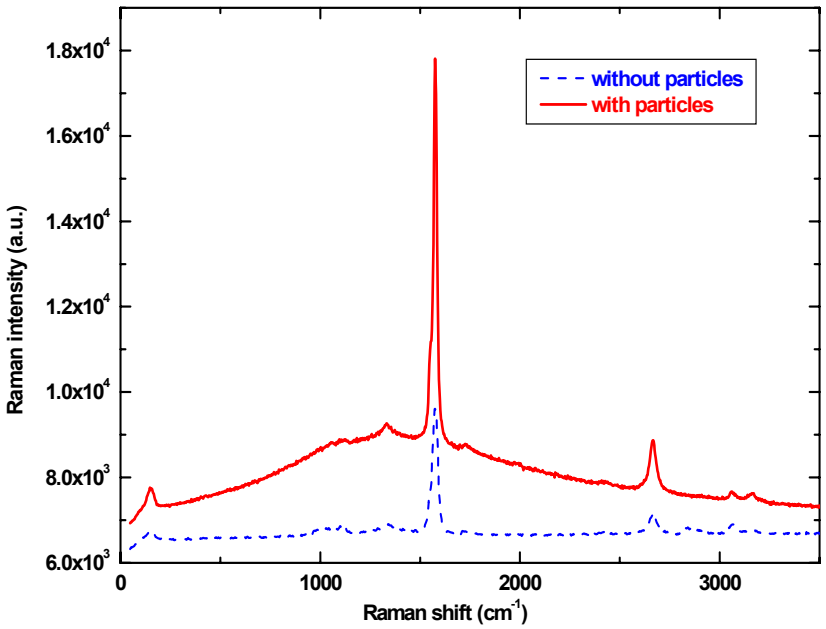

FIGURE 7.15 Raman spectra of the SWCNTs from areas A (without particles) and area B (with particles).

7.4 Raman characterization of SWCNTs at nanometer scales

7.4.1Tip-enhanced Raman spectra of SWCNTs

By applying the tip-enhanced Raman spectrometer, the Raman spectra of the individual SWCNTs dispersed on the Si substrate were obtained by measuring the Raman spectra with (near-field and far-field) and without (far-field only) the tip. With a good alignment, the Raman enhancement for all vibration modes (RBM, D, G and G') can be found, as shown in Fig. 7.16. This enhancement has a contrast ratio of about 180% for the G-band. The Raman peak of the silicon substrate was observed, but not enhanced, because the tip was exactly placed above the SWCNTs, and thus the enhanced optical fields only enhanced the Raman signal of the SWCNTs but not of the substrate.

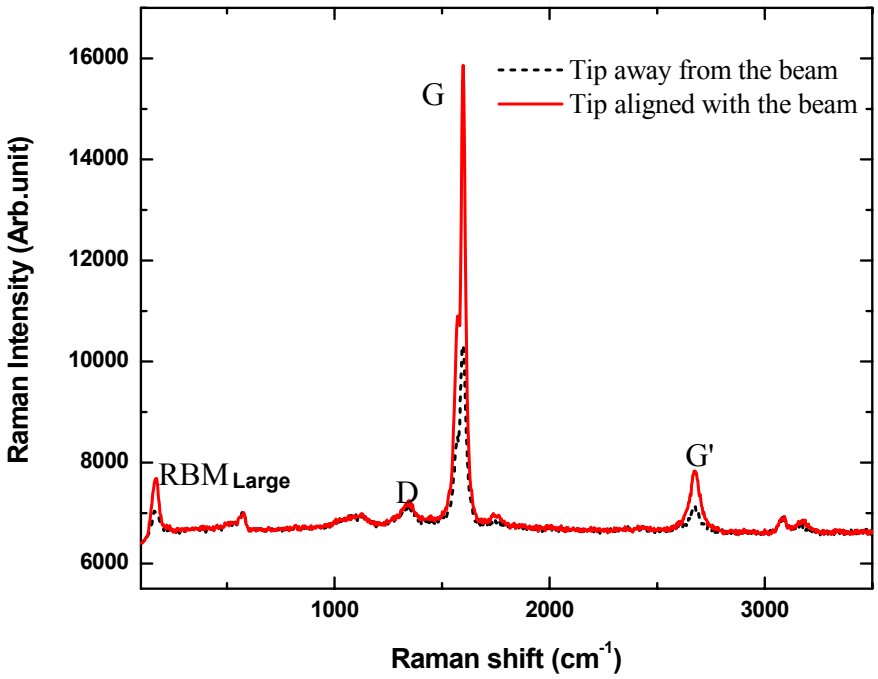

FIGURE 7.16 Raman spectra of the SWCNT with the tip away from (dotted curve) and aligned with (solid curve) the laser beam.

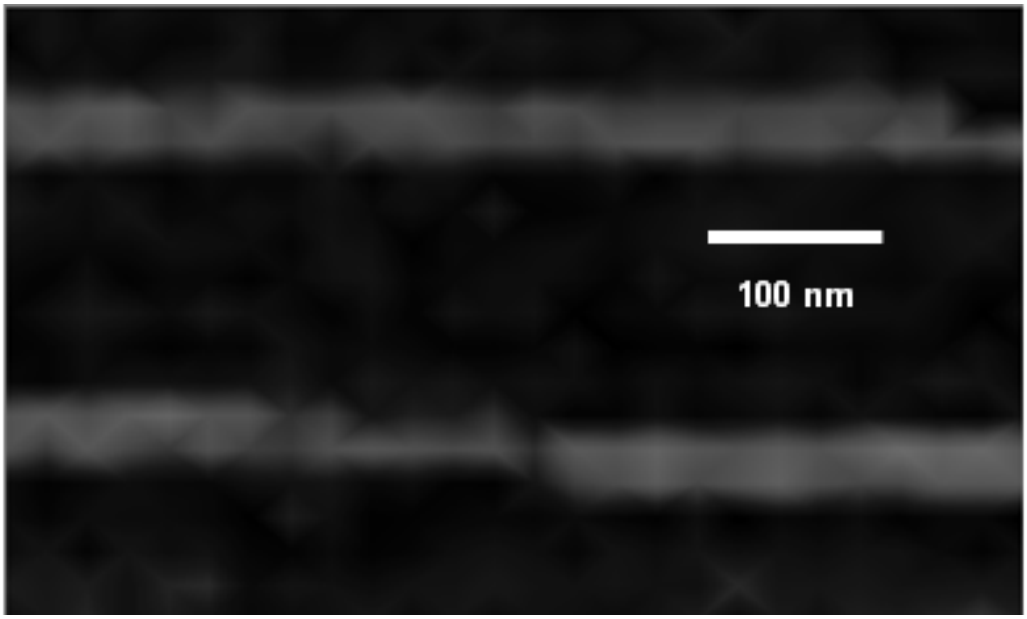

FIGURE 7.17 Raman mapping of the individual SWCNTs dispersed on the Si substrate.

7.4.2 Raman mapping of individual SWCNT

By identifying different Raman intensities from different region using a specific vibration mode as the fingerprint, Raman mapping can be performed to visualize the individual carbon nanotubes. Figure 7.17 shows the Raman image of the SWCNTs dispersed on the Si substrate. As evidenced by the images, this instrument has a spatial resolution of 30 nm.

7.5 Conclusion

In this chapter, using the micro-Raman and the tip-enhanced Raman spectrometers, we measured the SWCNT samples on the Si substrates prepared using the LCVD and solution dispersion. Their properties were studies in both microscale and nanoscale. The Raman peaks of different bands, including the RBM, D, G and G´ bands, were obtained and analyzed. By using the relationship between the tube diameter and the peak position of the RBM band, the diameters of those nanotubes were estimated to be 1.33 nm. The Raman mapping of the SWCNTs at microscales and nanoscales was performed. The successful mapping of the individual SWCNTs using the tip-enhanced Raman spectrometer demonstrates that this apparatus has a spatial resolution of 30 nm. In addition, by applying the microparticles-enhanced Raman spectroscopy, the Raman intensities of the SWCNTs were significantly enhanced.

CHAPTER 8 FABRICATION OF NANOSTRUCTURES WITH HIGH ELECTRICAL CONDUCTIVITY ON SILICON SUBSTRATES USING A LASER-ASSISTED SCANNING TUNNELING MICROSCOPE

8.1 Introduction

The past decade has seen an unprecedented rapid growth of nanoscience research and engineering. Modern manufacturing industries, particularly for the fabrication of integrated circuit at nanoscales (i.e., nanoelectronics), demands innovative approaches to fabricate nanostructures, which are critical parts of quantum-effect devices for future highly integrated circuit building blocks [1]. The Scanning Tunneling Microscope (STM), traditionally as an indispensable tool for ultrahigh-resolution imaging of surfaces morphology/structures and measurement of surface electronic structures, has offered possibilities to locally manipulate and modify material surfaces in nanometer or even atomic scales by using various STM interactions as contact forces, electrical fields, and electron beam induced effects or even a combination of these interaction mechanisms [2-8]. The Laser-Assisted STM (LASTM), in which external energy is injected into the tip–substrate gap with laser radiation, is an alternative approach to perform surface nanostructuring and atomic manipulation. It has several advantages over STM-only counterpart such as versatile material processing and correlated property characterization [9-17]. This technique, stemming from the tip-enhanced RS, employs a focused laser radiation at the tip apex. A local intensity enhancement of optical radiation near the tip apex with the resolution much beyond the optical diffraction can be achieved. The field enhancement is mainly explained by a combination of classical electrostatic lightning rod and surface plasmon excitation effects [18-21]. Till present, nanostructures with low electrical conductivity, e.g. nanooxidization of Si as an energy barrier, have been intensively investigated using the LASTM. In contrast, however, the fabrication of nanostructures with high electrical conductivity using this method has not been fully

investigated. The application of the LASTM to surface nanostructuring which will ultimately be utilized in micro or nanoelectronics industry involves the completely understanding their electronic properties, which can be characterized using the scanning tunneling spectroscopy (STS) [22-25].

A few nanostructures, such as nanoscales dots and lines, with high electrical conductivity on p-type hydrogen-passivated Si (110) surfaces were fabricated using the LASTM. Their surface morphologies were characterized *in-situ* using the STM, and their electronic properties were characterized using the STS. The dependence of the nanostructure geometries on the energy and number of the pulsed laser was investigated.

8.2 Experimental details

The experimental steps include the preparation of the hydrogen-passivated Si substrates, the fabrication of W tips, the processing of the nanostructures on the as-prepared Si substrates, and the characterization of the fabricated nanostructures.

The p-type Si (110) substrates (Virginia Semiconductor) with a resistivity of 0.02-0.09 Ωcm were cleaned using an ultrasonic cleaner with acetone and alcohol solutions for 10 min, followed by a passivation process in a 5% HF solution for 5 min. The substrates were then dried with a nitrogen gas. Subsequently, they were stored in an acetone-filled container to avoid the surface oxidization.

The W tips were fabricated from a W wire with a diameter of 0.25 mm using an electrochemical (EC) etching system with a DC current. The tip geometries were characterized by a field-emission Scanning Electron Microscope (SEM, Hitachi S-4700). The tips with different geometries could be prepared by tuning the position of the wire

immersed in the electrolyte, for which a precise control over the length of tips is required due to the surface tension between the tip surface and the electrolyte.

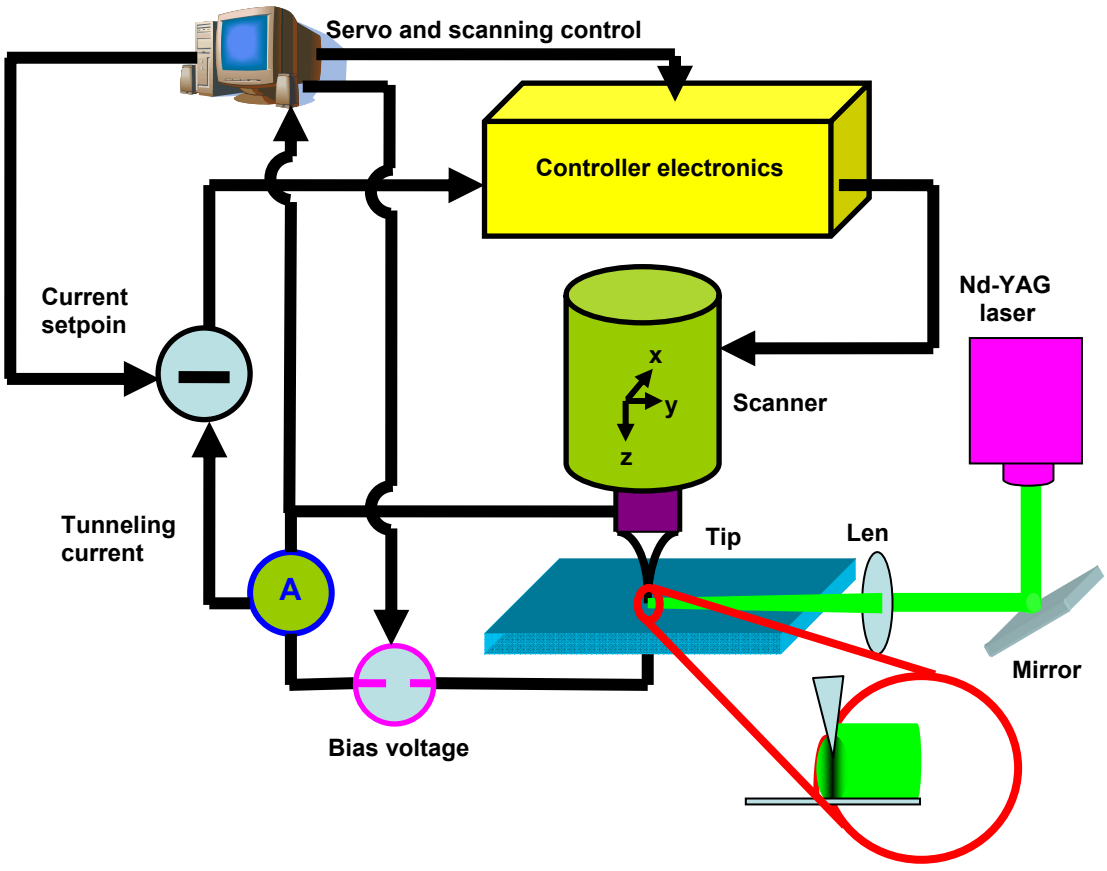

FIGURE 8.1 Experimental setup of LASTM used for surface nanostructuring.

The schematic diagram of the experimental setup for surface nanostructuring using the LASTM is shown in Fig. 8.1. The setup is composed of an STM (Agilent, PicoPlus 5), a Q-switched pulsed Nd-YAG laser with a pulse width of 7 ns and a wavelength of 532 nm, and optics for delivering the laser beam. The STM can operate both in open loop and close loop modes by changing different scanners. An on-axis optical microscope equipped with a CCD camera provides a zoomed view of the

substrate surfaces for the beam alignment on the tip apex. The focused laser beam is delivered to the tip-surface gap from the front side of the probe head.

The alignment of the laser beam was performed under the optical microscope by observing the diffraction light from the tip. To make sure that the nanostructure was induced only from the near-field effects of the tip, the incident laser beam was adjusted to be completely perpendicular to the tip axis or in parallel with the sample surface. The STM scanner was placed in a transparent environment chamber to effectively suppress environmental noises. To perform the nanofabrication, laser pulses were applied while the tip-surface distance was within the tunneling range. The incident laser beam was focused before reaching the tip-surface gap. The STM was kept in the constant-current mode with a tunneling current of 3 nA for the fabrication and the imaging. The surface morphology was characterized *in-situ* with the laser off. The STS was performed to measure the current-voltage (*I-V*) characteristics from which the differential conductance was derived.

8.3 Tip fabrication

The fabricated W tips with curvature radii varying from 10 nm to 50 nm were fabricated using the EC etching method are shown in Fig. 8.2, being numbered 1 to 5. Those tips have different curvature radius, aspect ratio and length. The SEM micrographs of the tips 3 and 5 shown in Fig. 8.2 in normal view are presented in Fig. 8.3(a) and 8.3(c), respectively, and their zoomed views are shown in Fig. 8.3(b) and 8.3(d), respectively.

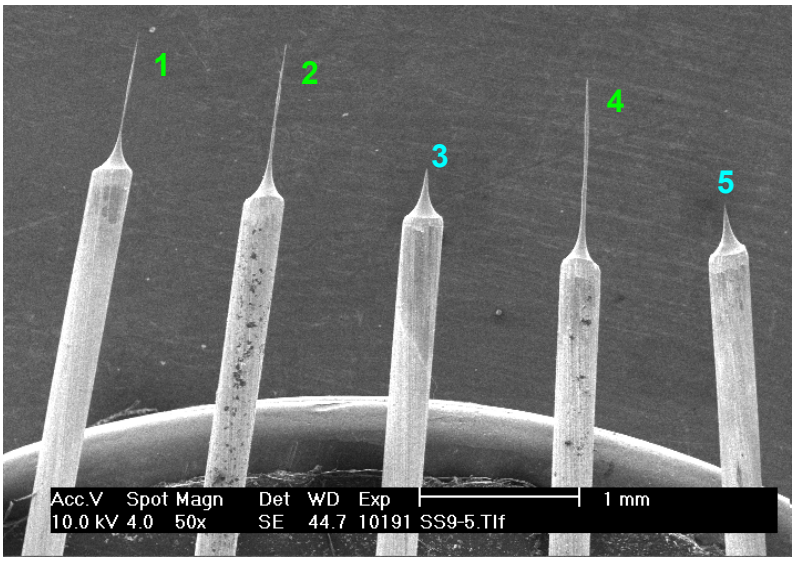

FIGURE 8.2 SEM micrographs of the fabricated W tips with different geometries.

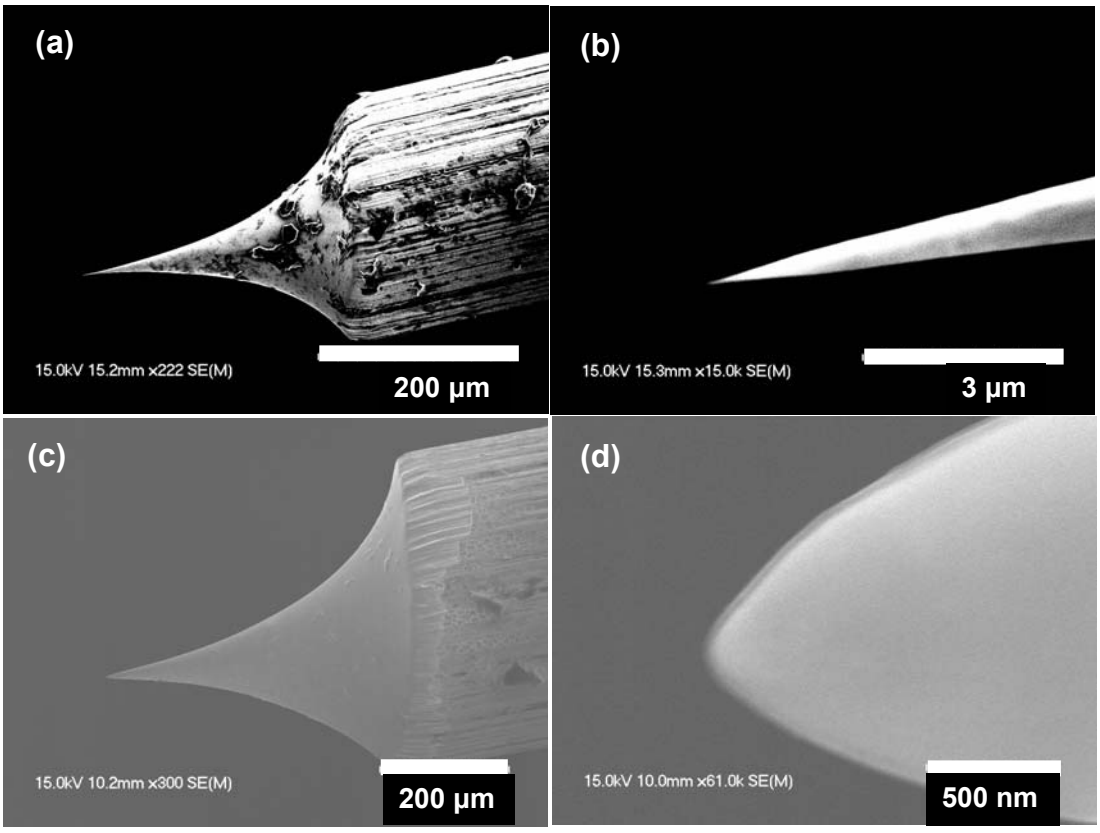

FIGURE 8.3 SEM micrographs of (a) the normal view, (b) the zoomed view of the tip 3; (c) the normal view and (d) the zoomed view of the tip 5.

8.4 Impact of laser fluence and number of pulse on nanostructures

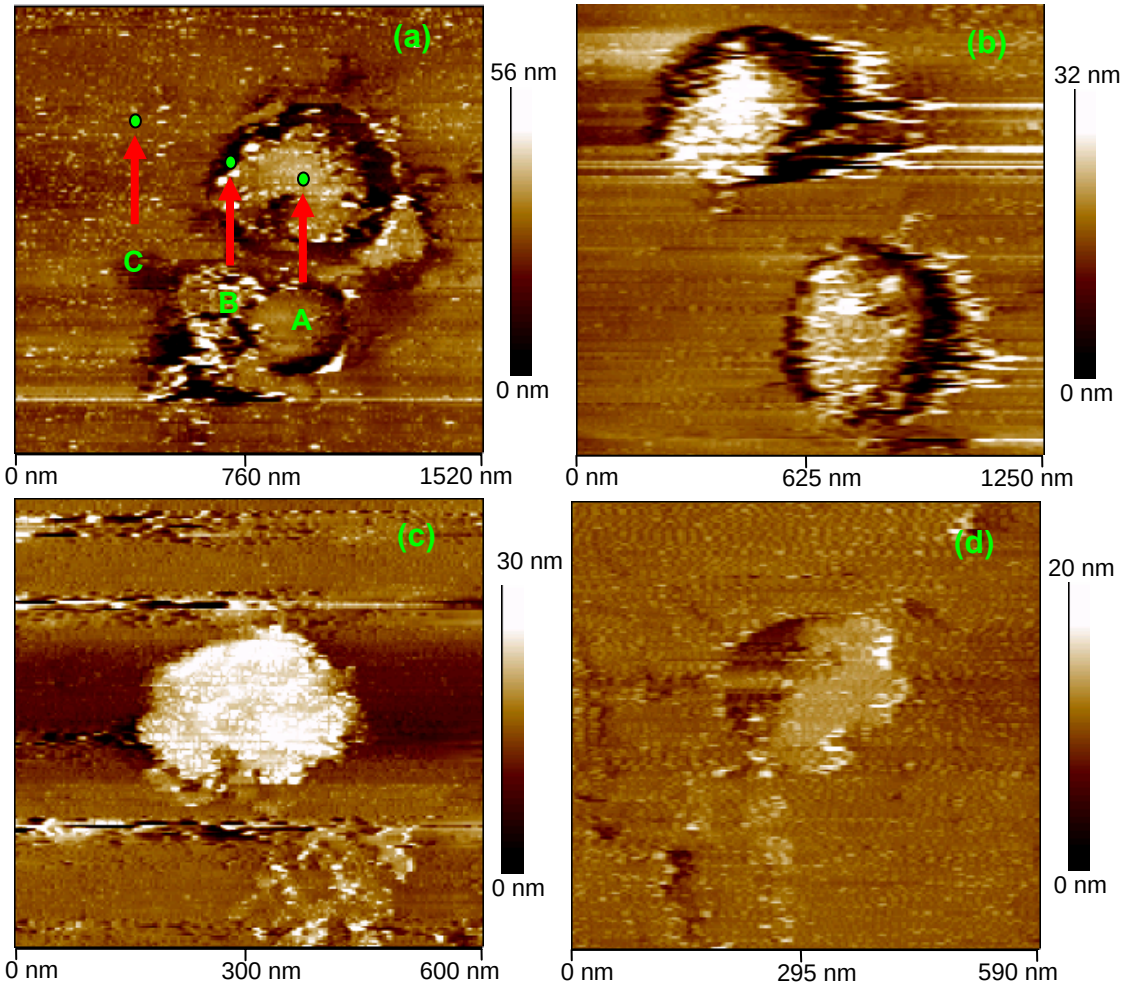

FIGURE 8.4 STM images of the nanostructures fabricated with different pulse numbers of (a) 15, (b) 10, (c) 5, and (d) 3. (laser energy = 15 mJ, gap voltage = 1 V, tunneling current = 3 nA).

The pulse energy, the number of the pulses, and the tip-surface distance strongly affect the formation of the nanostructures and their geometries. By adjusting these parameters, the nanostructures with different feature sizes (dot diameter or line width) and heights were fabricated. Figure 8.4 shows the STM images of the nanostructures fabricated using four different numbers of pulses (15, 10, 5, and 3) under the same condition of a pulse energy of 15 mJ, a gap voltage of 1 V, and a tunneling current of 3 nA. Figure 8.4(a)

shows two dots fabricated with 15 and Fig. 8.4(b) shows two dots fabricated with 10 pulses. Figures 8.4(c) and 8.4(d) show two dots fabricated with 5 and 3 pulses, respectively. It can be observed that these nanostructures have approximately circular shapes, due to the circular beam profile of the enhanced laser determined by the geometry of the W tip. The brighter regions in the figures correspond to the regions which have higher electrical conductivities, or more precisely, higher tunneling probabilities. Therefore, the electronic properties of the fabricated structures are totally different from the Si substrate.

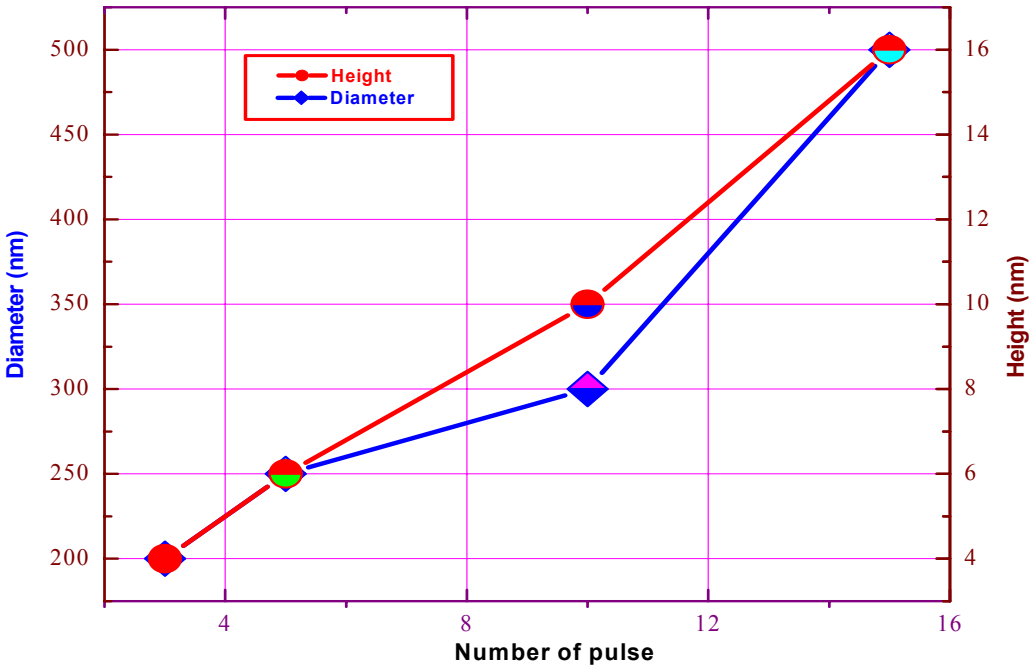

FIGURE 8.5 Nanostructure diameter (diamonds) and height (circles) as functions of number of pulses. (pulse energy = 15 mJ, gap voltage = 1 V, tunneling current = 3 nA).

The dependences of the diameters and the heights of the nanostructures in Fig. 8.4 on the number of the pulses are shown in Fig. 8.5. It can be seen that the diameters and

heights increase almost linearly with the increasing number of pulses. The diameters of the nanostructure are in the range from 200 to 500 nm, and their heights range from 4 to 16 nm, when the number of the pulse is in the range of 3 and 15.

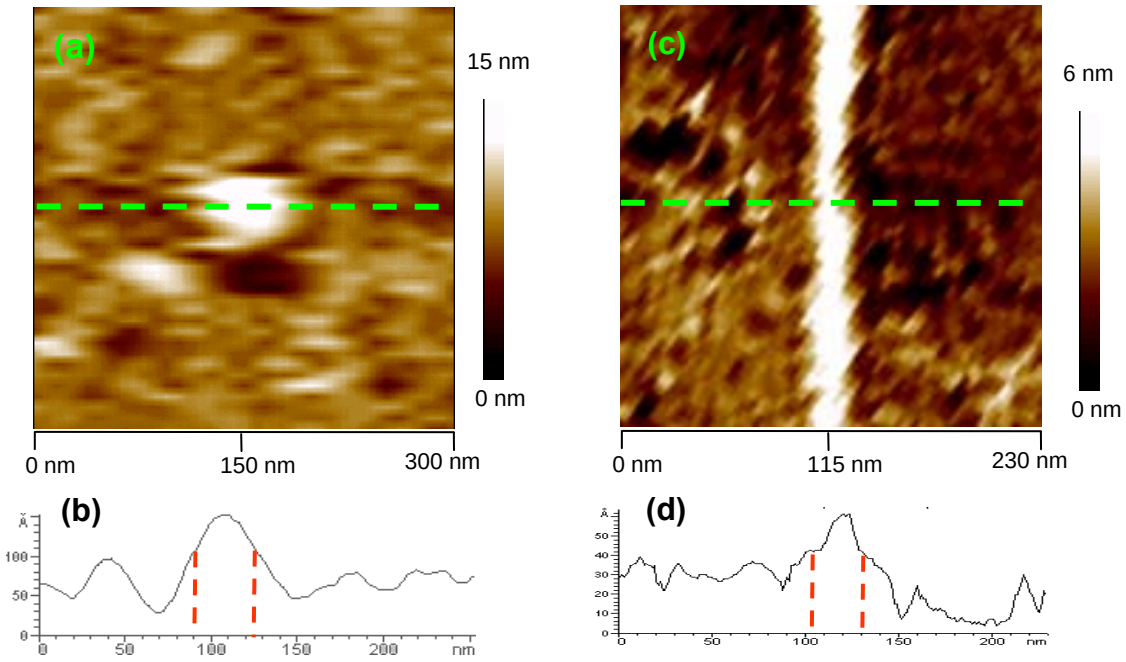

FIGURE 8.6 (a) STM image of a dot with a diameter of 30 nm, (b) profile along the line indicated in (a), (c) STM image of a line with a width of 30 nm, and (d) profile along the line indicated in (c). (gap voltage = 0.1 V, tunneling current = 3 nA).

In order to fabricate smaller nanostructures, more tightly focused and more highly enhanced optical field is required by tuning the gap voltage while keeping the same tunneling current. Different gap voltages (0.01, 0.1, and 1 V) and pulse energies (2, 5, and 10 mJ) at a constant current of 3 nA were utilized to fabricate smaller dots. As illustrated in Fig. 8.6(a), a dot with a diameter of 30 nm was fabricated when the gap voltage and pulse energy were 0.1 V and 5 mJ, respectively. A single line, as shown in Fig. 8.6(b), was also fabricated by scanning the STM tip on the Si surface at a speed of 10 nm per second while other conditions remained the same as those used in the fabrication of the 30-nm dot. This line has an average width of approximately 30 nm.

8.5 Characterization of nanostructures using scanning tunneling spectroscopy

The STS provides the vital information about the local density of states (LDOS) on the surfaces at atomic or molecular scales [26]. The H-passivated Si surfaces show an ideal surface electronic structure with a low surface state density [27]. The absence of surface states and the Fermi level pinning enables direct observation of the Schottky barrier behavior. The *I-V* curve of the p-type Si surfaces indicates a typical Schottky behavior, exponentially in the forward bias and lower current for reverse bias. As the substrate voltage is tuned more positive, the conduction band moves up and more current will flow. In the reverse direction, as the voltage becomes more negative, the bands bend down and increase the potential barrier to the holes.

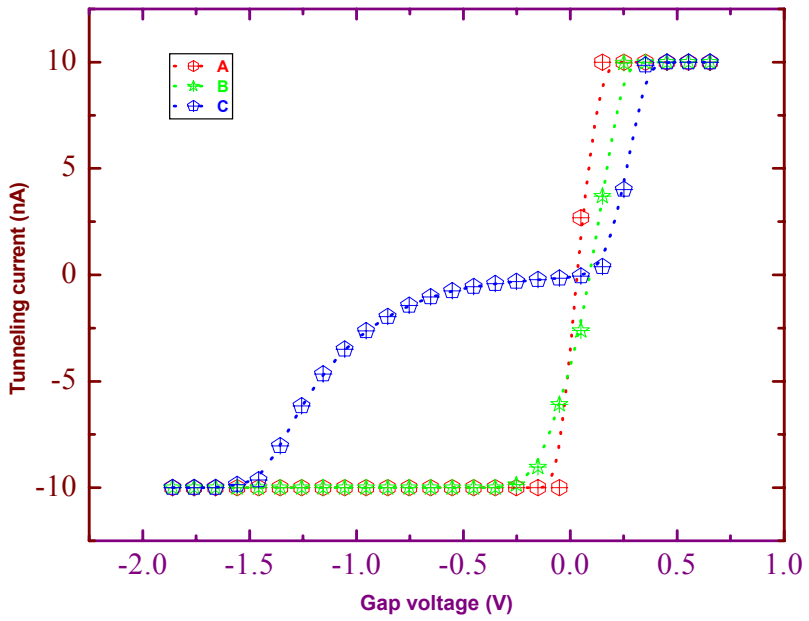

FIGURE 8.7 *I-V* characteristics as a function of gap voltage at points A, B, and C indicated in Fig. 8.4(a).

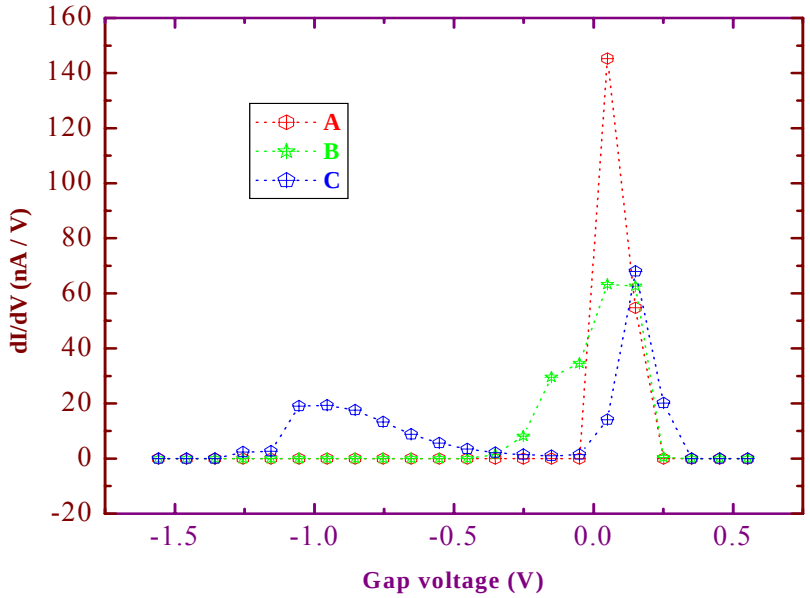

FIGURE 8.8 Differential conductance *dI/dV* as a function of gap voltage at points A, B, and C indicated in Fig. 8.4(a).

The STS was performed in different regions *in-situ* after the nanostructuring. The tunneling currents as functions of the gap voltage at points A, B, and C indicated in Fig. 8.4(a) are shown in Fig. 8.7. It can be seen that the *I-V* characteristics are different at different regions. In the region far from the fabricated dot (curve C), a typical Schottky barrier behavior can be observed. At the edge of the dot (curve B), the tip-surface gap still demonstrates a Schottky behavior but with increased tunneling probability. Inside the dot (curve A), no obvious Schottky behavior can be seen. Furthermore, the curve becomes more symmetric and band bending disappears. The band gap can be estimated from the differential conductivity as a function of gap voltage, as shown in Fig. 8.8. For the hydrogen-passivated surface without laser processing, the band gap is around 1.1 eV, which is a typical value for Si. The band gap of the Si surface decreases when the probe

point approaches the dot, and almost diminishes inside the dot, indicating the tendency of electronic structure change.

The difference between the tip work function and the semiconductor electrode affinity results in the formation of a Schottky barrier. The conduction between the tip and the semiconductor surface involves thermionic emission of electrons over the barrier followed by tunneling of electrons through the vacuum barrier to the metal tip. An increasing positive sample bias on p-type Si decrease the band banding, lowering the Schottky barrier and enhancing electron emission [28].

8.6 Mechanism investigation of surface nanostructuring on Si substrates

When the gap voltage is lower than both the work functions of the W tip and the p-type Si, the nanostructures with different differential conductance may arise from the surface states. These surface states are primarily associated with the critical points in the surface-projected bulk band structures or the surface dangling bonds. The mechanisms of the nanostructure fabrication on the Si surfaces using the LASTM might involve two individual steps: 1) the hydrogen atoms adsorbed on the Si surface for the passivation are thermally desorbed by the highly localized optical field, resulting in a clean and intrinsic Si surface; 2) the dehydrogenized surface is further turned into the more conductive poly-Si through the thermal process by the enhanced field. Therefore, the local temperature is of crucial importance in both steps. To better understand the mechanisms, a study of the temperature rising underneath the tip apex is necessary. It is assumed that the incident laser beam propagates in parallel with the sample surface. When a Gaussian distribution is used to describe the beam profile, the steady-state temperature on the Si surface underneath the W tip induced by a pulsed laser can be expressed by [13]

$$T_{\max} = \frac{\sqrt{\pi}\alpha F(1-R_0)w_0}{8\kappa_T \tau}. \quad (8.1)$$

Here, $T_{\max}$ is the maximum temperature on the Si surface underneath the tip apex, α is the optical enhancement factor defined as the ratio of the enhanced electric field to the original electric field of the incident pulsed laser, F is the laser fluence, R_0 is the optical reflectance of the Si surface at the normal incidence, w_0 is the diameter of the tip apex, κ_T is the thermal conductivity of the Si, and τ is the laser pulse duration. Obviously, the temperature induced by the LA-STM is proportional to the laser intensity F/τ, the optical enhancement factor, α and the tip radius. The laser wavelength also affects the temperature because the optical reflectance is a function of the laser wavelength. In order to increase the transient local temperature, we can use a pulsed laser with higher peak energy and a shorter pulse duration, or select a lower gap voltage to maintain a shorter tip-surface distance that can lead to an higher optical enhancement factor, or employ a tip with a smaller tip radius. The temperature was calculated using the parameters obtained both from the practical experimental conditions and the simulation results, which are R_0 = 0.37 at 532 nm, α = 220 at the gap distance of 1 nm, w_0 = 30 nm for the EC-etched W tip, and κ_T = 1.3 W.cm^{-1}°C^{-1}. For a pulsed laser with a pulse energy of 5 mJ and a pulse duration of 7 ns, the laser intensity F/τ was estimated as 30 mW.cm^{-2}. As a result, the temperature is calculated to be 1259 °C, corresponding to the temperature at which the 30 nm dot was fabricated. This temperature is a slightly lower than the melting point of Si (1412 °C). The threshold pulse energy to form a nanostructure was found to be 2 mJ. Using the same parameters given above, the threshold temperature was calculated to be

503 °C, below which neither the photochemical reaction for dehydrogenization nor the thermal process for the formation of poly-Si occurs. Hence, no nanostructure can be fabricated on the Si surface.

8.7 Conclusion

Nanoscale dots and lines with high electrical conductivity were fabricated on the p-type Si (110) substrate surfaces by LASTM. The feature sizes and heights are nearly linearly dependent on the number of the laser pulses in the studies range. A dot with a diameter of 30 nm was fabricated with pulse energy of 5 mJ, a gap voltage of 0.1 V, and a tunneling current of 3 nA. A line with a width of 30 nm was also fabricated at the tip scanning speed of 10 nm/s. The STS spectra indicate that their electronic structures were changed. The nanostructures are presumably poly-Si, which has a higher electrical conductivity than that of the intrinsic Si. The thermal effect induced by the enhanced optical field was successfully applied to explain the LASTM nanofabrication mechanism.

CHAPTER 9 SUMMARY AND OUTLOOK

The diffraction limit of the conventional optics prevents the laser technologies from being applied to the fabrication and characterization of the materials and devices in nanoscale. The main objective of this study was to explore the possibilities and extend the capabilities of the laser technologies to resolve this problem. The specific goals of this study were to develop novel optical characterization techniques and platforms with nanoscale resolutions, and fabricate nanostructures on semiconductor substrates like Si surfaces, based upon the near-field optics. This study was mainly focused on: 1) theoretically studying the optical near fields induced by the laser-tip and the laser-microparticles interactions, 2) practically developing a tip-enhanced Raman spectrometer and imaging system with nanoscale resolutions, 3) investigating the impact of the nanojets generated by the self-assembled silica microparticles on Raman enhancement, 4) improving the detection sensitivity of the tip-enhanced Raman spectroscopy by introducing metallic nanostructures, 5) examining the properties of the SWCNTs using the Raman spectra and the Raman imaging in nanoscale, and 6) fabricating nanostructures on Si substrates using a laser-assisted scanning tunneling microscope.

Using the Finite-Difference Time-Domain (FDTD) method and the Lorentz-Drude model, the theoretical calculations of the enhanced optical near fields induced by the microparticles, the metallic tips (Ag, W, and Au) and the combination of the Ag nanostructures with the Au tips were performed. The field enhancement by the nanoparticles, the metallic tips and the combination of the nanostructures and tips are based on the nanojets phonomena, the surface Plasmon resonant excitation and the coupling of the excited surface plasmons of the nanostructures and tips, respectively. The

polarization of the excitation light plays an important role in achieving a highly enhanced optical field when a metallic tip is used as the light enhancer. If the polarization is in parallel with the tip axis, a significantly enhanced optical field can be obtained in the proximity of the tip apex. On the contrary, if the polarization is perpendicular to the tip axis, no apparent enhancement can be observed. The presence of the substrate and the gap distance between the tip and the substrate also have significant impacts on the optical field. Those conclusions drawn from the simulations provide us a compass to design our experiments.

A practical Raman spectrometer and imaging system capable of working in both microscale and nanoscale was developed. Equipped with a back-illuminated CCD camera with an extremely high sensitivity and a notch filter with a high optical density at an excitation wavelength of 514.5 nm, this system allows us to characterize a variety of samples, such as diamond-like carbon films and individual single-walled carbon nanotubes, etc. Working in the microscale mode, it incorporates an optical microscope with several objectives with a maximum resolution of 1 μm. Working in the nanoscale mode, it includes a scanning tunneling microscope with a maximum resolution of 30 nm. The flexibility of the optical path permits us to perform a fast and reliable optical alignment through a special procedure which enables the laser beam to be well aligned with the tip apex. The optical alignment is critical to maximize the Raman enhancement. The software program for the Raman mapping was developed to study structured samples. The functionalities of the system were verified by measuring Si substrates. In addition, by applying the depolarization technique, the far-field signals on the Si substrates were significantly suppressed, giving rise to a high contrast ratio.

The Raman intensity of the Si substrates covered with self-assembled silica microparticles was enhanced by the nanojets generated at the backside of the microparticles in the light propagation direction. The maximum enhancement factor of 1.4×10^4 was obtained when the particles with diameters of 2.34 μm were used, which is in good agreement with the simulation results. This technique, with a resolution of around 100 nm or below, has potentials in a variety of applications, such as surface science, biology, chemistry, materials science and microelectronics.

Metallic nanostructures were used to further improve the Raman enhancement of the tip-enhanced Raman spectroscopy. The Ag nanostructures with a dipole distance of 100 nm were fabricated on Si substrates using the nanosphere lithography. If the STM tip and the nanostructures were properly aligned, the Raman signals were significantly enhanced. The enhancement factor was estimated to be 9.75×10^6, more than one order of magnitude higher than the enhancement factor obtained without the nanostructures, i.e., with the tip only. The simulation based on three tips model was in agreement with the experimental. The coupling of the LSPs from the STM tip and the nanostructure dipole explains the improved enhancement. The Raman imaging of the nanostructures revealed that this apparatus has a spatial resolution of 100 nm.

As a promising candidate to build future nanoelectronic devices to replace current Si-based microelectronic devices, the single-walled carbon nanotubes were investigated using the developed techniques and platforms. The nanotube samples were synthesized on both flat and inverse-opal Si substrates using the laser-assisted chemical vapor deposition and solution dispersion. The Raman peaks of the nanotubes at the RBM mode (181 cm^{-1}), the D mode (1350 cm^{-1}), the G mode (1591 cm^{-1}) and the G' mode (3090 cm^{-1})

were clearly observed. By applying the microparticles-enhanced technique, the Raman intensity of the nanotubes was enhanced 3 times higher. Using the tip-enhanced Raman spectrometer, two individual nanotubes were imaged, indicating that this instrument has a resolution of 30 nm.

Electronically active nanoscale dots and lines were fabricated on the p-type Si (110) substrates using the laser-assisted scanning tunneling microscope. Their feature sizes and heights are almost linearly dependent on the number of pulses. A dot with the diameter of 30 nm was fabricated with a laser fluence of 5 mJ, a gap voltage of 0.1 V, and a tunneling current of 3 nA. In addition, a line with the width of 30 nm was fabricated at the scanning speed of 10 nm/s. The STS spectra indicate that their electronic structures were changed. The nanostructures are presumably polysilicon, which has a higher tunneling probability than the intrinsic Si. The thermal effect induced by the highly localized optical field is used to explain the fabrication mechanism and is believed to be the major driving force of this nanofabrication technique.

The characterization and fabrication techniques and platforms demonstrated in this dissertation based on the near-field optics are far from maturity, and many aspects need to be improved. A few future research directions are outlined as the following:

(1) The tips are critical to achieve a stable and reliable Raman enhancement. According to our experiences, however, the fabrication yield of high quality tips that can be used to obtain the significant enhancement is very low. Tips with small apex diameters and high aspect ratios can achieve high Raman enhancement. Optimizing the etching conditions, including the etching time, the bias voltage, the immersion depths and the

chemical solutions might help to increase the fabrication yield of high quality tips. Using ion bombarding to tailor the tips might be another way to do so.

(2) The spatial resolution of the tip-enhanced Raman spectroscopy can be improved to a sub-10 nm scale by employing more advanced nanotips such as carbon nanotube probes. Recently, nanotube tips have been successfully used to achieve a nanodot on a piece of highly ordered pyrolytic graphite with a diameter of only 2 nm using a scanning tunneling microscope. The laser-assisted chemical vapor deposition method developed in our group might be an ideal approach to fabricate the nanotubes near the tip apex with the localized heating. By controlling the diameter of the nanotubes, various spatial resolutions could be achieved. The successful development of this technique will provide a powerful tool for studying nanostructures with feature sizes of sub-10 nm, such as biological proteins and semiconductor quantum structures.

(3) Since the tip enhanced Raman spectrometer and the laser-assisted scanning tunneling microscope share the same scanning tunneling microscope, and are all based on the localized and enhanced optical field induced by the metallic tips, they can be integrated together to achieve more powerful functions and perform more complicated tasks. The successful integration will pave the way for the systematic *in-situ* study of the nanostructures fabricated by the laser-assisted scanning tunneling microscope, including their topologic, electronic, physical, chemical, and thermal properties in nanoscale or even atomic scale. For example, it can be used to understand the formation mechanism of the individual nanostructures by investigating the location, extension, and intensity of the residual strains and the sub-surface structural damages through charactering the topology

and the electronic density of states using the scanning tunneling spectroscopy and through characterizing the Raman spectra using the tip-enhanced Raman spectrometer.

(4) The writing speed of the surface nanostructuring using the laser-assisted scanning tunneling microscope is extremely low, which is detrimental for this technique to be widely accepted. The main reason of the low speed is that only one tip can operate at a time. Similar to the Millipede developed in IBM, the technique using multiple tips may be a good solution to solve this problem.

(5) In combination with a tunable laser and a multistage spectrometer, the tip-enhanced Raman spectrometer can be used to achieve higher Raman enhancement by tuning the laser to the resonance frequency of the tip. One exciting application of this system is that by identifying the resonance frequencies of individual single-walled carbon tubes, thus the unwanted tubes with specific chiralities can be selectively removed.

(6) The feasibility of the depolarization technique to suppress far-field signals is only limited to the samples with asymmetric vibrations. It is inadequate for those with symmetric vibrations. Therefore, finding an alternative way to block the far-field signals from the samples with symmetric vibrations is another challenge.

(7) There is still plenty of room for further improving the Raman enhancement using metallic nanostructures. For example, we can optimize the materials and geometries of the tips, the materials and geometries of the nanostructures, the dipole distance, the tip-dipole distance and the incident angles of the excitation beam to achieve higher enhancement factors.

REFERENCES

Chapter 1

[1] C. Molpeceres, S. Lauzurica, J. L. Ocana, J. J. Gandia, L. Urbina and J. Carabe, "Microprocessing of ITO and a-Si thin films using ns laser sources", *J. Micromech. Microeng.* 15, 1271-1278 (2005).

[2] J. W. Kim, D. Y. Jeong, M. S. Kim, C. S. Kang, J. A. Kim and T. B. Eom, "A 50 m laser interferometer for automatic calibration of surveying tapes using wireless communication", *Meas. Sci. Technol.*, 19, 017003 (2008).

[3] J. Y. Fang, C. H. Tien, H. P. D. Shieh, P. Herget, J. A. Bain and T. E. Schlesinger, "Optical feedback height control system using laser diode sensor for near-field data storage applications", *J. Lightwave Technol.*, 25, 3704-3709 (2007).

[4] E. A. Sherr, "Laser induced scatter and fluorescence for ocular diagnosis of Alzheimer's disease: System evaluation", *Laser Surg. Med.*, 3-3 (2008).

[5] M. Fritze, J. Burns, P. W. Wyatt, C. K. Chen, P. Gouker, C. L. Chen, C. Keast, D. Astolfi, D. Yost, D. Preble, A. Curtis, P. Davis, S. Cann, S. Deneault and H. Y. Liu, "Sub-100 nm silicon on insulator complimentary metal-oxide semiconductor transistors by deep ultraviolet optical lithography", *J. Vac. Sci. Technol. B*, 18, 2886-2890 (2000).

[6] B. Cui, L. Wu and S. Y. Chou, "Fabrication of high aspect ratio metal nanotips by nanosecond pulse laser melting", *Nanotechnology*, 19, 345303 (2008).

[7] D. A. Rusak, K. D. Weaver and B. L. Taroli, "Laser-induced breakdown Spectroscopy for analysis of chemically etched polytetrafluoroethylene", *Appl. Spectrosc.*, 62, 773-777 (2008).

[8] D. W. Pohl, "Optics at the nanometre scale", *Philos. T. Roy. Soc. A*, 362, 701-717 (2004).

[9] D. H. Lowndes, "Nanotechnology overview", *Adv. Mater. Process*, 157, 48-51 (2000).

[10] A. Lewis, H. Taha, A. Strinkovski, A. Manevitch, A. Khatchatouriants, R. Dekhter and E. Ammann, "Near-field optics: from subwavelength illumination to nanometric shadowing", *Nat. Biotechnol.*, 21, 1377-1386 (2003).

[11] D. W. Pohl and L. Novotny, "Near-Field Optics - Light for the World of Nano", *J. Vac. Sci. Technol. B*, 12, 1441-1446 (1994).

[12] D. Richards, "Near-field microscopy: throwing light on the nanoworld", *Philos. T. Roy. Soc. A*, 361, 2843-2857 (2003).

[13] M. A. Poggi, E. D. Gadsby, L. A. Bottomley, W. P. King, E. Oroudjev and H. Hansma, "Scanning probe microscopy", *Anal. Chem.*, 76, 3429-3443 (2004).

[14] A. Hartschuh, M. R. Beversluis, A. Bouhelier and L. Novotny, "Tip-enhanced optical spectroscopy", *Philos. T. Roy. Soc. A*, 362, 807-819 (2004).

[15] L. Gomez, R. Bachelot, A. Bouhelier, G. P. Wiederrecht, S. H. Chang, S. K. Gray, F. Hua, S. Jeon, J. A. Rogers, M. E. Castro, S. Blaize, I. Stefanon, G. Lerondel and P. Royer, "Apertureless scanning near-field optical microscopy: a comparison between homodyne and heterodyne approaches", *J. Opt. Soc. Am. B*, 23, 823-833 (2006).

[16] B. Hecht, B. Sick, U. P. Wild, V. Deckert, R. Zenobi, O. J. F. Martin and D. W. Pohl, "Scanning near-field optical microscopy with aperture probes: Fundamentals and applications", *J. Chem. Phys.*, 112, 7761-7774 (2000).

Chapter 2

[1] H. J. Guntherodt and W. Meier, "Nanoscience and nanotechnology", *Chimia*, 56, 483-483 (2002).

[2] T. Sugii, "High-performance bulk CMOS technology for 65/45 nm nodes", *Solid State Electron.*, 50, 2-9 (2006).

[3] N. Tamura and Y. Shimamune, "45 nm CMOS technology with low temperature selective epitaxy of SiGe", *Appl. Surf. Sci.*, 254, 6067-6071 (2008).

[4] C. Z. Wang, Y. H. Rong and T. Y. Hsu, "Designs of higher tunnelling giant magnetoresistance in granular films", *Mater. Lett.*, 60, 379-382 (2006).

[5] Z. P. Niu, Z. B. Feng, J. Yang and D. Y. Xing, "Tunneling magnetoresistance of double-barrier magnetic tunnel junctions in sequential and coherent regimes", *Phys. Rev. B*, 73, 014432 (2006).

[6] M. Chen, S. Yamamuro, D. Farrell and S. A. Majetich, "Gold-coated iron nanoparticles for biomedical applications", *J. Appl. Phys.*, 93, 7551-7553 (2003).

[7] P. Eaton, G. Doria, E. Pereira, P. V. Baptista and R. Franco, "Imaging gold nanoparticles for DNA sequence recognition in biomedical applications", *Ieee T. Nanobiosci.*, 6, 282-288 (2007).

[8] D. J. Schulte, "Nanotechnology in environmental protection and pollution sustainable future, environmental cleanup and energy solutions", *Sci. Technol. Adv. Mat.*, 8, 11-11 (2007).

[9] C. G. Smith, "Low-dimensional quantum devices", *Rep. Prog. Phys.*, 59, 235-282 (1996).

[10] R. Tsu, "Applying the insight into superlattices and quantum wells for nanostructures: Low-dimensional structures and devices", *Microelectron. J.*, 38, 959-1012 (2007).

[11] B. Babic, M. Iqbal and C. Schonenberger, "Ambipolar field-effect transistor on as-grown single-wall carbon nanotubes", *Nanotechnology*, 14, 327-331 (2003).

[12] H. Watanabe, C. Manabe, T. Shigematsu, K. Shimotani and M. Shimizu, "Single molecule DNA device measured with triple-probe atomic force microscope", *Appl. Phys. Lett.*, 79, 2462-2464 (2001).

[13] M. A. Poggi, E. D. Gadsby, L. A. Bottomley, W. P. King, E. Oroudjev and H. Hansma, "Scanning probe microscopy", *Anal. Chem.*, 76, 3429-3443 (2004).

[14] N. P. Kobayashi, T. R. Ramachandran, P. Chen and A. Madhukar, "In situ, atomic force microscope studies of the evolution of InAs three-dimensional islands on GaAs(001)", *Appl. Phys. Lett.*, 68, 3299-3301 (1996).

[15] M. Moskovits, "Surface-enhanced Raman spectroscopy: a brief perspective", *Top Appl. Phys.*, 103, 1-17 (2006).

[16] P. Avouris, T. Hertel and R. Martel, "Atomic force microscope tip-induced local oxidation of silicon: Kinetics, mechanism, and nanofabrication", *Appl. Phys. Lett.*, 71, 285-287 (1997).

[17] D. W. Pohl, "Optics at the nanometre scale", *Philos. T. Roy. Soc. A*, 362, 701-717 (2004).

[18] B. Hecht, B. Sick, U. P. Wild, V. Deckert, R. Zenobi, O. J. F. Martin and D. W. Pohl, "Scanning near-field optical microscopy with aperture probes: Fundamentals and applications", *J. Chem. Phys.*, 112, 7761-7774 (2000).

[19] A. Bouhelier, "Field-enhanced scanning near-field optical microscopy", *Microsc. Res. Techniq.*, 69, 563-579 (2006).

[20] M. A. Paesler and P. J. Moyer, "Near-field optics: Theory, Instrumentation, and Applications", New York: Wiley (1996).

[21] D. W. Pohl, W. Denk and M. Lanz, "Optical stethoscopy: Image recording with resolution lambda/20", *Appl. Phys. Lett.*, 44, 651-653 (1984).

[22] D. W. Pohl and L. Novotny, "Near-Field Optics - Light for the World of Nano", *J. Vac. Sci. Technol. B*, 12, 1441-1446 (1994).

[23] A. Harootunian, E. Betzig, M. Isaacson and A. Lewis, "Super-resolution fluorescence nearfield scanning optical microscopy." *Appl. Phys. Lett.*, 674-676 (1986).

[24] E. Betzig, J. K. Trautman, T. D. Harris, J. S. Weiner and R. L. Kostelak, "Breaking the Diffraction Barrier - Optical Microscopy on a Nanometric Scale", *Science*, 251, 1468-1470 (1991).

[25] A. Naber, D. Molenda, U. C. Fischer, H. J. Maas, C. Hoppener, N. Lu and H. Fuchs, "Enhanced light confinement in a near-field optical probe with a triangular aperture", *Phys. Rev. Lett.*, 89, 210801 (2002).

[26] J. A. Veerman, A. M. Otter, L. Kuipers and N. F. van Hulst, "High definition aperture probes for near-field optical microscopy fabricated by focused ion beam milling", *Appl. Phys. Lett.*, 72, 3115-3117 (1998).

[27] A. V. Zayats and V. Sandoghdar, "Apertureless near-field optical microscopy via local second-harmonic generation", *J. Microsc.-Oxford*, 202, 94-99 (2001).

[28] R. Bachelot, P. Gleyzes and A. C. Boccara, "Reflection-mode scanning near-field optical microscopy using an apertureless metallic tip", *Appl. Optics*, 36, 2160-2170 (1997).

[29] Y. C. Martin, H. F. Hamann and H. K. Wickramasinghe, "Strength of the electric field in apertureless near-field optical microscopy", *J. Appl. Phys.*, 89, 5774-5778 (2001).

[30] P. G. Gucciardi and G. Bachelier, "Far-field background suppression in tip-modulated apertureless near-field optical microscopy", *J. Appl. Phys.*, 99, 124309 (2006).

[31] A. Kramer, W. Trabesinger, B. Hecht and U. P. Wild, "Optical near-field enhancement at a metal tip probed by a single fluorophore", *Appl. Phys. Lett.*, 80, 1652-1654 (2002).

[32] A. V. Zayats and V. Sandoghdar, "Apertureless scanning near-field second-harmonic microscopy", *Opt Commun*, 178, 245-249 (2000).

[33] B. Pettinger, B. Ren, G. Picardi, R. Schuster and G. Ertl, "Nanoscale probing of adsorbed species by tip-enhanced Raman spectroscopy", *Phys. Rev. Lett.*, 92, 096101 (2004).

[34] P. Verma, Y. Inouye and S. Kawata, "Tip-enhanced near-field Raman scattering: Fundamentals and new aspects for molecular nanoanalysis identification", *Top Appl. Phys.*, 103, 241-260 (2006).

[35] A. Tarun, N. Hayazawa, M. Motohashi and S. Kawata, "Highly efficient tip-enhanced Raman spectroscopy and microscopy of strained silicon", *Rev. Sci. Instrum.*, 79, 013706 (2008).

[36] L. V. Stebounova, Y. E. Romanyuk, D. X. Chen and S. R. Leone, "Imaging of InGaN inhomogeneities using visible apertureless near-field scanning optical microscope", *J. Appl. Phys.*, 101, 124306 (2007).

[37] E. Betzig, P. L. Finn and J. S. Weiner, "Combined Shear Force and near-Field Scanning Optical Microscopy", *Appl. Phys. Lett.*, 60, 2484-2486 (1992).

[38] E. Betzig, J. K. Trautman, J. S. Weiner, T. D. Harris and R. Wolfe, "Polarization Contrast in near-Field Scanning Optical Microscopy", *Appl. Optics*, 31, 4563-4568 (1992).

[39] E. Betzig and R. J. Chichester, "Single Molecules Observed by near-Field Scanning Optical Microscopy", *Science*, 262, 1422-1425 (1993).

[40] E. Betzig and R. J. Chichester, "Single Molecules Observed by near-Field Scanning Optical Microscopy (Nsom)", *Biophys. J.*, 66, 277-277 (1994).

[41] R. Kopelman and W. H. Tan, "Near-Field Optics - Imaging Single Molecules", *Science*, 262, 1382-1384 (1993).

[42] D. Zeisel, V. Deckert, R. Zenobi and T. Vo-Dinh, "Near-field surface-enhanced Raman spectroscopy of dye molecules adsorbed on silver island films", *Chem. Phys. Lett.*, 283, 381-385 (1998).

[43] L. Novotny, R. X. Bian and X. S. Xie, "Theory of nanometric optical tweezers", *Phys. Rev. Lett.*, 79, 645-648 (1997).

[44] G. W. Bryant, E. L. Shirley, L. S. Goldner, E. B. McDaniel, J. W. P. Hsu and R. J. Tonucci, "Theory of probing a photonic crystal with transmission near-field optical microscopy", *Phys. Rev. B*, 58, 2131-2141 (1998).

[45] A. Bouhelier, T. Huser, H. Tamaru, H. J. Guntherodt, D. W. Pohl, F. I. Baida and D. Van Labeke, "Plasmon optics of structured silver films", *Phys. Rev. B*, 6315, 155404 (2001).

[46] R. D. Grober, R. J. Schoelkopf and D. E. Prober, "Optical antenna: Towards a unity efficiency near-field optical probe", *Appl. Phys. Lett.*, 70, 1354-1356 (1997).

[47] R. L. McCreery, "Raman spectroscopy for chemical analysis", New York: John Wiley & Sons (2000).

[48] W. Ball, "Theory of Raman spectroscopy", *Spectroscopy*, 16, 32-34 (2001).

[49] S. M. Nie and S. R. Emory, "Single-molecule detection and spectroscopy by surface-enhanced Raman scattering." *Abstr. Pap. Am. Chem. S.*, 213, 177-PHYS (1997).

[50] P. Etchegoina and L. F. Cohenb, "Electromagnetic contribution to surface enhanced Raman scattering revisited", *J. Chem. Phys.*, 119, 5281-5289 (2003).

[51] A. Otto, I. Mrozek, H. Grabhorn and W. Akemann, "Surface-Enhanced Raman-Scattering", *J. Phys-Condens. Mat.*, 4, 1143-1212 (1992).

[52] E. J. Liang and P. X. Zhang, "Absorption and Surface-Enhanced Resonant Raman-Spectra of Riboflavin in Silver Colloid", *Chinese Phys.*, 11, 812-817 (1991).

[53] F. Akbarian, B. S. Dunn and J. I. Zink, "Surface-Enhanced Raman-Spectroscopy Using Photodeposited Gold Particles in Porous Sol-Gel Silicates", *J. Phys. Chem.-US*, 99, 3892-3894 (1995).

[54] S. Kruszewski, "The surface enhanced Raman scattering on electrochemically roughened silver electrodes", *Vacuum*, 48, 363-368 (1997).

[55] J. Sallack, A. K. Maiti, R. Aroca and J. R. Menendez, "Surface-enhanced resonant Raman spectra of perylenetetracarboxylic derivatives on silver colloids and island films", *J. Mol. Struct.*, 410, 217-221 (1997).

[56] J. A. Sanchez-Gil and J. V. Garcia-Ramos, "Calculations of the direct electromagnetic enhancement in surface enhanced Raman scattering on random self-affine fractal metal surfaces", *J. Chem. Phys.*, 108, 317-325 (1998).

[57] N. Zettsu, J. M. McLellan, B. Wiley, Y. D. Yin, Z. Y. Li and Y. N. Xia, "Synthesis, stability, and surface plasmonic properties of rhodium multipods, and their use as substrates for surface-enhanced Raman scattering", *Angew. Chem. Int. Edit.*, 45, 1288-1292 (2006).

[58] M. Futamata, Y. Maruyama and M. Ishikawa, "Metal nanostructures with single molecule sensitivity in surface enhanced Raman scattering", *Vib. Spectrosc.*, 35, 121-129 (2004).

[59] T. Vo-Dinh, "Surface-enhanced Raman spectroscopy using metallic nanostructures", *Trac-Trends in Anal. Chem.*, 17, 557-582 (1998).

[60] E. X. Jin and X. F. Xu, "Enhanced optical near field from a bowtie aperture", *Appl. Phys. Lett.*, 88, 153110 (2006).

[61] S. Zou, N. Janel and G. C. Schatz, "Silver nanoparticle array structures that produce remarkably narrow plasmon lineshapes", *J. Chem. Phys.*, 120, 10871-10875 (2004).

[62] R. L. Sobocinski and J. E. Pemberton, "Sers Investigation of Interfacial Methanol at Silver Electrodes", *Langmuir*, 6, 43-50 (1990).

[63] W. F. Pearman and A. W. Fountain, "Classification of chemical and biological warfare agent simulants by surface-enhanced Raman spectroscopy and multivariate statistical techniques", *Appl. Spectrosc.*, 60, 356-365 (2006).

[64] D. I. Ellis and R. Goodacre, "Metabolic fingerprinting in disease diagnosis: biomedical applications of infrared and Raman spectroscopy", *Analyst*, 131, 875-885 (2006).

[65] F. Adar, R. Geiger and J. Noonan, "Raman spectroscopy for process/quality control", *Appl. Spectrosc. Reviews*, 32, 45-101 (1997).

[66] N. Hayazawa, M. Motohashi, Y. Saito and S. Kawata, "Highly sensitive strain detection in strained silicon by surface-enhanced Raman spectroscopy", *Appl. Phys. Lett.*, 86, 263114 (2005).

[67] B. Pettinger, G. Picardi, R. Schuster and G. Ertl, "Surface-enhanced and STM-tip-enhanced Raman spectroscopy at metal surfaces", *Single Mol.*, 3, 285-294 (2002).

[68] D. Richards, R. G. Milner, F. Huang and F. Festy, "Tip-enhanced Raman microscopy: practicalities and limitations", *J. Raman Spectrosc.*, 34, 663-667 (2003).

[69] A. Hartschuh, M. R. Beversluis, A. Bouhelier and L. Novotny, "Tip-enhanced optical spectroscopy", *Philos. T. Roy. Soc. A*, 362, 807-819 (2004).

[70] J. Wessel, "Surface enhanced optical microscopy", *J. Opt. Soc. Am. B*, 2, 1538–1540 (1985).

[71] R. Zenobi and V. Deckert, "Scanning near-field optical microscopy and spectroscopy as a tool for chemical analysis", *Angew. Chem. Int. Edit.*, 39, 1746-1756 (2000).

[72] B. Pettinger, "Tip-enhanced Raman spectroscopy (TERS)", *Top Appl. Phys.*, 103, 217-240 (2006).

[73] B. Pettinger, G. Picardi, R. Schuster and G. Ertl, "Surface-enhanced and STM tip-enhanced Raman spectroscopy of CN- ions at gold surfaces", *J. Electroanal. Chem.*, 554, 293-299 (2003).

[74] L. Zhu, J. Atesang, P. Dudek, M. Hecker, J. Rinderknecht, Y. Ritz, H. Geisler, U. Herr, R. Greer and E. Zschech, "Experimental challenges for approaching local strain determination in silicon by nano-Raman spectroscopy", *Mater. Sci. -Poland*, 25, 19-31 (2007).

[75] A. Hartschuh, H. Qian, A. J. Meixner, N. Anderson and L. Novotny, "Nanoscale optical imaging of single-walled carbon nanotubes", *J. Lumin.*, 119, 204-208 (2006).

[76] W. H. Weber and R. Merlin, "Raman scattering in materials science", New York: Springer (2000).

[77] J. E. Griffith and G. P. Kochanski, "Scanning Tunneling Microscopy", *Annu. Rev. Mater. Sci.*, 20, 219-244 (1990).

[78] G. A. Baker and D. S. Moore, "Progress in plasmonic engineering of surface-enhanced Raman-scattering substrates toward ultra-trace analysis", *Anal. Bioanal. Chem.*, 382, 1751-1770 (2005).

[79] P. M. Campbell, E. S. Snow and P. J. McMarr, "AFM-based fabrication of Si nanostructures", *Physica B*, 227, 315-317 (1996).

[80] J. Schneir, J. A. Dagata and H. H. Harary, "Scanning Tunneling Microscope-Based Nanostructure Fabrication System", *J. Vac. Sci. Technol. A*, 11, 754-757 (1993).

[81] E. S. Snow and P. M. Campbell, "Fabrication of Si Nanostructures with an Atomic-Force Microscope", *Appl. Phys. Lett.*, 64, 1932-1934 (1994).

[82] S. A. Miller, K. L. Turner and N. C. MacDonald, "Microelectromechanical scanning probe instruments for array architectures", *Rev. Sci. Instrum.*, 68, 4155-4162 (1997).

[83] E. J. Van Loenen, D. Dijkkamop, A. J. Hoeven, J. M. Lenssinck and J. Dieleman, "direct writing in Si with a scanning tunneling microscope", *Appl. Phys. Lett.*, 55, 1312-1314 (1989).

[84] J. A. Dagata, J. Schneir, H. H. Harary, C. J. Evans, M. T. Postek and J. Bennett, "Modification of Hydrogen-Passivated Silicon by a Scanning Tunneling Microscope Operating in Air", *Appl. Phys. Lett.*, 56, 2001-2003 (1990).

[85] S. T. Yau, X. Zheng and M. H. Nayfeh, "Nanolithography of Chemically Prepared Si with a Scanning Tunneling Microscope", *Appl. Phys. Lett.*, 59, 2457-2459 (1991).

[86] E. Hartmann, R. J. Behm, G. Krotz, G. Muller and F. Koch, "Writing Electronically Active Nanometer-Scale Structures with a Scanning Tunneling Microscope", *Appl. Phys. Lett.*, 59, 2136-2138 (1991).

[87] E. S. Snow, P. M. Campbell and P. J. Mcmarr, "Fabrication of Silicon Nanostructures with a Scanning Tunneling Microscope", *Appl. Phys. Lett.*, 63, 749-751 (1993).

[88] K. Matsumoto, M. Ishii and K. Segawa, "Application of scanning tunneling microscopy nanofabrication process to single electron transistor", *J. Vac. Sci. Technol. B*, 14, 1331-1335 (1996).

[89] W. Xie, X. Dai, L. S. Xu, D. A. Allee and J. Spector, "Fabrication of Cr nanostructures with the scanning tunnelling microscope", *Nanotechnology*, 8, 88-93 (1997).

[90] H. C. Day and D. R. Allee, "Selective area oxidation of Si3N4 with an ambient scanning tunneling microscope", *Nanotechnology*, 7, 106-109 (1996).

[91] A. Houel, D. Tonneau, N. Bonnail, H. Dallaporta and V. I. Safarov, "Direct patterning of nanostructures by field-induced deposition from a scanning tunneling microscope tip", *J. Vac. Sci. Technol. B*, 20, 2337-2345 (2002).

[92] D. Fujita, K. Onishi and T. Kumakura, "Silver nanostructures formation on Si(111)-(7 x 7) surfaces by the tip of a scanning tunneling microscope", *Jpn J. Appl. Phys. 1*, 42, 4773-4776 (2003).

[93] H. Rauscher, F. Behrendt and R. J. Behm, "Fabrication of surface nanostructures by scanning tunneling microscope induced decomposition of SiH4 and SiH2Cl2", *J. Vac. Sci. Technol. B*, 15, 1373-1377 (1997).

[94] H. Iwasaki, T. Yoshinobu and K. Sudoh, "Nanolithography on SiO2/Si with a scanning tunnelling microscope", *Nanotechnology*, 14, R55-R62 (2003).

[95] S. W. Hla, K. F. Braun and K. H. Rieder, "Single-atom manipulation mechanisms during a quantum corral construction", *Phys. Rev. B*, 67, 201402 (2003).

[96] I. W. Lyo and P. Avouris, "Field-Induced Nanometer-Scale to Atomic-Scale Manipulation of Silicon Surfaces with the Stm", *Science*, 253, 173-176 (1991).

[97] C. T. Salling and M. G. Lagally, "Fabrication of Atomic-Scale Structures on Si(001) Surfaces", *Science*, 265, 502-506 (1994).

[98] Stefan Grafstrom, "Photoassisted scanning tunneling microscopy", *J. Appl. Phys.*, 91, 1717-1753 (2002).

[99] C. Y. Liu and A. J. Bard, "Irradiation-Induced Nanometer-Scale Surface Etching of a Cdse Film with a Scanning Tunneling Microscope", *Chem. Phys. Lett.*, 174, 162-166 (1990).

[100] A. A. Gorbunov and W. Pompe, "Thin-Film Nanoprocessing by Laser Stm Combination", *Phys. Status Solidi A*, 145, 333-338 (1994).

[101] J. Jersch and K. Dickmann, "Nanostructure fabrication using laser field enhancement in the near field of a scanning tunneling microscope tip", *Appl. Phys. Lett.*, 68, 868-870 (1996).

[102] Z. H. Mai, Y. F. Lu, S. M. Huang, W. K. Chim and J. S. Pan, "Mechanism of laser-induced nanomodification on hydrogen-passivated Si(100) surfaces underneath the tip of a scanning tunneling microscope", *J. Vac. Sci. Technol. B*, 18, 1853-1857 (2000).

[103] Y. F. Lu, Z. H. Mai, G. Qiu and W. K. Chim, "Laser-induced nano-oxidation on hydrogen-passivated Ge (100) surfaces under a scanning tunneling microscope tip", *Appl. Phys. Lett.*, 75, 2359-2361 (1999).

[104] Y. F. Lu, Z. H. Mai, Y. W. Zheng and W. D. Song, "Nanostructure fabrication using pulsed lasers in combination with a scanning tunneling microscope: Mechanism investigation", *Appl. Phys. Lett.*, 76, 1200-1202 (2000).

[105] V. A. Ukraintsev and J. T. Yates, "Nanosecond laser induced single atom deposition with nanometer spatial resolution using a STM", *J. Appl. Phys.*, 80, 2561-2571 (1996).

[106] J. Boneberg, H. J. Munzer, M. Tresp, M. Ochmann and P. Leiderer, "The mechanism of nanostructuring upon nanosecond laser irradiation of a STM tip", *Appl. Phys. a-Mater.*, 67, 381-384 (1998).

Chapter 3

[1] A. Bouhelier, "Field-enhanced scanning near-field optical microscopy", *Microsc. Res. Techniq.*, 69, 563-579 (2006).

[2] I. Notingher and A. Elfick, "Effect of sample and substrate electric properties on the electric field enhancement at the apex of SPM nanotips", *J. Phys. Chem.-US B*, 109, 15699-15706 (2005).

[3] W. Denk and D. W. Pohl, "Near-Field Optics - Microscopy with Nanometer-Size Fields", *J. Vac. Sci. Technol. B*, 9, 510-513 (1991).

[4] A. V. Zayats, "Electromagnetic field enhancement in the context of apertureless near-field microscopy", *Opt. Commun.*, 161, 156-162 (1999).

[5] O. J. F. Martin and C. Girard, "Controlling and tuning strong optical field gradients at a local probe microscope tip apex", *Appl. Phys. Lett.*, 70, 705-707 (1997).

[6] L. Novotny, R. X. Bian and X. S. Xie, "Theory of nanometric optical tweezers", *Phys. Rev. Lett.*, 79, 645-648 (1997).

[7] W. X. Sun and Z. X. Shen, "Optimizing the near field around silver tips", *J. Opt. Soc. Am. A*, 20, 2254-2259 (2003).

[8] J. L. Bohn, D. J. Nesbitt and A. Gallagher, "Field enhancement in apertureless near-field scanning optical microscopy", *J. Opt. Soc. Am. A*, 18, 2998-3006 (2001).

[9] X. Li, Z. G. Chen, A. Taflove and V. Backman, "Optical analysis of nanoparticles via enhanced backscattering facilitated by 3-D photonic nanojets", *Opt. Express*, 13, 526-533 (2005).

[10] Z. Chen and A. Taflove, "Photonic nanojet enhancement of backscattering of light by nanoparticles: a potential novel visible-light ultramicroscopy technique", *Opt. Express*, 12, 1214-1220 (2004).

[11] S. Lecler, Y. Takakura and P. Meyrueis, "Properties of a three-dimensional photonic jet", *Opt. Lett.*, 30, 2641-2643 (2005).

[12] A. V. Itagi and W. A. Challener, "Optics of photonic nanojets", *J. Opt. Soc. Am. A*, 22, 2847-2858 (2005).

[13] M. I. Markovic and A. D. Rakic, "Determination of Optical-Properties of Aluminum Including Electron Reradiation in the Lorentz-Drude Model", *Opt. Laser Technol.*, 22, 394-398 (1990).

[14] M. I. Markovic and A. D. Rakic, "Determination of the Reflection Coefficients of Laser-Light of Wavelengths Lambda-Epsilon(0.22 Mu-M,200 Mu-M) from the Surface of Aluminum Using the Lorentz-Drude Model", *Appl. Optics*, 29, 3479-3483 (1990).

[15] R. Zhang, P. Catrysse and S. Dods, “Finite-difference time-domain method guides optical design of metallic nanostructures”, Laser Focus World, 07, 67-71 (2004).

[16] W. H. Zhang, X. D. Cui, B. S. Yeo, T. Schmid, C. Hafner and R. Zenobi, "Nanoscale roughness on metal surfaces can increase tip-enhanced Raman scattering by an order of magnitude", *Nano Lett.*, 7, 1401-1405 (2007).

Chapter 4

[1] E. Smith and G. Dent, "Modern Raman Spectroscope: A Practical Approach", New Jersey: Wiley (2005).

[2] A. Feofanov, S. Sharonov, P. Valisa, E. Dasilva, I. Nabiev and M. Manfait, "A New Confocal Stigmatic Spectrometer for Micro-Raman and Microfluorescence Spectral Imaging Analysis - Design and Applications", *Rev. Sci. Instrum.*, 66, 3146-3158 (1995).

[3] D. K. Veirs, J. W. Ager, E. T. Loucks and G. M. Rosenblatt, "Mapping Materials Properties with Raman-Spectroscopy Utilizing a 2-D Detector", *Appl. Optics*, 29, 4969-4980 (1990).

[4] H. S. Sands, F. Demangeot, E. Bonera, S. Webster, R. Bennett, I. P. Hayward, F. Marchi, D. A. Smith and D. N. Batchelder, "Development of a combined confocal and scanning near-field Raman microscope for deep UV laser excitation", *J. Raman Spectrosc.*, 33, 730-739 (2002).

[5] D. Wolverson and S. V. Railson, "Automated Resonance Raman-Spectroscopy", *Meas. Sci. Technol.*, 4, 1080-1084 (1993).

[6] B. M. Cullum, J. Mobley, Z. H. Chi, D. L. Stokes, G. H. Miller and T. Vo-Dinh, "Development of a compact, handheld Raman instrument with no moving parts for use in field analysis", *Rev. Sci. Instrum.*, 71, 1602-1607 (2000).

[7] J. Kim, G. L. Liu and L. P. Lee, "Lens-scanning Raman microspectroscopy system using compact disc optical pickup technology", *Opt. Express*, 13, 4780-4785 (2005).

[8] A. Paipetis, C. Vlattas and C. Galiotis, "Remote laser Raman microscopy (ReRaM) .1. Design and testing of a confocal microprobe", *J. Raman Spectrosc.*, 27, 519-526 (1996).

[9] W. H. Weber and R. Merlin, "Raman scattering in materials science", New York: Springer (2000).

[10] S. Schlucker, M. D. Schaeberle, S. W. Huffman and I. W. Levin, "Raman microspectroscopy: A comparison of point, line, and wide-field imaging methodologies", *Anal. Chem.*, 75, 4312-4318 (2003).

[11] B. Pettinger, G. Picardi, R. Schuster and G. Ertl, "Surface-enhanced and STM tip-enhanced Raman spectroscopy of CN- ions at gold surfaces", *J. Electroanal. Chem.*, 554, 293-299 (2003).

[12] A. Otto, I. Mrozek, H. Grabhorn and W. Akemann, "Surface-Enhanced Raman-Scattering", *J. Phys-Condens. Mat.*, 4, 1143-1212 (1992).

[13] A. Hartschuh, M. R. Beversluis, A. Bouhelier and L. Novotny, "Tip-enhanced optical spectroscopy", *Philos. T. Roy. Soc. A*, 362, 807-819 (2004).

[14] A. Bouhelier, "Field-enhanced scanning near-field optical microscopy", *Microsc. Res. Techniq.*, 69, 563-579 (2006).

[15] A. Barbara, T. Lopez-Rios and P. Quemerais, "Near-field optical microscopy with a scanning tunneling microscope", *Rev. Sci. Instrum.*, 76, 023704 (2005).

[16] N. Hayazawa, Y. Inouye, Z. Sekkat and S. Kawata, "Near-field Raman scattering enhanced by a metallized tip", *Chem. Phys. Lett.*, 335, 369-374 (2001).

[17] J. Steidtner and B. Pettinger, "High-resolution microscope for tip-enhanced optical processes in ultrahigh vacuum", *Rev. Sci. Instrum.*, 78, 103104 (2007).

[18] M. Motohashi, N. Hayazawa, A. Tarun and S. Kawata, "Depolarization effect in reflection-mode tip-enhanced Raman scattering for Raman active crystals", *J. Appl. Phys.*, 103, 034309 (2008).

[19] A. Tarun, N. Hayazawa, M. Motohashi and S. Kawata, "Highly efficient tip-enhanced Raman spectroscopy and microscopy of strained silicon", *Rev. Sci. Instrum.*, 79, 013706 (2008).

[20] A. Hartschuh, N. Anderson and L. Novotny, "Near-field Raman spectroscopy using a sharp metal tip", *J. Microsc.-Oxford*, 210, 234-240 (2003).

[21] I. Notingher and A. Elfick, "Effect of sample and substrate electric properties on the electric field enhancement at the apex of SPM nanotips", *J. Phys. Chem.-US B*, 109, 15699-15706 (2005).

[22] G. Irmer and A. Dorner-Reisel, "Micro-Raman studies on DLC coatings", *Adv. Eng. Mater.*, 7, 694-705 (2005).

[23] J. Shi, Y. F. Lu, K. J. Yi, Y. S. Lin, S. H. Liou, J. B. Hou and X. W. Wang, "Direct synthesis of single-walled carbon nanotubes bridging metal electrodes by laser-assisted chemical vapor deposition", *Appl. Phys. Lett.*, 89, 083105 (2006).

[24] E. J. Sanchez, J. T. Krug and X. S. Xie, "Ion and electron beam assisted growth of nanometric SimOn structures for near-field microscopy", *Rev. Sci. Instrum.*, 73, 3901-3907 (2002).

[25] P. Nordlander and F. Le, "Plasmonic structure and electromagnetic field enhancements in the metallic nanoparticle-film system", *Appl. Phys. B-Lasers O.*, 84, 35-41 (2006).

[26] N. Hayazawa, Y. Saito and S. Kawata, "Detection and characterization of longitudinal field for tip-enhanced Raman spectroscopy", *Appl. Phys. Lett.*, 85, 6239-6241 (2004).

[27] V. Poborchii, T. Tada and T. Kanayama, "Subwavelength-resolution Raman microscopy of si structures using metal-particle-topped AFM probe", *Jpn. J. Appl. Phys.*, 44, L202-L204 (2005).

[28] N. Lee, R. D. Hartschuh, D. Mehtani, A. Kisliuk, J. F. Maguire, M. Green, M. D. Foster and A. P. Sokolov, "High contrast scanning nano-Raman spectroscopy of silicon", *J. Raman Spectrosc.*, 38, 789-796 (2007).

Chapter 5

[1] D. S. Chuu and W. F. Hsieha C. M. Dai, "Raman intensity enhancement of the Si peak by CdS thin films", *Appl. Phys. Lett.*, 59, 3273-3275 (1991).

[2] Z. S. Nickolov, J. C. Earnshaw and J. J. Mcgarvey, "Total Internal-Reflection Raman-Spectroscopy as a Method to Study Water-Structure near Langmuir-Blodgett-Films", *J. Raman Spectrosc.*, 24, 411-416 (1993).

[3] N. P. W. Pieczonka, P. J. G. Goulet and R. F. Aroca, "Applications of the enhancement of resonance Raman scattering and fluorescence by strongly coupled metallic nanostructures", *Top Appl. Phys.*, 103, 197-216 (2006).

[4] C. L. Jahncke, H. D. Hallen and M. A. Paesler, "Nano-Raman spectroscopy and imaging with near-field scanning optical microscope", *J. Raman Spectrosc.*, 27, 579-586 (1996).

[5] P. Etchegoina and L. F. Cohenb, "Electromagnetic contribution to surface enhanced Raman scattering revisited", *J. Chem. Phys.*, 119, 5281-5289 (2003).

[6] E. C. L. Ru, E. Blackie, M. Meyer and P. G. Etchegoin, "Surface enhanced Raman scattering enhancement factors: a comprehensive study", *J. Phys. Chem.-US C*, 111, 13794-13803 (2007).

[7] N. Anderson, A. Bouhelier and L. Novotny, "Near-field photonics: tip-enhanced microscopy and spectroscopy on the nanoscale", *J. Opt. a-Pure Appl. Op.*, 8, S227-S233 (2006).

[8] W. H. Zhang, B. S. Yeo, T. Schmid and R. Zenobi, "Single molecule tip-enhanced Raman spectroscopy with silver tips", *J. Phys. Chem.-US C*, 111, 1733-1738 (2007).

[9] B. Ren, G. Picardi and B. Pettinger, "Preparation of gold tips suitable for tip-enhanced Raman spectroscopy and light emission by electrochemical etching", *Rev. Sci. Instrum.*, 75, 837-841 (2004).

[10] B. Pettinger, "Tip-enhanced Raman spectroscopy (TERS)", *Top Appl. Phys.*, 103, 217-240 (2006).

[11] X. Li, Z. G. Chen, A. Taflove and V. Backman, "Optical analysis of nanoparticles via enhanced backscattering facilitated by 3-D photonic nanojets", *Opt. Express*, 13, 526-533 (2005).

[12] Z. Chen and A. Taflove, "Photonic nanojet enhancement of backscattering of light by nanoparticles: a potential novel visible-light ultramicroscopy technique", *Opt. Express*, 12, 1214-1220 (2004).

[13] D. S. Benincasa, P. W. Barber, J. Z. Zhang, W. F. Hsieh, and R. K. Chang, “Spatial distribution of the internal and near-field intensities of large cylindrical and spherical scatterers”, *Appl. Opt.*, 26, 1348-1356 (1987).

[14] W. X. Sun and Z. X. Shen, "Near-field scanning Raman microscopy using apertureless probes", *J. Raman Spectrosc.*, 34, 668-676 (2003).

Chapter 6

[1] M. Moskovits, "Surface-enhanced Raman spectroscopy: a brief perspective", *Top Appl. Phys.*, 103, 1-17 (2006).

[2] A. Hartschuh, H. Qian, A. J. Meixner, N. Anderson and L. Novotny, "Tip-enhanced optical spectroscopy for surface analysis in biosciences", *Surf. Interface Anal.*, 38, 1472-1480 (2006).

[3] X. Wang, Z. Liu, M. D. Zhuang, H. M. Zhang, X. Wang, Z. X. Xie, D. Y. Wu, B. Ren and Z. Q. Tian, "Tip-enhanced Raman spectroscopy for investigating adsorbed species on a single-crystal surface using electrochemically prepared Au tips", *Appl. Phys. Lett.*, 91, 101105 (2007).

[4] Y. Saito, M. Motohashi, N. Hayazawa, M. Iyoki and S. Kawata, "Nanoscale characterization of strained silicon by tip-enhanced Raman spectroscope in reflection mode", *Appl. Phys. Lett.*, 88, 143109 (2006).

[5] A. Hartschuh, H. Qian, A. J. Meixner, N. Anderson and L. Novotny, "Nanoscale optical imaging of single-walled Carbon nanotubes", *J. Lumin.*, 119, 204-208 (2006).

[6] W. H. Zhang, B. S. Yeo, T. Schmid and R. Zenobi, "Single molecule tip-enhanced Raman spectroscopy with silver tips", *J. Phys. Chem.-US C*, 111, 1733-1738 (2007).

[7] G. A. Baker and D. S. Moore, "Progress in plasmonic engineering of surface-enhanced Raman-scattering substrates toward ultra-trace analysis", *Anal. Bioanal. Chem.*, 382, 1751-1770 (2005).

[8] K. Kneipp, H. Kneipp, R. R. Dasari and M. S. Feld, "Single molecule Raman spectroscopy using silver and gold nanoparticles", *Indian J. Phys. Pt-B*, 77B, 39-47 (2003).

[9] K. Kneipp, H. Kneipp and I. Itzkan, "Ultrasensitive Raman spectroscopy at the single-molecule level based on surface-enhanced Raman scattering on silver and gold colloidal clusters." *Abstr. Pap. Am. Chem. S.*, 221, U244-U244 (2001).

[10] W. Song, W. Li, Y. C. Cheng, H. Y. Jia, G. R. Zhao, Y. H. Zhou, B. Yang, W. Q. Xu, W. J. Tian and B. Zhao, "Surface enhanced Raman scattering from a hierarchical substrate of micro/nanostructured silver", *J. Raman Spectrosc.*, 37, 755-761 (2006).

[11] A. J. Haes, W. P. Hall and R. P. Van Duyne, "Nanoscale plasmonics begins to unravel Alzheimer's disease", *Laser Focus World*, 41, 105-109 (2005).

[12] W. H. Zhang, X. D. Cui, B. S. Yeo, T. Schmid, C. Hafner and R. Zenobi, "Nanoscale roughness on metal surfaces can increase tip-enhanced Raman scattering by an order of magnitude", *Nano Lett.*, 7, 1401-1405 (2007).

[13] P. Olk, J. Renger, T. Hartling, M. T. Wenzel and L. M. Eng, "Two particle enhanced nano Raman microscopy and spectroscopy", *Nano Lett.*, 7, 1736-1740 (2007).

[14] T. R. Jensen, G. C. Schatz and R. P. Van Duyne, "Nanosphere lithography: Surface plasmon resonance spectrum of a periodic array of silver nanoparticles by ultraviolet-visible extinction spectroscopy and electrodynamic modeling", *J. Phys. Chem. B*, 103, 2394-2401 (1999).

[15] H. Wang, C. S. Levin and N. J. Halas, "Nanosphere arrays with controlled sub-10-nm gaps as surface-enhanced Raman spectroscopy substrates", *J. Am. Chem. Soc.*, 127, 14992-14993 (2005).

[16] A. Tarun, N. Hayazawa, M. Motohashi and S. Kawata, "Highly efficient tip-enhanced Raman spectroscopy and microscopy of strained silicon", *Rev. Sci. Instrum.*, 79, 013706 (2008).

[17] N. Hayazawa, M. Motohashi, Y. Saito, H. Ishitobi, A. Ono, T. Ichimura, P. Verma and S. Kawata, "Visualization of localized strain of a crystalline thin layer at the nanoscale by tip-enhanced Raman spectroscopy and microscopy", *J. Raman Spectrosc.*, 38, 684-696 (2007).

[18] N. Hayazawa, M. Motohashi, Y. Saito and S. Kawata, "Highly sensitive strain detection in strained silicon by surface-enhanced Raman spectroscopy", *Appl. Phys. Lett.*, 86, 263114 (2005).

[19] N. Lee, R. D. Hartschuh, D. Mehtani, A. Kisliuk, J. F. Maguire, M. Green, M. D. Foster and A. P. Sokolov, "High contrast scanning nano-Raman spectroscopy of silicon", *J. Raman Spectrosc.*, 38, 789-796 (2007).

[20] J. Steidtner and B. Pettinger, "High-resolution microscope for tip-enhanced optical processes in ultrahigh vacuum", *Rev. Sci. Instrum.*, 78, 103104 (2007).

[21] T. Atay, J. H. Song and A. V. Nurmikko, "Strongly interacting plasmon nanoparticle pairs: From dipole-dipole interaction to conductively coupled regime", *Nano Lett.*, 4, 1627-1631 (2004).

[22] M. Danckwerts and L. Novotny, "Optical frequency mixing at coupled gold nanoparticles", *Phys. Rev. Lett.*, 98, 026104 (2007).

[23] R. Saito, T. Takeya, T. Kimura, G. Dresselhaus and M. S. Dresselhaus, "Raman intensity of single-wall Carbon nanotubes", *Phys. Rev. B*, 57, 4145-4153 (1998).

Chapter 7

[1] P. Avouris, T. Hertel, R. Martel, T. Schmidt, H. R. Shea and R. E. Walkup, "Carbon nanotubes: nanomechanics, manipulation, and electronic devices", *Appl. Surf. Sci.*, 141, 201-209 (1999).

[2] P. Avouris, "Electronics and optoelectronics with single Carbon nanotubes." *Abstr. Pap. Am. Chem. S.*, 229, U708-U709 (2005).

[3] P. Avouris, "Molecular electronics with Carbon nanotubes", *Accounts Chem. Res.*, 35, 1026-1034 (2002).

[4] P. Avouris, "Nanotube electronics - Electronics with Carbon nanotubes", *Phys. World*, 20, 40-45 (2007).

[5] D. E. H. Jones, "Science of fullerenes and Carbon nanotubes – Dresselhaus MS, Dresselhaus G, Eklund PC", *Nature*, 381, 384-384 (1996).

[6] Z. H. Chen, J. Appenzeller, Y. M. Lin, J. Sippel-Oakley, A. G. Rinzler, J. Y. Tang, S. J. Wind, P. M. Solomon and P. Avouris, "An integrated logic circuit assembled on a single carbon nanotube", *Science*, 311, 1735-1735 (2006).

[7] S. K. Doorn, M. J. O'Connell, L. X. Zheng, Y. T. Zhu, S. M. Huang and J. Liu, "Raman spectral imaging of a carbon nanotube intramolecular junction", *Phys. Rev. Lett.*, 94, 016802 (2005).

[8] J. Shi, Y. F. Lu, H. Wang, K. J. Yi, Y. S. Lin, R. Zhang and S. H. Liou, "Synthesis of suspended Carbon nanotubes on silicon inverse-opal structures by laser-assisted chemical vapour deposition", *Nanotechnology*, 17, 3822-3826 (2006).

[9] S. R. C. Vivekchand, A. Govindaraj, M. M. Seikh and C. N. R. Rao, "New method of purification of Carbon nanotubes based on hydrogen treatment", *J. Phys. Chem.-US B*, 108, 6935-6937 (2004).

[10] A. Jorio, R. Saito, J. H. Hafner, C. M. Lieber, M. Hunter, T. McClure, G. Dresselhaus and M. S. Dresselhaus, "Structural (n, m) determination of isolated single-wall Carbon nanotubes by resonant Raman scattering", *Phys. Rev. Lett.*, 86, 1118-1121 (2001).

[11] D. Kahn and J. P. Lu, "Vibrational modes of Carbon nanotubes and nanoropes", *Phys. Rev. B*, 60, 6535-6540 (1999).

[12] M. S. Dresselhaus, G. Dresselhaus, R. Saito and A. Jorio, "Raman spectroscopy of Carbon nanotubes", *Phys. Rep.*, 409, 47-99 (2005).

[13] J. Maultzsch, "Vibrational properties of carbon nanotubes and graphite", Berlin: PhD dissertation (2004).

[14] M. S. Dresselhaus, G. Dresselhaus, A. Jorio, A. G. Souza and R. Saito, "Raman spectroscopy on isolated single wall Carbon nanotubes", *Carbon*, 40, 2043-2061 (2002).

[15] C. Thomsen, "Second-order Raman spectra of single and multiwalled Carbon nanotubes", *Phys. Rev. B*, 61, 4542-4544 (2000).

[16] J. N. Chen, W. S. Yang, K. Dick, K. Deppert, H. Q. Xu, L. Samuelson and H. X. Xu, "Tip-enhanced Raman scattering of p-thiocresol molecules on individual gold nanoparticles", *Appl. Phys. Lett.*, 92, 093110 (2008).

[17] B. Pettinger, "Tip-enhanced Raman spectroscopy (TERS)", *Top Appl. Phys.*, 103, 217-240 (2006).

Chapter 8

[1] Y. Takahashi H. Togashi, A. Kato, A. Konno, H. Asaoka, and M. Suemitsu, "Observation of Initial Oxidation on Si(110)-16 x 2 surface by Scanning Tunneling Microscopy", *Jpn J. Appl. Phys.*, Vol. 46, 3239–3243 (2007).

[2] N. Barniol, F. Perezmurano and X. Aymerich, "Modification of Hf-Treated Silicon (100) Surfaces by Scanning Tunneling Microscopy in Air under Imaging Conditions", *Appl. Phys. Lett.*, 61, 462-464 (1992).

[3] J. A. Dagata, J. Schneir, H. H. Harary, C. J. Evans, M. T. Postek and J. Bennett, "Modification of Hydrogen-Passivated Silicon by a Scanning Tunneling Microscope Operating in Air", *Appl. Phys. Lett.*, 56, 2001-2003 (1990).

[4] A. A. Tseng, A. Notargiacomo and T. P. Chen, "Nanofabrication by scanning probe microscope lithography: A review", *J. Vac. Sci. Technol. B*, 23, 877-894 (2005).

[5] P. M. Campbell, E. S. Snow and P. J. McMarr, "Nanofabrication with proximal probes", *Surf. Sci.*, 362, 870-873 (1996).

[6] K. Sattler, "Nanolithography using the scanning tunneling microscope", *Jpn J. Appl. Phys. 1*, 42, 4825-4829 (2003).

[7] E. J. Vanloenen, D. Dijkkamp, A. J. Hoeven, J. M. Lenssinck and J. Dieleman, "Nanometer Scale Structuring of Silicon by Direct Indentation", *J. Vac. Sci. Technol. A*, 8, 574-576 (1990).

[8] S. Heike, T. Hashizume and Y. Wada, "Nanoneedle formation on silicon (111) surface using a scanning tunneling microscope tip", *J. Appl. Phys.*, 80, 4182-4188 (1996).

[9] J. Jersch and K. Dickmann, "Nanostructure fabrication using laser field enhancement in the near field of a scanning tunneling microscope tip", *Appl. Phys. Lett.*, 68, 868-870 (1996).

[10] M. Calleja, J. Anguita, R. Garcia, K. Birkelund, F. Perez-Murano and J. A. Dagata, "Nanometre-scale oxidation of silicon surfaces by dynamic force microscopy: reproducibility, kinetics and nanofabrication", *Nanotechnology*, 10, 34-38 (1999).

[11] Y. F. Lu, Z. H. Mai, W. D. Song and W. K. Chim, "Scanning tunnelling microscopy imaging and modification of hydrogen-passivated Ge(100) surfaces", *Appl. Phys. a-Mater.*, 70, 403-406 (2000).

[12] Y. F. Lu, Z. H. Mai, Y. W. Zheng and W. D. Song, "Nanostructure fabrication using pulsed lasers in combination with a scanning tunneling microscope: Mechanism investigation", *Appl. Phys. Lett.*, 76, 1200-1202 (2000).

[13] Z. H. Mai, Y. F. Lu, W. D. Song and W. K. Chim, "Nano-modification on hydrogen-passivated Si surfaces by a laser-assisted scanning tunneling microscope operating in air", *Appl Surf. Sci.*, 154, 360-364 (2000).

[14] X. W. Wang, "Large-scale molecular dynamics simulation of surface nanostructuring with a laser-assisted scanning tunnelling microscope", *J. Phys. D Appl. Phys.*, 38, 1805-1823 (2005).

[15] X. W. Wang and Y. F. Lu, "Solidification and epitaxial regrowth in surface nanostructuring with laser-assisted scanning tunneling microscope", *J. Appl. Phys.*, 98, 114304 (2005).

[16] V. A. Ukraintsev and J. T. Yates, "Nanosecond laser induced single atom deposition with nanometer spatial resolution using a STM", *J. Appl. Phys.*, 80, 2561-2571 (1996).

[17] Z. Dohnalek, I. Lyubinetsky and J. T. Yates, "Laser pulse desorption under scanning tunneling microscope tip-Cl removal from single site on Si(100)", *J. Vac. Sci. Technol. A*, 15, 1488-1492 (1997).

[18] W. X. Sun and Z. X. Shen, "Apertureless near-field scanning Raman microscopy using reflection scattering geometry", *Ultramicroscopy*, 94, 237-244 (2003).

[19] L. Gomez, R. Bachelot, A. Bouhelier, G. P. Wiederrecht, S. H. Chang, S. K. Gray, F. Hua, S. Jeon, J. A. Rogers, M. E. Castro, S. Blaize, I. Stefanon, G. Lerondel and P. Royer, "Apertureless scanning near-field optical microscopy: a comparison between homodyne and heterodyne approaches", *J. Opt. Soc. Am. B*, 23, 823-833 (2006).

[20] F. Demming, J. Jersch, K. Dickmann and P. I. Geshev, "Calculation of the field enhancement on laser-illuminated scanning probe tips by the boundary element method", *Appl. Phys. B-Lasers O.*, 66, 593-598 (1998).

[21] A. Hartschuh, M. R. Beversluis, A. Bouhelier and L. Novotny, "Tip-enhanced optical spectroscopy", *Philos. T. Roy. Soc. A*, 362, 807-819 (2004).

[22] E. Hartmann, R. J. Behm, G. Krotz, G. Muller and F. Koch, "Writing Electronically Active Nanometer-Scale Structures with a Scanning Tunneling Microscope", *Appl. Phys. Lett.*, 59, 2136-2138 (1991).

[23] H. A. Lin, R. Jaccodine and M. S. Freund, "Doping-density dependence of scanning tunneling spectroscopy on lightly doped silicon", *Appl. Phys. Lett.*, 72, 1993-1995 (1998).

[24] R. M. Ostrom, D. M. Tanenbaum and A. Gallagher, "Construction of Silicon Nanocolumns with the Scanning Tunneling Microscope", *Appl. Phys. Lett.*, 61, 925-927 (1992).

[25] S. T. Yau, X. Zheng and M. H. Nayfeh, "Nanolithography of Chemically Prepared Si with a Scanning Tunneling Microscope", *Appl. Phys. Lett.*, 59, 2457-2459 (1991).

[26] R. J. Hamers, "Atomic-Resolution surface spectroscopy with the scanning tunneling microscope", *Annu. Rev. Phys. Chem.*, 40, 531-559 (1989).

[27] W. J. Kaiser, L. D. Bell, M. H. Hecht and F. J. Grunthaner, "Scanning tunneling microscopy characterization of the geometric and electronic structure of hydrogen-terminated silicon surfaces", *J. Vac. Sci. Technol. A*, 6, 519-523 (1988).

[28] P. E. West, J. Jahanmir, A. Young, and T. N. Rhodin, "Current-voltage characteristics of silicon measured with the scanning tunneling microscope in air", *J. Vac. Sci. Technol. A*, 7, 2741-2744 (1989).

APPENDIX

1. Software program for Raman imaging: interface and source code

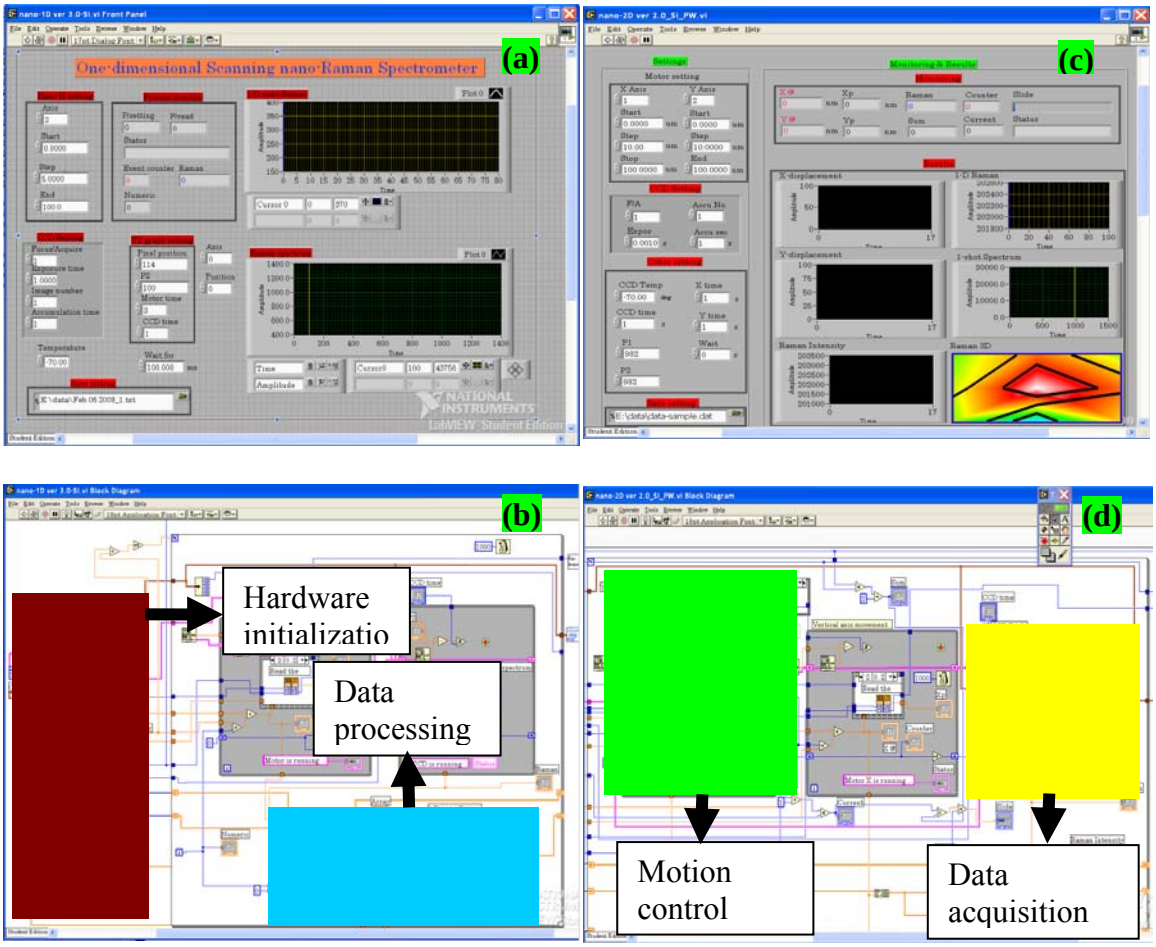

FIGURE A.1 (a, c) Software program interface and (b, d) source code of 1D profiling and of 2D mapping, respectively.

In addition to the hardware design, the software design was also implemented using Labview™ platform for the 1D profiling and the 2D mapping. The programs are used to initialize the hardware, such as the nanopositioner, the spectrograph and the CCD camera, control the nanopositioner, and acquire, analyze and process data.

2. The versatile multifunctional nanoscale characterization system

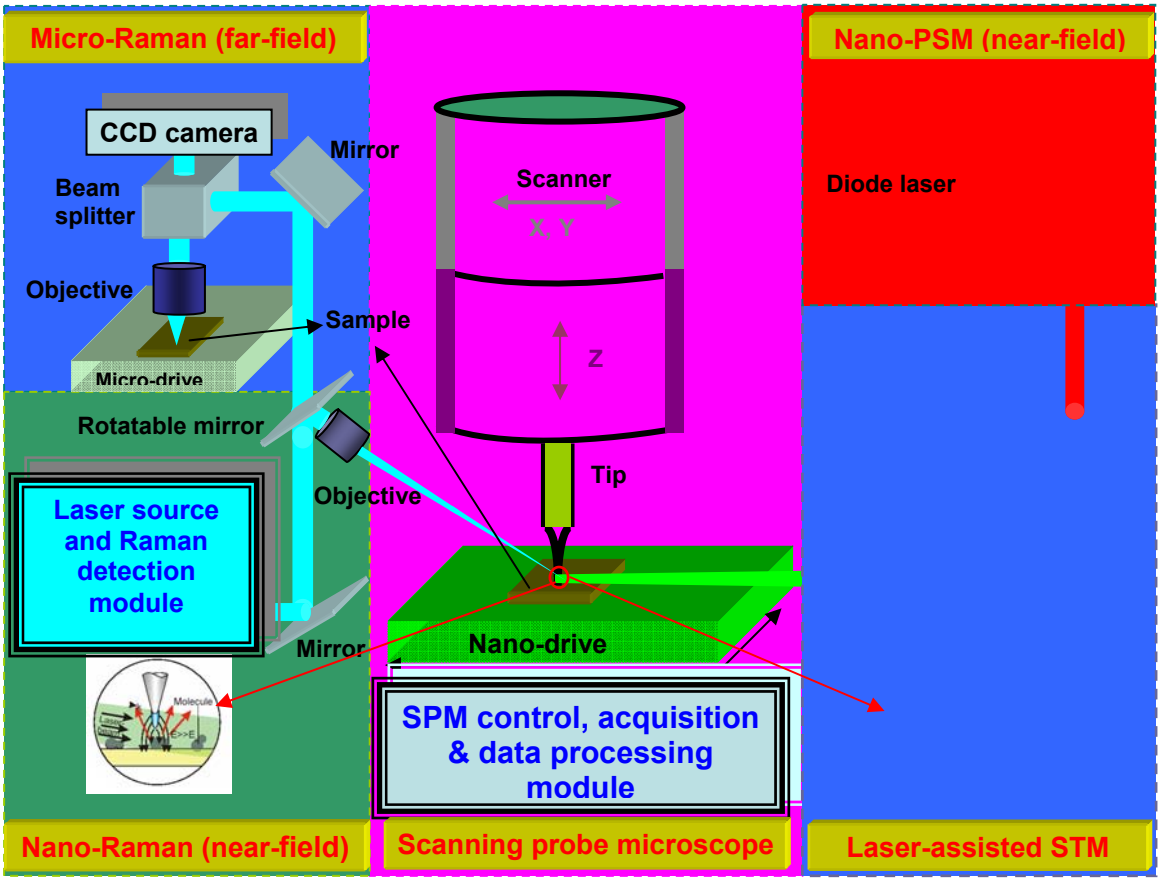

FIGURE A.2 Schematic diagram of the versatile multifunctional nanoscale characterization system.

As shown in Fig. A.2, the multifunctional nanoscale characterization system consists of five modules, including a Scanning Probe Microscope (SPM), a far-field Micro-Raman Spectrometer (μRS), a near-field Nano-Raman Spectrometer (nRS), an optical path for Laser Assisted Scanning Tunneling Microscope (LASTM), a near-field Pyroelectric Scanning Microscope (nPSM), and a Nanoscale Laser-Induced Breakdown Spectrometer (nLIBs, not drawn in the above diagram). Among those modules, the SPM is the key module to perform the fabrication and characterization in nanoscales or even atomic scales. The morphology of materials or substrates is characterized by the SPM, either the

Atomic Force Microscope (AFM) or the STM. The local electronic properties, such as the conductivity and the density of state (DOS), are measured through the Current-Sensing AFM (CSAFM) and the Scanning Tunneling Spectroscopy (STS), respectively. The chemical compositions are characterized by either the μRS or the nRS. Most of nanostructures are fabricated using the LASTM, while the nanostructures containing the polarization information are fabricated using the Laser-Assisted PSM (LAPSM). The fabricated nanostructures are characterized immediately after the fabrication by the SPM, the nRS or the nPSM.

This system allows for the correlated measurement of optical, electronic, chemical, geometric, thermal, and mechanical properties for nanomaterials, nanodevices and nanosystems. Besides, it also allows us to perform nanofabrication, nanomanipulation, and surface nanostructuring on various substrates such as Si substrates. We successfully built the SPM, LASTM, micro-RS (μRS), and n-LIBS. We used the system developed in this project to perform nanopatterning, nanooxidation, and surface nanostructuring; to characterize geometric and electronic properties of the nanostructures; to obtain Raman spectra and images of Si substrates and Single-Walled Carbon nanotubes (SWCNT); and to conduct nano-LIBS experiments on metal and biological samples. In addition, we configured the n-RS apparatus using AFM tips as an optical enhancer. We also developed the n-RS apparatus using STM tips. This apparatus, with unique features and necessary functions, has achieved a spatial resolution of 30 nm.

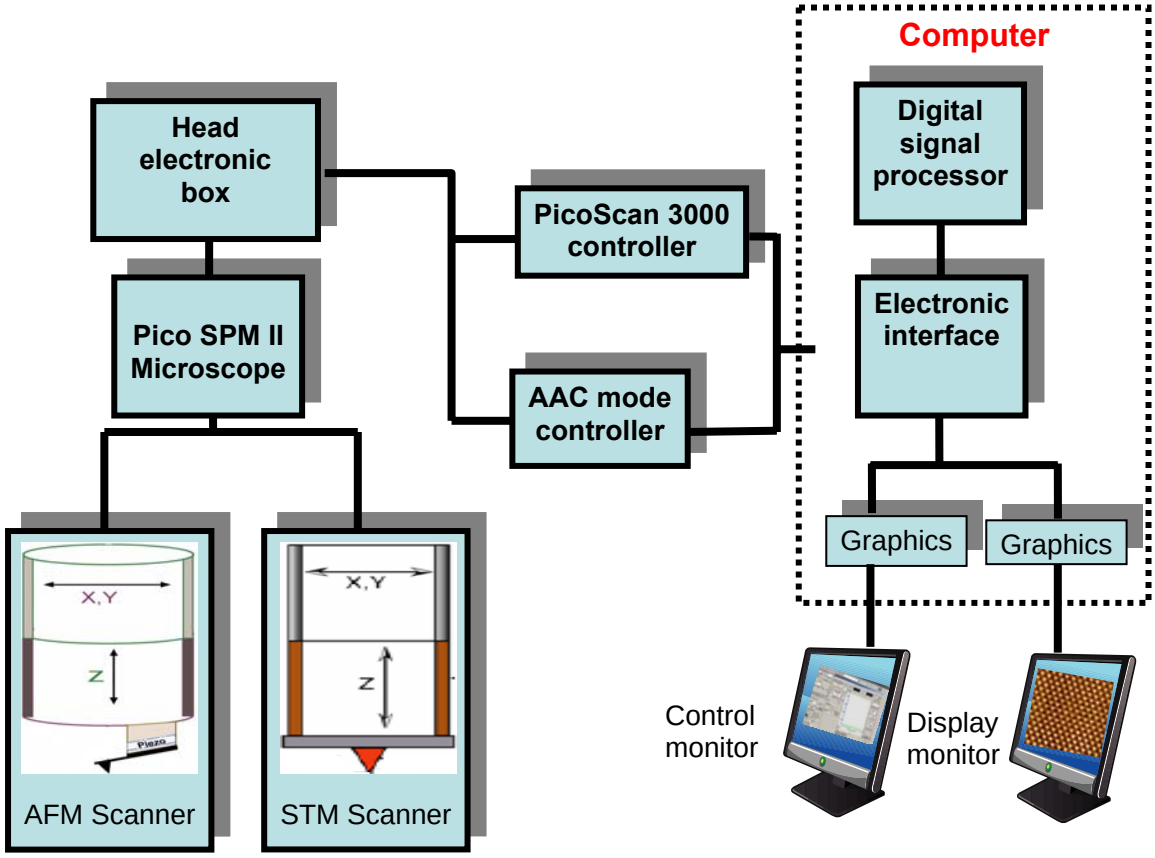

FIGURE A.3 Schematic diagram of the PicoPlus SPM system.

The schematic diagram of the SPM is illustrated in Fig. A.3. The system works in several different modes, such as the contact AFM, the non-contact AFM, the CSAFM, the STM and the STS, depending on which scanner is used. A computer is used for digital signal acquisition, processing and visualization. A controller, i.e., PicoScan 3000, is the main controller used for both the AFM and the STM. In contrast, the AAC controller operates only in the non-contact mode. The head electronic box provides an interface between the scanners and the controllers. The Pico SPM II microscope is composed of an optical microscope for real-time monitoring of the tip-sample surface, three motors for the coarse

approaching, one 4-segement PIN laser diode for the deflection detection, an environment chamber and a main frame. One example of nanolithography on the polycarbonate substrate using the SPM is shown in Fig. A.3.

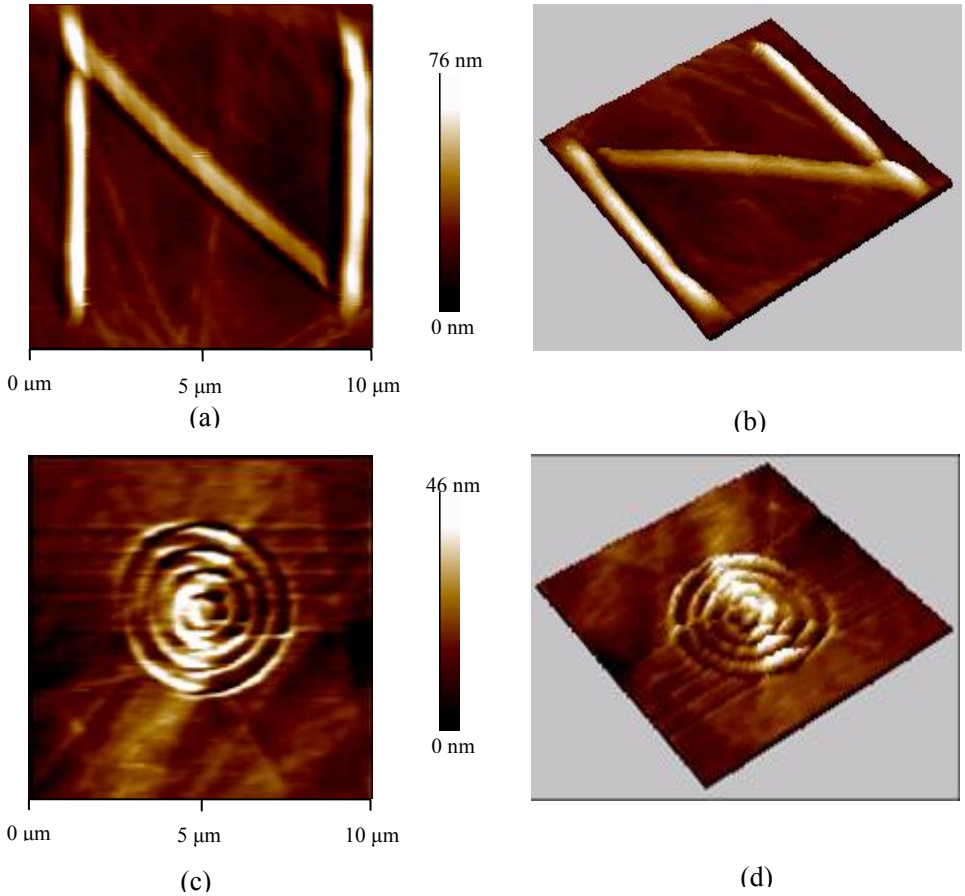

FIGURE A.4 Images of patterns generated by the SPM on the polycarbonate substrate. (a, b):lines; (b, d) circles.

4. DC-etching system

The schematic representation and the experimental setup of the DC electrochemical etching system constructed in our lab are shown in Fig. 11 and Fig. 12 respectively. The etching process involves the anodic dissolution of the W in an aqueous base. The apparatus consists of a beaker containing a given volume of KOH electrolyte. The W wire, which acts as an anode, is dipped into the solution. The anode is surrounded by a stainless steel cathode. The shape of the cathode and the length of the anode in the solution are determined by the nature of the tip required. A DC voltage of predetermined magnitude (also depends on the nature of the tip required) is applied between the two electrodes.

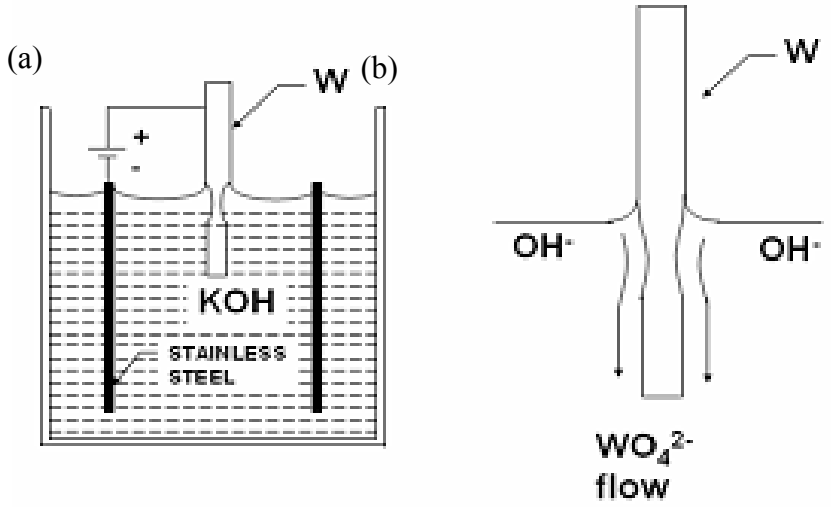

FIGURE A.5 Schematic diagram of the DC EC-etching system (a) and mechanism (b) for W tip fabrication

5. Nanofabrication on Si substrates with self-assembled microparticles

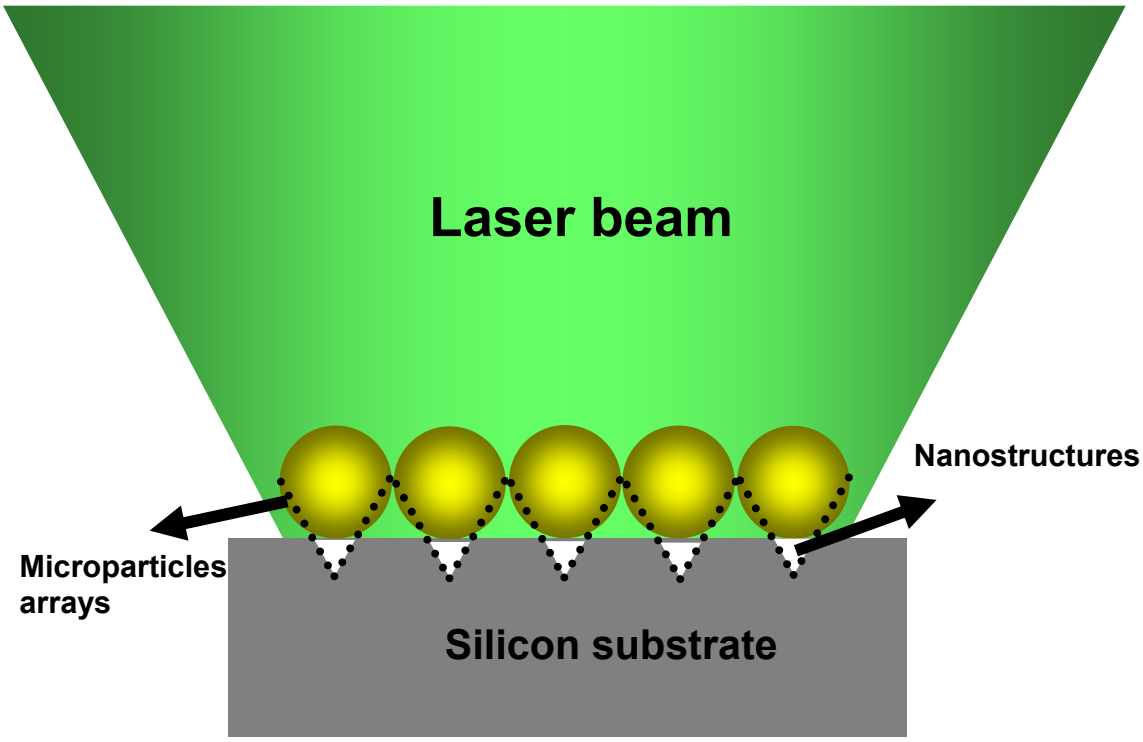

FIGURE A.6 Schematic diagram of surface nanostructuring by irradiating a pulsed laser beam onto microparticles self-assembled on a Si substrate.

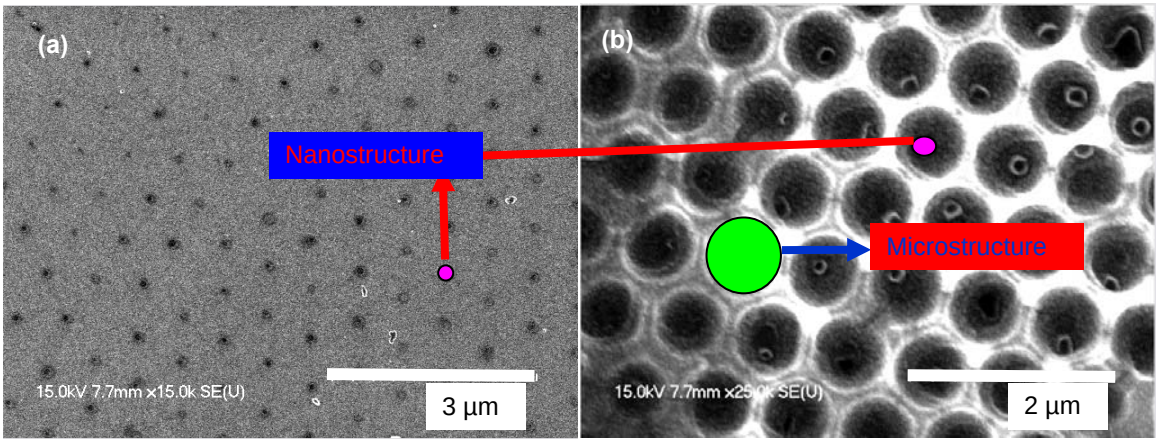

FIGURE A.7 SEM micrographs of nanostructures generated by irradiating a pulsed laser beam onto microparticles self-assembled on the Si substrates using (a) low influence and (b) high influence.

The single-step surface patterning with regular 2D lattices of microparticles has been demonstrated. The 2D lattices of microparticles are formed by the self-assembly processes from the colloidal suspensions. The microparticles which are transparent for the laser radiation focus the incident laser radiation onto the substrate. Figure A.1shows the schematic diagram of surface nanostructuring by irradiating the pulsed laser beam onto the self-assembled microparticles on the Si substrate. The technique allows us to fabricate thousands or millions of single submicron features on a substrate surface with a single or a few laser shots.

LIST OF PUBLICATIONS

Journal papers

[1] **K. J. Yi**, X. N. He, Y. F. Lu *et al.*, "*Increased Raman enhancement in tip-enhanced Raman spectroscopy using optical near fields created by metallic surface nanostructures*", submitted to **Nanotechnology**.

[2] **K. J. Yi**, X. N. He, Y. F. Lu *et al.*, "*Tip-enhanced Near-field Raman Spectroscopy with a Scanning Tunneling Microscope and Side-illumination Optics*", **Rev. Sci. Instrum.**, 79, 051807 (2008).

[3] **K. J. Yi**, Z. Y. Yang, and Y. F. Lu, "*Fabrication of nanostructures with high electrical conductivity on silicon surfaces using a laser-Assisted scanning tunneling microscope*", **J. Appl. Phys.**, 103, 054307 (2008).

[4] **K. J. Yi**, H. Wang, Y. F. Lu and Z. Y. Yang, "*Enhanced Raman scattering by self-assembled silica spherical microparticles*", **J. Appl. Phys.**, 101, 063528 (2007).

[5] W. Xiong, Y. S. Zhou, M. Masoud, W. Q. Yang, **K. J. Yi,** *et al.*, "*Self-aligned growth of single-walled Carbon nanotubes using optical near-field effects*", submitted to Appl. Phys. A.

[6] J. Shi, Y. F. Lu, **K. J. Yi**, *et al.*, "*Direct synthesis of single-walled Carbon nanotubes bridging electrodes by laser-assisted chemical vapor deposition*", **Appl. Phys. Lett.**, 89, 083105 (2006).

[7] J. Shi, Y. F. Lu, H. Wang, **K. J. Yi** *et al.*, "*Synthesis of suspended Carbon nanotubes on silicon inverse-opal structures by laser-assisted chemical vapor deposition*", **Nanotechnology,** 17, 3822 (2006).

Conference papers and presentations

[1] X. N. He, **K. J. Yi**, Y. F. Lu, "*Raman Characterization of Residual Stresses at Nanoscales in Silicon Nanostructures using Tip-enhanced Raman Spectroscopy*", to be presented in **Photonic West 2009** (San Jose, CA, USA).

[2] **K. J. Yi**, X. N. He and Y. F. Lu, *"Surface- and tip-enhanced Raman spectroscopy of silicon*", to be presented in **27th International Congress on Applications of Lasers and Electro-Optics**, 2008, Temecula, CA, USA.

[3] **K. J. Yi,** X.N. He and Y.F. Lu, "*Tip-enhanced near-field Raman spectroscopy using a scanning tunneling microscope with side illumination optics*", **Photonic West 2008** (San Jose, CA, USA) and **Proc. SPIE** Vol. 6880.

[4] **K. J. Yi**, Z. Y. Yang and Y. F. Lu, "*Nanostructure fabrication and characterization on crystal silicon substrates using a laser-assisted scanning tunneling microscope*", **26th International Congress on Applications of Lasers and Electro-Optics**, 2007, Orlando, FL, USA.

[5] **K. J. Yi**, H. Wang, Y. F. Lu and Z. Y. Yang, "*Raman scattering enhancement by silica microparticles*", ***Photonic West 2007*** (San Jose, CA, USA) and **Proc. SPIE** Vol. 6459.

[6] **K. J. Yi**, Y. F. Lu and J. Shi, "*Raman mapping of single-wall Carbon nanotubes in nanoscales with micro-Raman*", **25th International Congress on Applications of Lasers and Electro-Optics**, 2006, Scottsdale, AZ, USA.

[7] **K. J. Yi**, Y. F. Lu and H. Ling, "*Two-dimensional surface characterization of laser-deposited films using Raman scattering*", **Photonic West 2006** (San Jose, CA, USA) and **Proc. SPIE** Vol. 6107.